Numerical studies on the Heisenberg Antiferromagnet on a Square Lattice

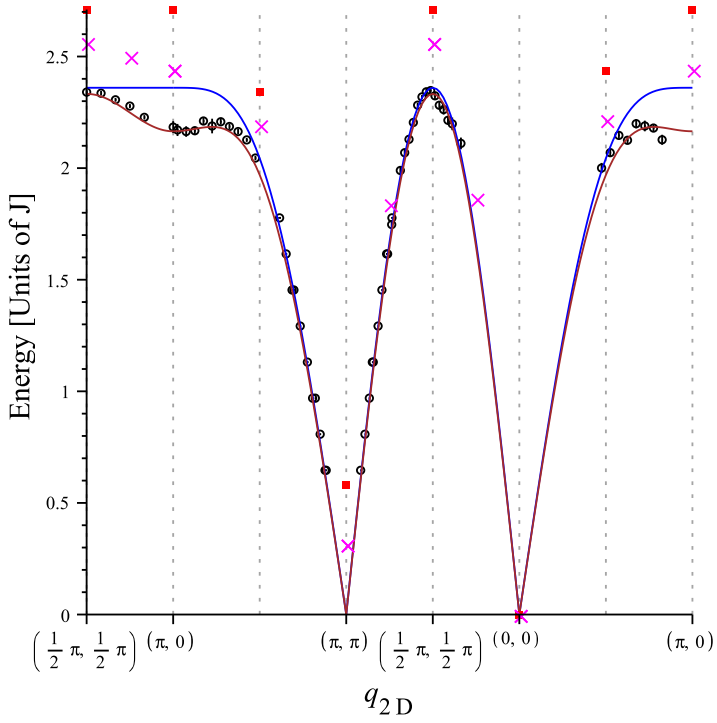

Torsten Tranum Rømer

Master thesis in physics - Speciale i Fysik

Nanoscience Center and E-Science Center

Niels Bohr Institute - Niels Bohr Institutet

University of Copenhagen - Københavns Universitet

July 19, 2010

Front page figure:

Dispersion relation for the Two Dimensional Quantum Heisenberg Antiferromagnetic Square Lattice (2DQHAFSL). The red squares and pink crosses are data from exact diagonalization results for 16 and 32 spin lattices respectively. The solid blue and brown lines are the linear spin wave approximation with nearest and nearest plus next-nearest neighbors respectively. Finally, the black dots with error bars are experimental data from an inelastic neutron scattering experiment on CFTD, by N.B. Christensen *et al.* [23]. The dip in energy at $(\pi, 0)$ is a quantum effect known as the $(\pi, 0)$ anomaly.

Date Torsten Tranum Rømer Cpr.nr.:

Contents

0.1 Foreword and acknowledgments

This thesis work covers 30 ECTS points and has been elaborated in the period from October 2009 to July 2010. The topic is numerical studies by use of the program RLexact, originally made by Kim Lefmann and Christian Rischel from the Niels Bohr Institute, University of Copenhagen. The supervisor on the project is Kim Lefmann, whom I thank for kind guidance in the field of numerical work and extensive directions in writing the thesis.
I also thank N.B. Christensen for extraordinary kind and extensive guidance in the literature of the 2DQHAFSL and careful answers to a wide range of questions and I thank Christian Rischel for discussions on the details of RLexact.
A special 'thank you' goes to Frederik Treue, who has helped me to operate and develop RLexact, including a very profound instruction in the programming languages C and Perl.

Chapter 1

Introduction

1.1 Poor mans physics philosophy

In any type of science a project must start by addressing a very important question: Does the topic of research deserve that effort is being spend on it, and if the answer is affirmative, why? The way to answer this question depends undoubtedly on the field of science, and within physics it boils down to the following: Does the topic from an ethical point of view deserve the interest? Is the topic of relevance for either basic knowledge or technological application? Is it necessary to investigate the topic further or is it already settled?

The overall topic of this thesis is quantum magnetism - a field that is of great interest to basic research, as it is a door to the realm of quantum mechanics. Furthermore quantum magnetism has turned out to be related to superconductivity - a physical state of matter, that if it can be controlled, will revolutionize transport of electrical energy, among other things making it possible to use the huge amount of transport demanding sustainable energy sources such as wind and solar energy. In other words, quantum magnetism is a field that points into the future. The scientific possibilities in quantum magnetism is constantly increasing as new technologies create enhanced possibilities for the experimentalist to explore and for the theorist to model.
Hence, the scientist can with clear conscience and enthusiasm dig into the realm of the quantum magnets.

Modern physics can be divided in two branches - theoretical and experimental physics. In theoretical physics the scientist is working under the constraint, that he or she must construct a systematic theory describing what the human senses register through experiment. This theory must be consistent with mathematical law - which is nothing but systematized human logic.
In order to construct a system of human observation of the physical world, the experiment plays a crucial role, as the link between the observed physics and the theoretical prediction; the results of experiments *are* the physics.
The role of theoretical physics then boils down to the construction of models of the experimentally observed physics - either before or after the experiment has been made. These models must obey two principal rules: They must capture the observed physics and they need to be sufficiently simple, such that the physicist "understands" what is going on. Having constructed a model, the outcome of experiment decides whether the model is legitimate.
This thesis work is no exception: It is investigated to which extent the relatively simple Heisen-

berg Model describes the observations on a physical system.
Well, enough poor mans philosophy, lets get started with the physics.

1.2 The Two Dimensional Quantum Heisenberg Antiferromagnetic Square Lattice (2DQHAFSL)

Quantum magnetism is a huge field of which this thesis work constitutes a tiny part. The physical system that we shall restrict ourselves to investigate, is the two dimensional square lattice governed by the antiferromagnetic (AFM) spin-$\frac{1}{2}$ Heisenberg model[1]. Hence, this system is known as the Two Dimensional Quantum Heisenberg Antiferromagnetic Square Lattice (2DQHAFSL).
The 2DQHAFSL is in its pure version a theoretical model to describe localized electrons interacting antiferromagnetically on the two dimensional square lattice. Crystals which are physical realizations of 2DQHAFSL systems have throughout the last two decades been the topic of intense investigations. The reason that the simplest of all 2D quantum magnetical systems experiences such a huge interest, is that most if not all parents of the High-T_c cuprate superconductors, discovered by Bednorz and Müller in 1986 [2, p.16], contain lattice planes which are described very well by this model.
To mention an example, the most investigated cuprate superconductor Lanthanum Strontium Copper Oxide $La_{2-x}Sr_xCuO_4$ (LSCO) is made by doping Lanthanum Copper Oxide La_2CuO_4 (LCO) with Strontium. LCO is a physical realization of the 2DQHAFSL.
Despite the fact that many parent compounds to High-T_c superconductors contain lattice planes forming 2DQHAFSL systems, it is far from all compounds described by the 2DQHAFSL system, that by doping can be transformed into a High-T_c superconductor. Nevertheless it is from the perspective of High-T_c superconductivity, relevant to explore all corners of the 2DQHAFSL by theoretical, experimental and numerical studies. This thesis work has been done within the field of numerical studies, which will be described in the chapters 4, 5 and 6.

1.2.1 LCO and LSCO

The cuprates superconductors and their parent compounds illustrated by LCO and LSCO order in their solid phase in lattice planes consisting of copper-oxides (CuO_4), separated by physically different inter-planar compounds. From the literature appears, that the interaction between spins within the copper-oxide planes, is about $10^4 - 10^5$ times larger than the interaction between spins localized on neighboring planes [11]. The relative strength of the intra-planar coupling strength as compared to the inter-planar coupling strength, tells us that the valence electrons of the copper oxide essentially move only in the plane and almost don't feel the existence of the outside world. The relevant interaction is therefore an in-plane exchange interaction. The physical realizations of the 2D systems are hence not two dimensional in a mathematical sense.
The classical ground state of an antiferromagnet is the Néel state, in which every spin is aligned anti-parallel to its nearest neighbors, parallel to its next nearest neighbors etc., see left panel of Fig. 2.1.
The most simple quantum mechanical model to describe antiferromagnetically interacting electrons is the Ising model, in which the spins can only order parallel or anti-parallel along the z-axis. The ground state of the Ising model is the Néel state.
The next level of sophistication allows the spins to orient in any spatial direction and contains

[1] The Heisenberg model will be treated in detail in chapter 2.

like the Ising model a coupling strength parameter, that describes whether the spins prefer parallel or anti-parallel alignment. This model is named the Heisenberg model and is the model on which this thesis work is based. The Heisenberg model is treated in detail in Sec. 2.1.
It turns out, that the magnetical properties of the copper-oxide planes in the cuprate compounds in most of the Brillouin zone, are very well described by spin wave calculations based on the 2DQHAFSL. The spin waves we shall return to in Sec. 2.3.
However, at one point in the two dimensional Brillouin zone, the point $(\pi, 0)$, experiments have revealed a pronounced anomaly. An important part of this thesis work is to investigate to which degree this anomaly is generic within the 2DQHAFSL.

1.2.2 CFTD

In this thesis work the results of the numerical studies will primarily be compared with experimental data obtained from CFTD. CFTD is not a cuprate, but is a very well studied quantum magnet, that wrt. magnetic structure resembles the cuprates. It is therefore appropriate to spend a few lines introducing this compound.
CFTD is an abbreviation for Copper Deuteroformate Tetradeuterate and it has the chemical formula $Cu(DCOO)_2 \cdot 4D_2O$. In CFTD as in other physical realizations of the 2DQHAFSL the intra-planar correlation is much greater than the inter-planar correlation. The ratio is about $10^4 - 10^5$[23].
The numerical studies of this thesis work intent among other things to model a series of experiments on CFTD made by N.B. Christensen *et al* [23]. In order to carry out and interpret these simulations properly, it is important to have in mind the physical properties of CFTD.
Below 236 K, which is much above the relevant temperature regime for the experiment carried out, CFTD has the space group $P2_1/n$ with lattice parameters $a = 8.113$ Å, $b = 8.119$ Å and $c = 12.45$ Å. The monoclinic angle, which is the angle between the a- and b-axis, is $100.28°$. The space group-notation should be read such that CFTD has a 2-fold screw-axis with a mirror plane perpendicular to it[2]. The ab-plane contains face-centered spin half Cu^{2+} ions [19], with the rotation axis being parallel to the c-axis and going through these same Copper ions. It is the Copper ions that form an approximate square lattice. In Fig. 1.1 three pictures are displayed. The first is a picture of the 2D unit cell. The dashed red line (solid black line) marks the structural (magnetic) unit cell. It is on the background of this magnetic unit cell, that simulation by RLexact will be carried out and spin wave calculations will be performed. The second picture is a schematic 3D image of the magnetic structure and the last picture displays the entire structure of CFTD at low temperatures, cf. the text above.

The intra-planar coupling constant is 6.19(2) meV [23], determined by fitting experimental data to linear spin wave theory in the $M - \Gamma$ direction. The literature roughly agrees on this value with deviations of about one percent, see f.x. [19] where the value is 6.31(2) meV. We will however in the present work arbitrarily adapt the value of 6.19 meV, when a value is needed. Below $T_N = 16.2(5)$ K the system orders three-dimensionally due to the interlayer coupling[19]. This, however, will not change the fact that the copper-oxide planes effectively are two dimensional. Qualitatively this can be understood from the value of the Boltzmann's constant[3]. If the inter-planar coupling is $10^4 - 10^5$ times smaller than the intra-planar coupling, the magnitude of this coupling must be in the order of 0.01 meV, which corresponds to a temperature of approximately 0.1 K. Hence only if the temperature is in this regime, the interlayer coupling plays a role compared to thermal fluctuations.

[2] The subindex 1 tells that the crystal after rotation of $t \cdot \frac{\pi}{2}$ $(t \in \mathbb{N})$ radians around the 2-fold rotation-axis must be translated by $\frac{1}{2}c$ along the c-axis in order to be brought into coincidence with itself

[3] $K_B \approx 8.6 \cdot 10^{-5}$eV/K, giving the approximate rule of thumb that 0.1 meV corresponds to 1K.

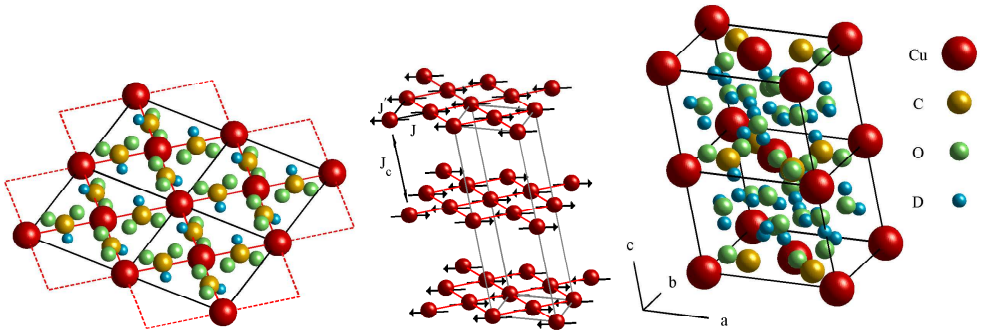

Figure 1.1: The structure of CFTD. Left: The 2D unit cell. The dashed red line (solid black line) marks the structural (magnetic) unit cell. Middle: 3D magnetic structure. Right: The structure at low temperatures, $T < 236$ K. The pictures are kindly supplied by N. B. Christensen.

1.3 The purpose of the project and the structure of the thesis

This thesis work has three main purposes: i) Developing and testing RLexact, ii) running RLexact on various systems in order to compare the results with experimental and numerical data from the literature, and iii) trying to reach exact diagonalization results for a 36 spin square lattice in the $m = 0$ subspace, which is the limit of what has been done in the literature. Further, when defining the project an implementation of RVB[4] calculations into RLexact were discussed. This however, quickly turned out to be impossible due to lack of time in a 30 ECTS project.
In order to set the work into perspective, the reader will find a brief resume of relevant experimental and numerical studies from the literature. This is found in Chapter 3 and 4 respectively. In Chapter 2 which is the theoretical chapter, one finds a resume of relevant theoretical considerations, including the Heisenberg model and the theory of spin waves. After all this the reader should be updated on the scientific status of the 2DQHAFSL, hence being ready to put into perspective the results, discussion and conclusion of this thesis work, which is reported in Chapters 6 and 7. Finally, Chapter 5 concerns selected details of RLexact.

[4]RVB is an abbreviation for Resonating Valence Bond, giving name to the so-called RVB state. This we will return to at various places throughout this thesis.

Chapter 2

Theory

This chapter contains a presentation of the notions used in the thesis work and furthermore outlines relevant calculations in detail.

2.1 The Heisenberg model

We shall start by introducing the Heisenberg model.
In the Heisenberg model for localized electrons each spin only interacts pairwise and it is given by the Hamiltonian

$$\mathcal{H} = -\sum_{\langle ij \rangle} J_{ij} \mathbf{S}_i \cdot \mathbf{S}_j + g\mu_B h \sum_i S_i^z \quad , J_{ij} < 0 \quad , \tag{2.1}$$

where $J_{ij<0}$ implies an antiferromagnet. g is the Landé splitting factor [4, p.139], μ_B is the Bohr magnetic moment and h is a magnetic field applied along an arbitrarily chosen direction, in this case the z axis for simplicity. The symbol $\langle \cdot \rangle$ denotes nearest neighbor summation. Finally the negative sign of J_{ij} favors antiferromagnetism, since opposite neighboring spins will clearly lower the energy.
For the sake of simplicity $J_{ij} = J$ for all i, j, resulting in the form

$$\mathcal{H} = -J \sum_{\langle ij \rangle} \mathbf{S}_i \cdot \mathbf{S}_j + g\mu_b h \sum_i S_i^z \quad , J_{ij} < 0$$

Furthermore expressing the $\mathbf{S}_n^x$ and $\mathbf{S}_n^y$ operators by $\mathbf{S}_n^+ = \mathbf{S}_n^x + i\mathbf{S}_n^y$ and $\mathbf{S}_n^- = \mathbf{S}_n^x - i\mathbf{S}_n^y$ leaves the model as

$$\mathcal{H} = -J \sum_{\langle i,j \rangle} S_i^z S_j^z + \frac{1}{2}\left(S_i^+ S_j^- + S_i^- S_j^+\right) + g\mu_b h \sum_i S_i^z \quad J < 0 \tag{2.2}$$

Within numerical- and theoretical studies it is standard to put $g\mu_b = 1$ and express the energies in units of J. Furthermore all calculations are performed at zero field ($h = 0$) making the last term of Eqn. (2.2) vanish.
Fig. 2.1 shows a classical picture of how the spins (considered as classical vectors) orient themselves with respect to an externally applied h-field. For zero field the classical ground state is the Néel state, in which the system experiences complete long range order, with each spin aligned anti-parallel to its nearest neighbors. For low fields (Fig. 2.1 left) the spins order antiferromagnetically in a plane perpendicular to the applied magnetic field, but with a small uniform out-of-plane component. For strong fields (Fig. 2.1 right) the spins gradually align

parallel to the increasing field, hence creating an uniform out-of-plane component. At the saturation field[1] of $h_s = 8JS = 4J$, see Sec. 2.2.1, for a spin $\frac{1}{2}$ system, all spins are completely aligned along the field. Why this happens at $h = 4J$ can be understood classically by setting $\theta = \frac{\pi}{2}$ in Eqn. (2.6), where θ is the angle defined in Fig. 2.1. In the regime of canted spins where $0 < h < h_s$, it is standard to decompose the spins in a staggered component perpendicular to the field and a uniform component parallel to the field. Quantum mechanically however, the Néel state is not an eigenstate for the Heisenberg Hamiltonian Eqn. (2.1) (or alternatively Eqn. (2.2)) with AFM coupling and therefore the quantum mechanical ground state must be different from the Néel state.

Despite its relative uncomplicated appearance, the Heisenberg model has proved its worth,

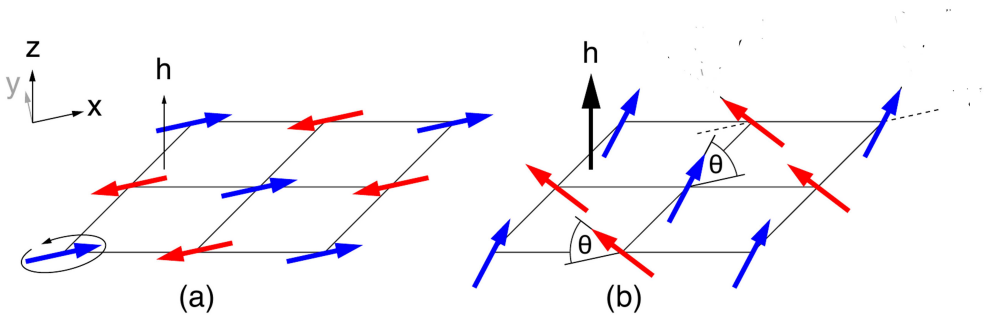

Figure 2.1: Classical picture of the the orientation of electronic spins represented by classical vectors in an externally applied magnetic field h. Left: For low fields the spins order antiferromagnetically in a plane perpendicular to the applied magnetic field, but with a small out-of-plane component. Right: At high fields the spins start to align parallel to the applied field, hence having a component perpendicular and parallel to the field. At the saturation field of $h_s = 8JS$ all spins are completely aligned along the field. The figure is modified from [39].

as an excellent description of two- dimensional quantum magnetical systems, and this thesis work is no exception: The Heisenberg model is the model used to govern the spin dynamics. The Mermin Wagner theorem [3, p. 355] states that at finite temperatures and in two dimensions, long range order is impossible. Experimentally there seems to be consensus though, that the 2DQHAFSL experiences long range AFM order at zero temperature, see f.x. [27] and [19], although zero temperature long range order never has been rigorously proven [37].

The Heisenberg model is now presented, and we will continue with other physical magnitudes relevant to this thesis work.

2.2 Magnetization and magnetic susceptibility

2.2.1 Classical magnetization

This section will be started by deriving the classical expression for the magnetization. We consider the Hamiltonian Eqn. (2.1) but with the the magnetic field in an arbitrary direction

[1] When $g\mu_b = 1$.

such that the last term will be a dot product between $\mathbf{h}$ and $\mathbf{S}_i$. Further we set $J_{ij} = J$ for all i, j. We get

$$\mathcal{H} = -J \sum_{\langle ij \rangle} \mathbf{S}_i \cdot \mathbf{S}_j + g\mu_b \mathbf{h} \cdot \sum_i \mathbf{S}_i \quad J < 0 \tag{2.3}$$

Classically the energy is nothing but the value of the Hamiltonian, yielding

$$E = 2JNS^2 \cos(180 - 2\theta) - g\mu_b NhS \sin(\theta) = -2JNS^2 \cos(2\theta) - g\mu_b NhS \sin(\theta) \quad , \tag{2.4}$$

where the assumption that the spins aligns along the field is made. The magnetization is obtained by differentiating the energy Eqn. (2.4) wrt. the angle θ and setting it equal to zero, hence obtaining the value of θ preferred by the system

$$\begin{aligned} \frac{dE}{d\theta} = 4JNS^2 \sin(2\theta) - g\mu_b NhS \cos(\theta) &= 0 \\ (8JS \sin(\theta) - g\mu_b h) \cos(\theta) &= 0 \end{aligned} \tag{2.5}$$

Giving that either $\cos(\theta) = 0$ or

$$S \sin(\theta) = \frac{g\mu_b h}{8J} \tag{2.6}$$

From Eqn. (2.6) it is seen that the saturation field is $h_s = 8JS$, because the $\sin(\theta) = 1$ giving $\theta = \frac{\pi}{2}$.
We now continue, using that classically the magnetization per spin is $m = g\mu_b S \sin(\theta)$ giving the classical magnetization

$$m(h) = \frac{h}{8J} g^2 \mu_B^2 \tag{2.7}$$

which have the correct unit of μ_B.

2.2.2 Quantum mechanical magnetization

We now turn to the quantum mechanical regime. For a system of N spins the magnetization is given by

$$\mathcal{M} = \frac{1}{N} \sum_i \langle S_i^z \rangle \tag{2.8}$$

which for the fully polarized limit (all spins pointing in the same direction) takes the value $M = S$.
An alternative definition of the magnetization can be obtained, if the energy E of the system is known as a function of an external field h. This relation is

$$m(h) = -\frac{\partial E}{\partial h} \tag{2.9}$$

where the magnetization once again is expressed relative to the number of sites N of the system.

Having obtained a differentiable function for the magnetization $m(h)$, the magnetic susceptibility, can be found from the relation

$$\chi = \frac{\partial m}{\partial h} \tag{2.10}$$

χ is known as the susceptibility (or the transverse susceptibility) and is a measure for how easy a system is magnetized by an applied field. The reason that the susceptibility sometimes is named 'transverse' is due to the classical picture, see Fig. 2.1, in which the spins orient transverse to the applied field. If the system is quantum mechanical and isotropic, this picture

does not make much sense. This is because the response to a field in terms of magnetization, does not have a direction wrt. the field. On the other hand, if the system has an anisotropy along which the spins prefer to align, it makes sense to talk about a susceptibility transverse and longitudinal to this field. Since the systems in this these all are isotropic, we will merely use the name 'the susceptibility'.
Eqns. (2.9) and (2.10) will be used when the data from RLexact is presented.

2.3 Spin waves in the 2DQHAFSL

The starting point when trying to understand the spin dynamics of the 2DQHAFSL, is to use the formalism of spin waves, calculating a spin wave dispersion relation. We shall only treat linear spin wave (LSW) theory (LSWT), which contain the creation- and annihilation of spin waves, but no interaction between the spin waves themselves. The starting point is the classical Néel state. One has to choose in which direction the spins are pointing and the choice can be made arbitrarily as long as one spin direction is chosen. In the present calculation the y-axis is chosen, which explicitly is seen from Eqns. (2.18) and (2.19). Using the Heisenberg Hamiltonian Eqn. (2.1) gives

$$\mathcal{H} = \sum_{nm} J_{nm}\mathbf{S}_n \cdot \mathbf{S}_m = \sum_{n\rho} J_{n,n+\rho}\mathbf{S}_n \cdot \mathbf{S}_{n+\rho} \quad , \tag{2.11}$$

which generalizes to

$$\sum_{n,\rho} J^x_{n,n+\rho}S^x_n S^x_{n+\rho} + J^y_{n,n+\rho}S^y_n S^y_{n+\rho} + J^z_{n,n+\rho}S^z_n S^z_{n+\rho} \quad J_y > J_x, J_z > 0 \quad , \tag{2.12}$$

where the J have been generalized to J^x, J^y and J^z, such that they can vary between the x, y and z directions. Further, the change in summation index from m to ρ comes from changing the summation from being over both sub lattices (m and n) to being over one sub-lattice (n) and nearest neighbor vectors ρ connecting the two sub lattices, see Fig. 2.2. The plan is to

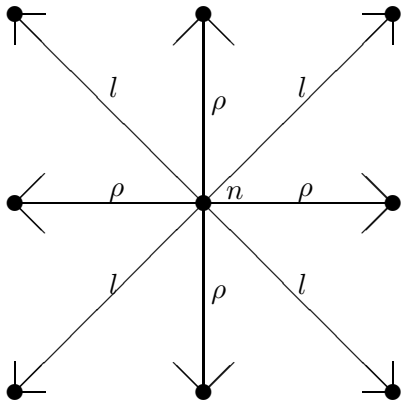

Figure 2.2: Picture illustrating nearest and next-nearest neighbors connected by the vectors ρ and l respectively. ρ takes the values $\hat{x}, -\hat{x}, \hat{y}$ and $-\hat{y}$ and l takes the values $\hat{x}+\hat{y}$, $\hat{x}-\hat{y}$, $-\hat{x}+\hat{y}$ and $-\hat{x}-\hat{y}$

consider the spins as $\mathbf{S} = \langle S \rangle + \delta\mathbf{S}$, i.e. as a number (classical) plus an operator (quantum mechanical). This opens for a semi-classical description of magnetic excitations in the lattice;

the so-called spin waves.
We start by considering the Heisenberg picture in which the time dependence has the form $\frac{d}{dt}\mathbf{S} = \frac{i}{\hbar}[\mathcal{H}, \mathbf{S}]$ and recalling the commutation relations[2] $[\mathbf{S}_\alpha, \mathbf{S}_\beta] = i\varepsilon_{\alpha\beta\gamma}\mathbf{S}_\gamma \quad \alpha, \beta, \gamma = x, y, z$, one gets for a index-$n'$ sub-lattice

$$\begin{aligned}
\hbar\frac{dS^x_{n'}}{dt} = i[\mathcal{H}, S^x_{n'}] &= \\
&= i\sum_{n,\rho}\Big(\big(J_xS^x_nS^x_{n+\rho} + J_yS^y_nS^y_{n+\rho} + J_zS^z_nS^z_{n+\rho}\big)S^x_{n'} \\
&\quad -S^x_{n'}\big(J_xS^x_nS^x_{n+\rho} + J_yS^y_nS^y_{n+\rho} + J_zS^z_nS^z_{n+\rho}\big)\Big) \\
&= i\sum_{\rho,n}\big(J_xS^x_nS^x_{n'}S^x_{n+\rho} + J_yS^y_nS^x_{n'}S^y_{n+\rho} + J_zS^z_nS^x_{n'}S^z_{n+\rho}\big) \\
&\quad -i\sum_{\rho,n}\big(J_xS^x_{n'}S^x_nS^x_{n+\rho} + J_yS^x_{n'}S^y_nS^y_{n+\rho} + J_zS^x_{n'}S^z_nS^z_{n+\rho}\big) \\
&= i\sum_{\rho}\big(-J_y[S^x_{n'}, S^y_{n'}]S^y_{n'+\rho} + J_z[S^z_{n'}, S^x_{n'}]S^z_{n'+\rho}\big) \\
&= i\sum_{\rho}\big(-iJ_yS^z_{n'}S^y_{n'+\rho} + iJ_zS^y_{n'}S^z_{n'+\rho} \\
&= \sum_{\rho}\big(J_yS^z_{n'}S^y_{n'+\rho} - J_zS^y_{n'}S^z_{n'+\rho}\big) \qquad (2.13)
\end{aligned}$$

In the calculations leading to (2.13) it has been used that for $\alpha, \beta, \gamma \in \{x, y, z\}$ then $[S^\alpha_n, S^\alpha_{n+\rho}] = [S^\alpha_{n'}, S^\alpha_n] = [S^\alpha_n, S^\alpha_n] = [S^\alpha_{n'}, S^\beta_n] = 0$ and $[S^\alpha_n, S^\beta_n] = i\varepsilon_{\alpha\beta\gamma}S^\gamma_n$ for $(\alpha, \beta, \gamma) = (x, y, z)$. Alternatively it might be easier in the above calculations to think of these relations as $S^\alpha_nS^\alpha_{n+\rho}S^x_{n'} - S^x_{n'}S^\alpha_nS^\alpha_{n+\rho} = \delta_{nn'}\big[S^\alpha_n, S^x_{n'}\big]S^\alpha_{n+\rho} \quad$ for $\alpha \in \{x, y, z\}$.

From similar calculations one obtains changing n' to n, since it is nothing but an index,

$$\hbar\frac{dS^y_n}{dt} = i[\mathcal{H}, S^y_n] = \sum_{\rho}\big(-J_xS^z_nS^x_{n+\rho} + J_zS^x_nS^z_{n+\rho}\big) \qquad (2.14)$$

$$\hbar\frac{dS^z_n}{dt} = i[\mathcal{H}, S^z_n] = \sum_{\rho}\big(J_xS^y_nS^x_{n+\rho} - J_yS^x_nS^y_{n+\rho}\big) \qquad (2.15)$$

Obtaining altogether

$$\hbar\dot{\mathbf{S}}_n = \sum_{\rho}\begin{pmatrix} J_yS^z_nS^y_{n+\rho} - J_zS^y_nS^z_{n+\rho} \\ -J_xS^z_nS^x_{n+\rho} + J_zS^x_nS^z_{n+\rho} \\ J_xS^y_nS^x_{n+\rho} - J_yS^x_nS^y_{n+\rho} \end{pmatrix} \qquad (2.16)$$

Since also n is nothing but an index, we can now substitute n for m obtaining the equation of motion for the index-m part of the bipartite lattice

$$\hbar\dot{\mathbf{S}}_m = \sum_{\rho}\begin{pmatrix} J_ys^z_mS^y_{m+\rho} - J_zs^y_mS^z_{m+\rho} \\ -J_xs^z_mS^x_{m+\rho} + J_zs^x_mS^z_{n+\rho} \\ J_xs^y_mS^x_{m+\rho} - J_ys^x_mS^y_{m+\rho} \end{pmatrix} \qquad (2.17)$$

We then consider small changes in the spin. Along the spin direction the change is so relatively small, that it can be neglected to first order. This gives for each sub-lattice of the bipartite

[2] These commutation relations must be unit less, i.e. without $\hbar$, since the unit of energy is inside J_i.

lattice

$$\mathbf{S}_n = \mathbf{S} + \delta\mathbf{S}_n = S\hat{\mathbf{y}} + \delta\mathbf{S}_n = \begin{pmatrix} \delta S_n^x \\ S \\ \delta S_n^z \end{pmatrix} \tag{2.18}$$

$$\mathbf{S}_m = \mathbf{S} + \delta\mathbf{S}_m = -S\hat{\mathbf{y}} + \delta\mathbf{S}_m = \begin{pmatrix} \delta S_m^x \\ -S \\ \delta S_m^z \end{pmatrix} \tag{2.19}$$

Here the index $n(m)$ labels the spin up(down) part of the bipartite lattice. Using Eqn. (2.18) and (2.19) in (2.16) and (2.17) one gets

$$\hbar\dot{\mathbf{S}}_n = \hbar\delta\dot{\mathbf{S}}_n = -\sum_\rho \begin{pmatrix} J_y S\delta S_n^z + J_z S\delta S_{n+\rho}^z \\ +J_x\delta S_n^z\delta S_{n+\rho}^x - J_z\delta S_n^x\delta S_{n+\rho}^z \\ -J_x S S_{n+\rho}^x - J_y S\delta S_n^x \end{pmatrix} \approx -\sum_\rho \begin{pmatrix} J_y S\delta S_n^z + J_z S\delta S_{n+\rho}^z \\ 0 \\ -J_x S S_{n+\rho}^x - J_y S\delta S_n^x \end{pmatrix} \tag{2.20}$$

Making the substitutions $S \to -S$, $S_{n+\rho} \to S_{m+\rho}$ and $S_n \to S_m$ one gets for the spin down part

$$\hbar\dot{\mathbf{S}}_m = \hbar\delta\dot{\mathbf{S}}_m = \sum_\rho \begin{pmatrix} J_y S\delta S_m^z + J_z S\delta S_{m+\rho}^z \\ J_x\delta S_m^z\delta S_{m+\rho}^x - J_z\delta S_m^x\delta S_{m+\rho}^z \\ -J_x S S_{m+\rho}^x - J_y S\delta S_m^x \end{pmatrix} \approx \sum_\rho \begin{pmatrix} J_y S\delta S_m^z + J_z S\delta S_{m+\rho}^z \\ 0 \\ -J_x S S_{m+\rho}^x - J_y S\delta S_m^x \end{pmatrix} \tag{2.21}$$

We wish to Fourier transform (2.20) and (2.21) one component at a time, hence introducing for each sub-lattice respectively

$$\mathbf{A_q} = \sqrt{\frac{2}{N}}\sum_n e^{-i\mathbf{q}\cdot\mathbf{R_n}}\delta\mathbf{S_n} \Leftrightarrow \delta\mathbf{S_n} = \sqrt{\frac{2}{N}}\sum_{\mathbf{q}} e^{i\mathbf{q}\cdot\mathbf{R_n}}\mathbf{A_q} \tag{2.22}$$

$$\mathbf{B_q} = \sqrt{\frac{2}{N}}\sum_m e^{-i\mathbf{q}\cdot\mathbf{R_m}}\delta\mathbf{S_m} \Leftrightarrow \delta\mathbf{S_m} = \sqrt{\frac{2}{N}}\sum_{\mathbf{q}} e^{i\mathbf{q}\cdot\mathbf{R_m}}\mathbf{A_q} \tag{2.23}$$

We then transform one component at a time, getting from the x-component of (2.20)

$$\begin{aligned} \hbar\delta\dot{S}_n^x &= -\sum_\rho \left(J_y S\delta S_n^z + J_z S\delta S_{n+\rho}^z\right) \\ &\Updownarrow \\ \hbar\sqrt{\frac{2}{N}}\sum_{\mathbf{q}} e^{i\mathbf{q}\cdot\mathbf{R_n}}\dot{A}_{\mathbf{q}}^x &= -\sqrt{\frac{2}{N}}J_y S\sum_{\mathbf{q},\rho} e^{i\mathbf{q}\cdot\mathbf{R_n}}A_{\mathbf{q}}^z - J_z S\sqrt{\frac{2}{N}}\sum_{\mathbf{q},\rho} e^{i\mathbf{q}\cdot\mathbf{R_{n+\rho}}}B_{\mathbf{q}}^z \end{aligned} \tag{2.24}$$

Demanding that every term on each side of the equality sign must equal for any value of $\mathbf{q}$ we can cancel the summation over $\mathbf{q}$ and multiply by $e^{-i\mathbf{q}\cdot\mathbf{R_n}}$ and divide by $\sqrt{\frac{2}{N}}$. Thereby one obtains

$$\begin{aligned} \hbar\dot{A}_{\mathbf{q}}^x &= -\sum_\rho J_y S A_{\mathbf{q}}^z - \sum_\rho J_z S e^{-i\mathbf{q}\cdot(\mathbf{R_{n+\rho}}-\mathbf{R_n})}B_{\mathbf{q}}^z \\ &= -zJ_y S A_{\mathbf{q}}^z - zJ_z S\gamma_{\mathbf{q}} B_{\mathbf{q}}^z \end{aligned} \tag{2.25}$$

Here the definition $\gamma_{\mathbf{q}} = \frac{1}{z}\sum_\rho e^{-i\mathbf{q}\cdot(\mathbf{R_{n+\rho}}-\mathbf{R_n})}$ has been used along with $\sum_\rho J_y S = zJ_y S$, z denoting the number of nearest neighbors which is 4 for the square lattice.

By similar calculations one obtains the other component of (2.20) and the two components of (2.21)

$$\begin{aligned}
\hbar\dot{A}^z_q &= zJ_ySA^x_{\mathbf{q}} + zJ_xS\gamma_{\mathbf{q}}B^x_{\mathbf{q}} && (2.26)\\
\hbar\dot{B}^x_q &= zJ_ySB^z_{\mathbf{q}} + zJ_zS\gamma_{\mathbf{q}}A^z_{\mathbf{q}} && (2.27)\\
\hbar\dot{B}^z_q &= -zJ_ySB^x_{\mathbf{q}} - zJ_xS\gamma_{\mathbf{q}}A^x_{\mathbf{q}} && (2.28)
\end{aligned}$$

Setting[3] $J_x = J_z = J_{xz}$ a transformation using the ladder operators $A^{\mathbf{q}}_{\pm} = A^x_{\mathbf{q}} \pm iA^z_{\mathbf{q}}$ and $B^{\mathbf{q}}_{\pm} = B^x_{\mathbf{q}} \pm iB^z_{\mathbf{q}}$ one gets by combining Eqns. (2.25) and (2.26) the equations

$$\begin{aligned}
\hbar\dot{A}^+_{\mathbf{q}} = \hbar\big(\dot{A}^x_q + i\dot{A}^z_q\big) &= -zJ_ySA^z_{\mathbf{q}} - zJ_{xz}S\gamma_{\mathbf{q}}B^z_{\mathbf{q}} + i\Big(zJ_ySA^x_{\mathbf{q}} + zJ_{xz}S\gamma_{\mathbf{q}}B^x_{\mathbf{q}}\Big)\\
&= iS\Big(zJ_y\big(A^x_{\mathbf{q}} + iA^z_{\mathbf{q}}\big) + zJ_{xz}\gamma_{\mathbf{q}}\big(B^x_{\mathbf{q}} + iB^z_{\mathbf{q}}\big)\Big)\\
&= iS\Big(zJ_yA^+_{\mathbf{q}} + zJ_{xz}\gamma_{\mathbf{q}}B^+_{\mathbf{q}}\Big) && (2.29)
\end{aligned}$$

Similarly Eqns.(2.25) to (2.28) combine to

$$\begin{aligned}
\hbar\dot{A}^-_{\mathbf{q}} &= -iS\Big(zJ_yA^-_{\mathbf{q}} + zJ_{xz}\gamma_{\mathbf{q}}B^-_{\mathbf{q}}\Big) && (2.30)\\
\hbar\dot{B}^+_{\mathbf{q}} &= -iS\Big(zJ_yB^+_{\mathbf{q}} + zJ_{xz}\gamma_{\mathbf{q}}A^+_{\mathbf{q}}\Big) && (2.31)\\
\hbar\dot{B}^-_{\mathbf{q}} &= iS\Big(zJ_yB^-_{\mathbf{q}} + zJ_{xz}\gamma_{\mathbf{q}}A^-_{\mathbf{q}}\Big) && (2.32)
\end{aligned}$$

Assuming that the $A^{\mathbf{q}}_{\pm}$ and $B^{\mathbf{q}}_{\pm}$ have the harmonic time dependence $e^{i\omega_{\mathbf{q}}t}$ one gets a factor $i\omega_{\mathbf{q}}$ on the left side of Eqns. (2.29) to (2.32) yielding a homogeneous system of equations

$$\begin{aligned}
0 &= \big(zJ_yS - \hbar\omega_{\mathbf{q}}\big)A^+_{\mathbf{q}} + zJ_{xz}S\gamma_{\mathbf{q}}B^+_{\mathbf{q}} && (2.33)\\
0 &= -\big(zJ_yS + \hbar\omega_{\mathbf{q}}\big)A^-_{\mathbf{q}} - zJ_{xz}S\gamma_{\mathbf{q}}B^-_{\mathbf{q}} && (2.34)\\
0 &= -\big(zJ_yS + \hbar\omega_{\mathbf{q}}\big)B^+_{\mathbf{q}} - zJ_{xz}S\gamma_{\mathbf{q}}A^+_{\mathbf{q}} && (2.35)\\
0 &= \big(zJ_yS - \hbar\omega_{\mathbf{q}}\big)B^-_{\mathbf{q}} + zJ_{xz}S\gamma_{\mathbf{q}}A^-_{\mathbf{q}} && (2.36)
\end{aligned}$$

Combining (2.33) with (2.35), or (2.34) with (2.36), in both cases results in the characteristic polynomial

$$det\left(\begin{vmatrix} zJ_yS - \hbar\omega_{\mathbf{q}} & zJ_{xz}S\gamma_{\mathbf{q}} \\ -zJ_{xz}S\gamma_{\mathbf{q}} & -zJ_yS - \hbar\omega_{\mathbf{q}} \end{vmatrix}\right) = 0 \qquad (2.37)$$

Solving this one finally obtains

$$\hbar\omega_{\mathbf{q}} = \pm zS\sqrt{J_y^2 - J_{xz}^2\gamma_{\mathbf{q}}} \qquad (2.38)$$

[3] This assumes the lattice to have the y-direction as the anisotropy direction and hence the x- and z -directions to be completely symmetric.

Eqn. (2.38) is the LSW relation for a 2DQHAFSL with a y-axis spin direction. By setting[4] $J_y = J_{xz} = J$, one obtains the simple dispersion relation

$$\hbar\omega_{\mathbf{q}} = zSJ\sqrt{1-\gamma_{\mathbf{q}}^2} \tag{2.39}$$

For a square lattice the four ($z = 4$) nearest neighbors can be reached from a given site by the vectors[5] $\pm\hat{x}$ and $\pm\hat{y}$. This gives using $|S| = \frac{1}{2}$ that $\gamma_{\mathbf{q}} = \frac{1}{4}\big(2\cos(q_x) + 2\cos(q_y)\big)$ giving a dispersion relation

$$\hbar\omega_{\mathbf{q}} = zSJ\sqrt{1-\Big(\frac{1}{z}\big(2\cos(q_x)+2\cos(q_y)\big)\Big)^2} = 2J\sqrt{1-\big(\frac{1}{2}\cos(q_x)+\frac{1}{2}\cos(q_y)\big)^2} \tag{2.40}$$

Experimental notes

For the purpose of theoretical considerations, the energy is presented in units of J. The magnitude of J depends of course on the compound in question and can be found from neutron scattering experiments. Since we at present only are interested in obtaining the qualitative behavior of the LSW dispersion, we choose to present the energies in units of J. In Fig. 2.3 a plot of the nearest neighbor LSW dispersion relation Eqn. (2.40) is seen.

Constant zone boundary dispersion

From inspection of Fig. 2.3 it is seen that along the magnetic zone boundary (ZB) from $(0,\pi)$ to $(\pi,0)$ the LSW dispersion is constant. This observation can be verified by a simple calculation using that $q_y = \pi - q_x$ along the ZB. This yields that $\frac{1}{2}\cos(q_x) + \frac{1}{2}\cos(q_y) = \frac{1}{2}(\cos(q_x) - \cos(\pi - q_x)) = 0$, since $\cos(\pi - q_x) = -\cos(q_x)$. Hence the dispersion takes the value

$$\hbar\omega_{\mathbf{q}} = 2J \tag{2.41}$$

along the magnetic ZB.

2.3.1 Next-nearest neighbor coupling

In principle every ion (spin) will interact with all other ions (spins) in the system. In many cases though, it turns out that models based on nearest neighbor approximation describes the observed physics quite well. Nonetheless taking into account more ions as interacting bodies for a given ion, could possibly reveal a behavior not captured by the nearest neighbor approximation. It will in the following be investigated what happens to the LSW dispersion relation, if next-nearest neighbors are included in the Hamiltonian (2.1).
The next-nearest neighbors contribution can be expressed as an extra term

$$\sum_{nl} J'_{n,n+l}\mathbf{S}_n\cdot\mathbf{S}_{n+l} = \sum_{nl} J'^{x}_{n,n+l}S^x_nS^x_{n+l} + J'^{y}_{n,n+l}S^y_nS^y_{n+l} + J'^{z}_{n,n+l}S^z_nS^z_{n+l} \quad ,$$

[4]Recall that the J's represents the coupling between spins (in spin space), see Eqn. (2.1). In the above calculation we have chosen the spin direction to be the y direction through the equations (2.18) and (2.19). This means, that a spin wave *consists* of spins precessing around the y direction. When we set $J_x = J_y = J_z = J$, this means that a spin wave can *consist* of precessing spins in all directions. The information about real space enters the above calculation when summing over the nearest neighbor lattice vectors ρ. For the square lattice with nearest neighbor coupling only, this introduces a C_4 symmetry in real space, which through Fourier transformation is carried over to $\mathbf{q}$-space. The C_4 symmetry is clearly visible in Fig. 2.3, which soon will be introduced. The direction in which the spin wave propagates in real space has nothing to do with the coupling constants J of Eqn. (2.1). This direction depends on the lattice in question as given by the vectors ρ.

[5]The lattice constant a is set to 1, such that f.x. $q_x a = q_x$ and $q_y a = q_y$.

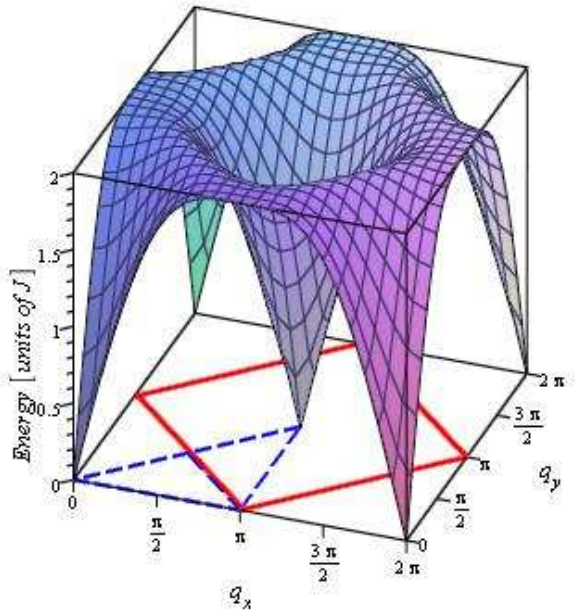

Figure 2.3: Energy dispersion obtained from LSW calculations. Energies are in units of the exchange coupling constant J. The solid red line marks the magnetic zone boundary and the dashed blue line marks the scan in Q_{2D}-space used later on in the thesis, when the energy dispersion is plotted.

where l is a vector summing over next nearest neighbors, see Fig. 2.2, and the coupling constants J' are different from J. This leads to a zero field Hamiltonian of the form

$$\begin{aligned}
\mathcal{H} &= \sum_{nm} J_{nm}\mathbf{S}_n \cdot \mathbf{S}_m \\
&= \sum_{n\rho} J_{n,n+\rho}\mathbf{S}_n \cdot \mathbf{S}_{n+\rho} + \sum_{nl} J'_{n,n+l}\mathbf{S}_n \cdot \mathbf{S}_{n+l} \\
&= \sum_{n,\rho} J^x_{n,n+\rho}S^x_n S^x_{n+\rho} + J^y_{n,n+\rho}S^y_n S^y_{n+\rho} + J^z_{n,n+\rho}S^z_n S^z_{n+\rho} \\
&+ \sum_{n,l} J'^x_{n,n+l}S^x_n S^x_{n+l} + J'^y_{n,n+l}S^y_n S^y_{n+l} + J'^z_{n,n+l}S^z_n S^z_{n+l}
\end{aligned} \tag{2.42}$$

The sign of the constant J' for a AFM lattice is far from self-evident. In LCO which as mentioned is a physical realization of the 2DQHAFS, the next-nearest neighbor coupling is experimentally determined to be ferromagnetic with the value $J' = -11.4 \pm 3$ meV (compare with $J = 111.8 \pm 4$meV) [33]). In CFTD Rønnow *et al.* modeled their experimental data with an additional antiferromagnetic next-nearest neighbor coupling of $J' = 0.067J \pm 0.007J$[19]. It is therefore not clear which sign the next-nearest coupling constant should have in the purely theoretical 2DQHAFSL.

Inspecting (2.42) it is seen that the last term in the calculations of a dispersion relation, can be treated similarly as the first term already handled with, keeping in mind that summing over next-nearest neighbors reaches vectors on the same sub-lattice. Hence, the calculations

for next-nearest neighbors can be performed relatively easy. The starting point is Eqns. (2.20) and (2.21) which generalizes to

$$\begin{aligned}\hbar\dot{\mathbf{S}}_n = \hbar\delta\dot{\mathbf{S}}_n &= -\sum_{\rho,l}\begin{pmatrix} +J_yS\delta S^z_n + J_zS\delta S^z_{n+\rho} - J'_yS\delta S^z_n + J'_zS\delta S^z_{n+l} \\ +J_x\delta S^z_n\delta S^x_{n+\rho} - J_z\delta S^x_n\delta S^z_{n+\rho} + J'_x\delta S^z_n\delta S^x_{n+l} - J'_z\delta S^x_n\delta S^z_{n+l} \\ -J_xSS^x_{n+\rho} - J_yS\delta S^x_n - J'_xSS^x_{n+l} + J'_yS\delta S^x_n\end{pmatrix} \\ &\approx -\sum_{\rho,l}\begin{pmatrix} J_yS\delta S^z_n + J_zS\delta S^z_{n+\rho} - J'_yS\delta S^z_n + J'_zS\delta S^z_{n+l} \\ 0 \\ -J_xSS^x_{n+\rho} - J_yS\delta S^x_n - J'_xSS^x_{n+l} + J'_yS\delta S^x_n\end{pmatrix} \qquad (2.43)\end{aligned}$$

and

$$\begin{aligned}\hbar\dot{\mathbf{S}}_m = \hbar\delta\dot{\mathbf{S}}_m &= \sum_{\rho,l}\begin{pmatrix} J_yS\delta S^z_m + J_zS\delta S^z_{m+\rho} - J'_yS\delta S^z_m + J'_zS\delta S^z_{m+l} \\ -J_x\delta S^z_m\delta S^x_{m+\rho} - J_z\delta S^x_m\delta S^z_{m+\rho} - J'_x\delta S^z_m\delta S^x_{m+l} + J'_z\delta S^x_m\delta S^z_{m+l} \\ -J_xSS^x_{m+\rho} - J_yS\delta S^x_m - J'_xSS^x_{m+l} + J'_yS\delta S^x_m\end{pmatrix} \\ &\approx \sum_{\rho,l}\begin{pmatrix} J_yS\delta S^z_m + J_zS\delta S^z_{m+\rho} - J'_yS\delta S^z_m + J'_zS\delta S^z_{m+l} \\ 0 \\ -J_xSS^x_{m+\rho} - J_yS\delta S^x_m - J'_xSS^x_{m+l} + J'_yS\delta S^x_m\end{pmatrix} \qquad (2.44)\end{aligned}$$

These equations are now Fourier transformed using Eqns. (2.22) and (2.23). Demanding like the considerations leading to Eqn. (2.25), that the terms equal pairwise for each value of $\mathbf{q}$, one arrives at the four coupled differential equations

$$\begin{aligned}\hbar\dot{A}^x_q &= (-zJ_yS + zJ'_yS - zJ'_zS\gamma'_{\mathbf{q}})A^z_{\mathbf{q}} - zJ_zS\gamma_{\mathbf{q}}B^z_{\mathbf{q}} && (2.45)\\ \hbar\dot{A}^z_q &= (zJ_yS - zJ'_yS + zJ'_xS\gamma'_{\mathbf{q}})A^x_{\mathbf{q}} + zJ_xS\gamma_{\mathbf{q}}B^x_{\mathbf{q}} && (2.46)\\ \hbar\dot{B}^x_q &= (zJ_yS - zJ'_yS + zJ'_zS\gamma'_{\mathbf{q}})B^z_{\mathbf{q}} + zJ_zS\gamma_{\mathbf{q}}A^z_{\mathbf{q}} && (2.47)\\ \hbar\dot{B}^z_q &= (-zJ_yS + zJ'_yS - zJ'_xS\gamma'_{\mathbf{q}})B^x_{\mathbf{q}} - zJ_xS\gamma_{\mathbf{q}}A^x_{\mathbf{q}} && (2.48)\end{aligned}$$

where $\gamma'_{\mathbf{q}} = \frac{1}{z'}\sum_l e^{-i\mathbf{q}\cdot(\mathbf{R}_{n+l}-\mathbf{R}_n)}$ and $z' = 4$ is the number of next-nearest neighbors.
Like in the case of nearest neighbors we assume the x and z directions to be symmetric and transforming Eqns. (2.45) to (2.48) by use of the ladder operators $A^{\mathbf{q}}_{\pm} = A^x_{\mathbf{q}} \pm iA^z_{\mathbf{q}}$ and $B^{\mathbf{q}}_{\pm} = B^x_{\mathbf{q}} \pm iB^z_{\mathbf{q}}$ we arrive at four differential equation which are pairwise coupled

$$\begin{aligned}\hbar\dot{A}^+_{\mathbf{q}} &= iS\Big((-zJ_y + zJ'_y - zJ'_z\gamma'_{\mathbf{q}})A^+_{\mathbf{q}} + zJ_{xz}\gamma_{\mathbf{q}}B^+_{\mathbf{q}}\Big) && (2.49)\\ \hbar\dot{A}^-_{\mathbf{q}} &= -iS\Big((zJ_y - zJ'_y + zJ'_x\gamma'_{\mathbf{q}})A^-_{\mathbf{q}} + zJ_{xz}\gamma_{\mathbf{q}}B^-_{\mathbf{q}}\Big) && (2.50)\\ \hbar\dot{B}^+_{\mathbf{q}} &= -iS\Big((zJ_y - zJ'_y + zJ'_z\gamma'_{\mathbf{q}})B^+_{\mathbf{q}} + zJ_{xz}\gamma_{\mathbf{q}}A^+_{\mathbf{q}}\Big) && (2.51)\\ \hbar\dot{B}^-_{\mathbf{q}} &= iS\Big((-zJ_y + zJ'_y - zJ'_x\gamma'_{\mathbf{q}})B^-_{\mathbf{q}} + zJ_{xz}\gamma_{\mathbf{q}}A^-_{\mathbf{q}}\Big) && (2.52)\end{aligned}$$

Using harmonic time dependence $e^{i\omega_{\mathbf{q}}t}$, one gets through differentiation a factor $i\omega_{\mathbf{q}}$ on the left side of the equality sign in Eqns. (2.49) to (2.52). This gives a homogeneous system of differential equations

$$\begin{aligned}0 &= \big((-zJ_y + zJ'_y - zJ'_z\gamma'_{\mathbf{q}}) - \hbar\omega_{\mathbf{q}}\big)A^+_{\mathbf{q}} + zJ_{xz}S\gamma_{\mathbf{q}}B^+_{\mathbf{q}} && (2.53)\\ 0 &= -\big((zJ_y - zJ'_y + zJ'_x\gamma'_{\mathbf{q}}) + \hbar\omega_{\mathbf{q}}\big)A^-_{\mathbf{q}} - zJ_{xz}S\gamma_{\mathbf{q}}B^-_{\mathbf{q}} && (2.54)\\ 0 &= -\big((zJ_y - zJ'_y + zJ'_z\gamma'_{\mathbf{q}}) + \hbar\omega_{\mathbf{q}}\big)B^+_{\mathbf{q}} - zJ_{xz}S\gamma_{\mathbf{q}}A^+_{\mathbf{q}} && (2.55)\\ 0 &= \big((-zJ_y + zJ'_y - zJ'_x\gamma'_{\mathbf{q}}) - \hbar\omega_{\mathbf{q}}\big)B^-_{\mathbf{q}} + zJ_{xz}S\gamma_{\mathbf{q}}A^-_{\mathbf{q}} && (2.56)\end{aligned}$$

of which the first couples with the third and the second couples with the fourth. In both cases the resulting characteristic polynomial is

$$det\left(\left| \begin{array}{cc} zS(-J_y + J'_y - J'_{xz}\gamma'_{\mathbf{q}}) - \hbar\omega_{\mathbf{q}} & zJ_{xz}S\gamma_{\mathbf{q}} \\ -zJ_{xz}S\gamma_{\mathbf{q}} & -zS(-J_y + J'_y - J'_{xz}\gamma'_{\mathbf{q}}) - \hbar\omega_{\mathbf{q}} \end{array} \right| \right) = 0 \tag{2.57}$$

which yields the final LSW result for nearest plus next-nearest neighbor coupling

$$\hbar\omega_{\mathbf{q}} = \pm zS\sqrt{k_1^2 - k_2^2} \tag{2.58}$$

with $k_1 = -J_y + J'_y - J'_{xz}\gamma'_{\mathbf{q}}$ and $k_2 = zJ_{xz}S\gamma_{\mathbf{q}}$. Making the simplification $J_y = J_{xz} = J$ and $J'_y = J'_{xz} = J'$, the dispersion takes the simpler form

$$\hbar\omega_{\mathbf{q}} = \pm zS\sqrt{\Big(-J + J'(1 - \gamma'_{\mathbf{q}})\Big)^2 - J^2\gamma_{\mathbf{q}}^2} \tag{2.59}$$

$\gamma'_{\mathbf{q}}$ is obtained by summing over the vectors $l \in \{\hat{x}+\hat{y}, \hat{x}-\hat{y}, \hat{y}-\hat{x}, -\hat{x}-\hat{y}\}$. This gives

$$\begin{aligned} \gamma'_{\mathbf{q}} &= \frac{1}{z'}\sum_l e^{-i\mathbf{q}\cdot(R_n - R_{n+l})} \\ &= \frac{1}{z'}\big(e^{-i(q_x+q_y)} + e^{-i(q_x-q_y)} + e^{-i(q_y-q_x)} + e^{i(q_x+q_y)}\big) \\ &= \frac{1}{4}\big(2\cos(q_x+q_y) + 2\cos(q_x-q_y)\big) \end{aligned} \tag{2.60}$$

It has been used that the number of next-nearest neighbors $z' = 4$, see Fig. 2.2. Altogether the LSW dispersion relation with next-nearest neighbor coupling takes the form

$$\hbar\omega_{\mathbf{q}} = 2\sqrt{\Big(-J + J'\Big(1 - \big(\frac{1}{2}\cos(q_x+q_y) + \frac{1}{2}\cos(q_x-q_y)\big)\Big)^2 - J^2\Big(\frac{1}{2}\cos(q_x) + \frac{1}{2}\cos(q_y)\Big)^2} \tag{2.61}$$

A plot of the dispersion relation based on nearest plus next-nearest neighbor coupling is seen in Fig. 2.4, where $J' = \pm 0.2J$. The left/right screen shows the dispersion for a negative (antiferromagnetic)/positive (ferromagnetic) J'[6]. This figure will later be interesting in relation with the $(\pi, 0)$ anomaly mentioned in Chapter 1.

2.4 Ferromagnetic spin waves

Since the topic of this work is antiferromagnetic spin waves we will not go into theoretical details about ferromagnetic spin waves, but merely state the result.
For ferromagnetic spin waves in the Heisenberg model with nearest neighbor coupling, Eqn. (2.1) with $J_{ij} = J > 0$ the dispersion relation is given by[7]

$$\hbar\omega = 2S(J(0) - J(\mathbf{q})) + g\mu_b h \tag{2.62}$$

where g and μ_B are defined above and[8] $J(\mathbf{q}) = \sum_n J(\mathbf{R}_n)e^{-i\mathbf{q}\cdot\mathbf{R}_n}$, the summation in n as above being nearest neighbors, next-nearest neighbors etc. $J(0)$ takes the value $4J$.
In Fig. 2.5 a plot of the ferromagnetic dispersion Eqn. (2.62) is seen.

[6] Recall that $J < 0$.
[7] [6, Eqn. (8.11)]
[8] [6, Eqn. (5.14)]

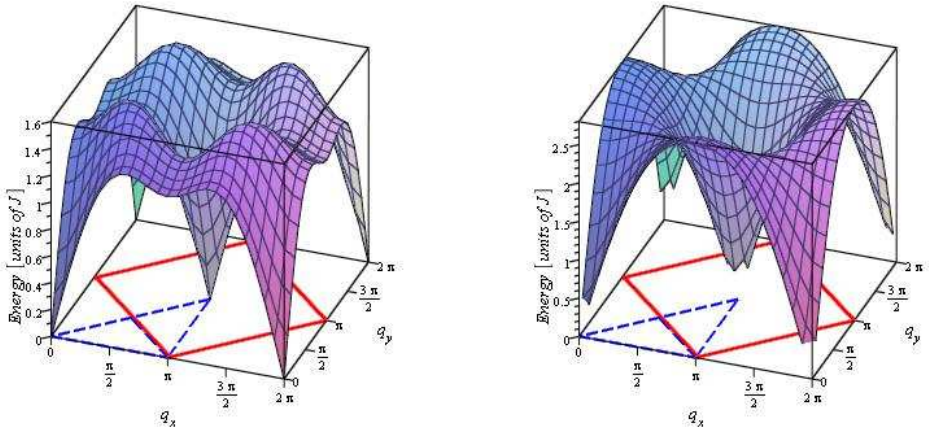

Figure 2.4: Dispersion relation for magnon excitation based on LSW calculation including nearest plus next-nearest neighbors. The left(right) screen displays antiferromagnetic(ferromagnetic) next-nearest neighbor coupling J'. Energies are in units of J. The value of the next-nearest neighbor exchange constant is $J' = +(-)0.2J$ for the left (right) panel. This value is for instructive reasons (to get a visible effect) chosen higher than what can be justified experimentally [19]. The solid red line marks the magnetic zone boundary and the dashed blue line marks the scan in Q_{2D}-space, which shall be used later.

2.5 The dynamical structure factor $S^{\alpha\beta}(\mathbf{q},\omega)$

This section introduces the dynamical structure factor also known as the dynamical correlation function. In order to do this properly it is necessary to introduce a quantity $\frac{d^2\sigma}{d\Omega dE}$ which is measured in neutron scattering experiments and goes under the name 'the differential cross section'. The differential cross section is given by[5, Eqns.(2.65) and (2.66)]

$$\frac{d\sigma^2}{d\Omega dE} = \frac{N}{\hbar}\frac{k_f}{k_i}\Big(\frac{\gamma r_0}{2}\Big)^2 g^2 F(\mathbf{q})^2 e^{-2W} \sum_{\alpha\beta}(\delta_{\alpha\beta} - q_\alpha q_\beta) S^{\alpha\beta}(\mathbf{q},\omega) \tag{2.63}$$

Here

$$S^{\alpha\beta}(\mathbf{q},\omega) = \frac{1}{2\pi}\int_{-\infty}^{\infty} dt e^{-i\omega t} \sum_l e^{i\mathbf{q}\cdot\mathbf{r}_l} \langle S_0^\alpha(0) S_l^\beta(t)\rangle \tag{2.64}$$

where, α and β in general can take the values $\{x, y, z\}$ but in the Heisenberg model Eqn. (2.1) $\alpha = \beta$. Alternatively $\alpha\beta \in \{+-, -+, zz\}$, which is used to obtain the transverse correlation functions

$$S^{xx}(\mathbf{q},\omega) = S^{yy}(\mathbf{q},\omega) = \frac{1}{4}\big[S^{+-}(\mathbf{q},\omega) + S^{-+}(\mathbf{q},\omega)\big]$$

The dynamical structure factor er defined through Eqn. (2.64).
The above formulas are complicated and due will follow an explanation of the various factors involved.
The fraction $\frac{k_f}{k_i}$ is the only factor referring to the experimental setup. The remaining factors are all properties of the sample; N is the number of unit cells, $\gamma = 1.913$ is the gyro magnetic ratio, $r_0 = \frac{e^2}{m_e c^2}$ is the electron radius, $q_\alpha = \mathbf{q}\cdot\mathbf{e}_\alpha$, $q_\beta = \mathbf{q}\cdot\mathbf{e}_\beta$ and g is Landé splitting factor, which is a quantity to be calculated, see f.x. [4, p.139]. Finally we have the Debye-Waller

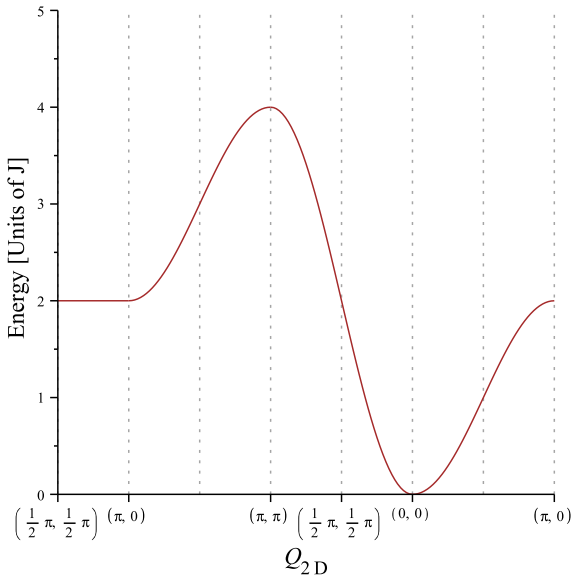

Figure 2.5: The ferromagnetic dispersion relation in zero field displayed as a scan through Q_{2D} space. The scan direction is the same as indicated by the blue dashed line in Fig. 2.4.

factor e^{-2W} which contains information about thermal vibration of the atoms away from their equilibrium positions and the magnetic form factor

$$F(\mathbf{q}) = \int d^3r s(\mathbf{r}) e^{i\mathbf{q}\cdot\mathbf{r}} = \sum_{\mathbf{r}_i} e^{i\mathbf{q}\cdot\mathbf{r}_i} \langle \mathbf{S}_i \rangle \tag{2.65}$$

We shall not pursue the experimental aspects of the differential cross section further. However, it is necessary to spend a little more time on the dynamical structure factor $S^{\alpha\beta}(\mathbf{q},\omega)$ defined in Eqn. (2.64), which is the quantity that RLexact calculates. The expression $\langle S_0^\alpha(0) s_l^\beta(t)\rangle$ in Eqn. (2.64) is a correlation function in space and time, giving the correlation between spins separated by the distance l and the time t. The angular brackets denotes thermal average.
From Eqn. (2.64) it is seen, that the correlation function is Fourier transformed in both space and time with the factor $\sum_{\alpha\beta}(\delta_{\alpha\beta} - q_\alpha q_\beta)$ reflecting that only spin components perpendicular to the scattering vector $\mathbf{q}$ contribute to the scattering signal.
We shall concentrate on $S^{zz}(\mathbf{q},\omega)$, since this is the only component of $S^{\alpha\beta}(\mathbf{q},\omega)$ that RLexact can handle on two dimensional systems. Earlier RLexact was able to perform calculations of the transverse correlation function $S^{xx}(\mathbf{q},\omega)$ for one dimensional systems [34], but this functionality has not yet been carried over to the new parallelized version.

2.5.1 The dynamical structure factor for antiferromagnetic spin waves

In Chapter 6 it will be necessary to compare the dynamical structure factor $S(\mathbf{q},\omega)$ calculated by RLexact with the one predicted by LSWT on antiferromagnets. The present subsection will present the LSWT prediction of $S(\mathbf{q},\omega)$.
According to [22] the differential cross section Eqn. (2.63) reduces for antiferromagnetic spin

waves to

$$\begin{aligned}\left(\frac{d\sigma^2}{d\Omega dE}\right)_{magn.} &= \frac{k_f}{k_i}\Big(\frac{\gamma r_0}{2}\Big)^2 g^2 F(\mathbf{q})^2 e^{-2W}(1+\hat{q}_z^2)\frac{1}{4}\frac{(2\pi)^3}{v_0} \\ &\sum_{\mathbf{q},\tau,a}[(n_{a,\mathbf{q}}+1)\delta(\hbar\omega_{\mathbf{q}}-\hbar\omega)\delta(q-\mathbf{q}-\tau)+n_{a,\mathbf{q}}\delta(\hbar\omega_{\mathbf{q}}-\hbar\omega)\delta(q-\mathbf{q}-\tau)] \\ \times \quad & [u_{\mathbf{q}}^2+v_{\mathbf{q}}+2u_{\mathbf{q}}v_{\mathbf{q}}\cos(\rho\cdot\tau)] \qquad (2.66)\end{aligned}$$

Here τ is a reciprocal lattice vector, ρ is a vector connecting the two sublattices, $\mathbf{q}$ the scattering vector and $n_{a,\mathbf{q}}$ the Bose factor which is zero at 0 K. The last factor is known as the coherence factor and using $n_{a,\mathbf{q}}=0$, this is the only quantity that except for delta-functions depends on $\mathbf{q}$. According to [22] the magnetic coherence factor takes the value

$$u_{\mathbf{q}}^2+v_{\mathbf{q}}+2u_{\mathbf{q}}v_{\mathbf{q}}\cos(\rho\cdot\tau)=2S\sqrt{\frac{J(0)-J(\mathbf{q})}{J(0)+J(\mathbf{q})}} \quad , \qquad (2.67)$$

with $J(\mathbf{q})=\sum_\rho J_\rho e^{i\mathbf{q}\cdot\mathbf{r}_\rho}$.
For later reference the following values are calculated for the square lattice with nearest neighbor coupling only, i.e. $\rho=\{\hat{x},-\hat{x},\hat{y},-\hat{y}\}$. In all calculations $J_\rho=J$

$$\begin{aligned}J(0,0) &= 4J \qquad (2.68)\\ J\big(\frac{\pi}{2},\frac{\pi}{2}\big) &= J(2e^{i\frac{\pi}{2}}+2e^{-i\frac{\pi}{2}})=4J\cos(\frac{\pi}{2})=0 \qquad (2.69)\\ J(\pi,0) &= J(2+e^{i\pi}+e^{-i\pi})=2\big(1+\cos(\pi)\big)=0 \qquad (2.70)\end{aligned}$$

Yielding

$$2S\sqrt{\frac{J(0)-J(\mathbf{q})}{J(0)+J(\mathbf{q})}}=\begin{cases}2S & \text{if } \mathbf{q}=(\frac{\pi}{2},\frac{\pi}{2})\\ 2S & \text{if } \mathbf{q}=(\pi,0)\end{cases}$$

These two values will be used when the results are presented in Chapter 6.

2.6 The staggered magnetization

The staggered magnetization[9] $m^\dagger$ of an antiferromagnet on a square lattice, is defined by

$$m^\dagger = \frac{S_\uparrow - S_\downarrow}{2} \tag{2.71}$$

Hence the classical value of $m^\dagger$ for the Néel state is $m^\dagger_{cl} = S = \frac{1}{2}$. In zero field the staggered moment equals the magnetization of one sub-lattice of a bipartite lattice. The literature present a variety of methods used to determine $m^\dagger$. Among these are a method based on SWT by P. W. Anderson [14], series expansion by D. A. Huse [15] and $1/N$ extrapolations to the thermodynamical limit from numerical results on finite clusters by Oitmaa and Betts [16]. An important remark to the interpolation used by Oitmaa and Betts, is that it is not entirely correct, as is noted by [32] and [15]. The latter explains that the incorrect method is due to the use of a linear interpolation of the mean-square staggered magnetization[10] vs. $1/N$. This procedure assumes the finite size correction to be of order N^{-1}, where it from SWT are found to be $N^{-3/2}$. This results in an overestimation of $m^\dagger$ in the thermodynamical limit [32].
[15] explains that for finite systems, the mean-square staggered magnetization per spin should converge as $(m^\dagger_N)^2 - (m^\dagger)^2 \sim N^{-1/2}$ resulting in the expectation $(m^\dagger_N)^2 = (m^\dagger)^2 + \alpha N^{-1/2} + \beta N^{-1} + \ldots$. This tells, that a reliable $N \to \infty$ interpolation can only be made if there is reason to believe that $\beta N^{-1} \ll \alpha N^{-1/2}$. In the absence of knowing α and β this can be expressed as $(m^\dagger_N)^2 - (m^\dagger)^2 \ll (m^\dagger)^2$. This we will return to in the discussion of the results in chapter 6.

In the following the basic theory for the staggered moment will be presented.
The static *structure factor* is given by

$$S^{zz}(\mathbf{q}) = \int \partial\omega S^{zz}(\mathbf{q},\omega) \tag{2.72}$$

Performing the integral one gets

$$\int \partial\omega S^{zz}(\mathbf{q},\omega) = \int \partial\omega \sum_e M^{zz}_e(\mathbf{q},\omega)\delta(\omega+E_0-E_e) = \int \partial\omega \sum_e 2\pi|\langle e|S^z_{\mathbf{q}}|gs\rangle|^2\delta(\omega+E_0-E_e) \quad , \tag{2.73}$$

where E_0 is the ground state energy, E_e is the energy of the exited states and the definition of the matrix elements are $M^{zz}_e(\mathbf{q},\omega) = 2\pi|\langle e|S_{\mathbf{q}^z}|gs\rangle|^2$. Performing the summation and integration in Eqn. (2.73) yields

$$\begin{aligned}
\int \partial\omega \sum_e 2\pi|\langle e|S^z_{\mathbf{q}}|gs\rangle|^2\delta(\omega + E_0 - E_e) &= \sum_e \int \partial\omega 2\pi|\langle e|S^z_{\mathbf{q}}|gs\rangle|^2\delta(\omega,\omega_{\mathbf{q}}) \\
&= \sum_e 2\pi|\langle e|S^z_{\mathbf{q}}|gs\rangle|^2 \\
&= 2\pi \sum_e \langle gs|S^z_{\mathbf{q}}|e\rangle\langle e|S^z_{\mathbf{q}}|gs\rangle \\
&= 2\pi\langle gs|\left(S^z_{\mathbf{q}}\right)^2|gs\rangle \\
&= 2\pi F(\mathbf{q})
\end{aligned} \tag{2.74}$$

Here

$$F(\mathbf{q}) = \left|\frac{1}{\sqrt{N}} \sum_{\mathbf{r}_j} e^{i\mathbf{q}\cdot\mathbf{r}_j}\langle \mathbf{S}^z_j\rangle\right|^2$$

[9] Also known as the Static Moment.
[10] Except for a $1/N^2$ normalization defined as Eqn. (2.75).

is nothing but the magnetic structure factor of the ground state. Evaluating this in (π, π) gives

$$F(\pi,\pi) = \Big|\frac{1}{\sqrt{N}}\sum_{jj'} e^{i\pi(j+j')}\langle \mathbf{S}^z_{jj'}\rangle\Big|^2 \tag{2.75}$$

The factor $e^{i\pi(j+j')}$ takes the values -1 for $j+j' = (2n+1)$ and the value 1 for $j+j' = 2n$, where n is an integer. Hence the summation in j and j' equals $N\delta_{jj'}$, yielding that that Eqn. (2.75) takes the value $N\langle S\rangle^2$. Since $S(\pi,\pi) \equiv 2\pi N\big(m^\dagger\big)^2$ this gives the final relation between the static structure factor in (π,π) and the staggered moment

$$m^\dagger = \langle S\rangle = \sqrt{\frac{S((\pi,\pi))}{2\pi N}} \tag{2.76}$$

Using the simple method of Oitmaa and Bets discussed above, it is now possible to make a plot of $m^\dagger$ vs. $1/N$ reading of the value of the staggered moment in the thermodynamical limit, as the abscissa intercept. Despite the overestimation of $m^\dagger$, this method will be used in this thesis work.

2.7 Quantum theory for the spin-$\frac{1}{2}$ quantum magnet on a square lattice.

This section will offer an overview of some of the relatively new ideas for quantum theory on the spin-$\frac{1}{2}$ quantum magnet on a square lattice.

2.7.1 Resonating Valence Bonds

The lack of rigorous proof and clear experimental results for the ground state of the spin-$\frac{1}{2}$ quantum magnet on the square lattice, has facilitated speculations about the nature of this ground state. A few of these ideas will now be presented briefly.
We shall start our review about eighty years ago. The story can be started in many ways, but we will start in 1931 where a paper published by Bethe [17] established that general antiferromagnetic chains do not experience classical ground state order. In 1938 it was realized by Hultén, that the exited states of these chains also could not be described by classical theory. At this point in our review it suffices to use a few lines briefly illustrating the physics of quantum antiferromagnets as opposed to ferromagnets, and it is instructive to look at a two-electron system. The ground state of this system is the well known singlet $|\Psi\rangle = \frac{1}{\sqrt{2}}\big(|\uparrow\downarrow\rangle - |\downarrow\uparrow\rangle\big)$. The Heisenberg Hamiltonian Eqn. (2.1) introduces a coupling constant J between the two ions (spins) that through its sign favors either parallel (FM) or anti-parallel (AFM) alignment of nearest neighbors. If we stick to the simple case of two spins, it is readily found that in the case of parallel alignment the ground state is a triplet consisting of $|\uparrow\uparrow\rangle$, $|\downarrow\downarrow\rangle$ and $\frac{1}{\sqrt{2}}\big(|\uparrow\downarrow\rangle + |\downarrow\uparrow\rangle\big)$ whilst in the case of anti-parallel alignment the ground state is the anti-symmetric singlet, as stated above. What should be noted here, is that in the case of ferromagnetism, the classical ground states $|\uparrow\uparrow\rangle$ and $|\downarrow\downarrow\rangle$ still co-exists with the purely quantum mechanical member of the triplet, whilst in the antiferromagnetic case the unique solution to the ground state is of pure quantum mechanical nature. This simple example tells the troubles we are facing, when trying to understand more complex antiferromagnets.
The next occurrence that has found its way to this brief history of quantum magnetism, takes place in 1973. In this year Anderson published a paper [12] about the ground state of the triangular lattice. He proposed that the ground state was described by what he called

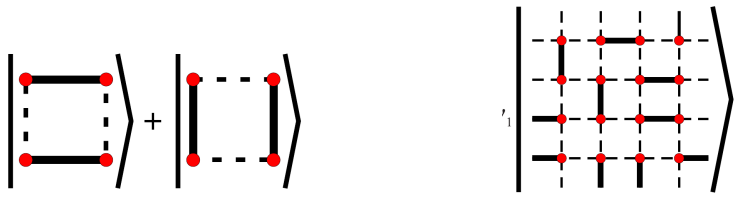

Figure 2.6: Illustration of the RVB idea. Left: The quantum mechanical ground state of the square plaquette is the sum of two terms, each consisting of two dimer singlet pairs along the edges of the plaquette. This is the RVB state. Right: For a bigger lattice the RVB state is the superposition of all possible dimer singlet coverings. Here one of the possible configuration are illustrated. The picture is taken directly from [23].

Resonating Valence Bonds (RVB). In this picture the electrons in the ground state are entangled in a way similar to the Cooper pairs in BCS theory from 1957[11]. BCS theory is used to describe low-T_c superconductivity, a phenomenon that was discovered as long ago as in 1911 by H. Kammerlingh Onnes.
In 1986 Bednorz and Müller discovered a new type of cuprate material surprisingly displaying infinite conductivity above 30 K, which was the limit set by BCS theory. This founded the field of High Temperature Superconductivity (HTSC). These cuprates are closely related to the spin-$\frac{1}{2}$ quantum magnet on a square lattice, since they are made from parent compounds described well by this structure. Inspired by his idea from 1973, Anderson suggested [13], that the RVB state could be the true ground state for the spin-$\frac{1}{2}$ quantum magnet on a square lattice. In Fig. 2.6 the RVB idea is illustrated for a square plaquette and a general square lattice. The RVB state of a square lattice is the sum of all possible dimer coverings, a dimer being the ground state singlet of a spin-pair discussed above. The notion of RVB are in the literature sometimes used somewhat hand waving. For an exact definition, see [30].
The RVB idea is in relation with the ground state of the spin-$\frac{1}{2}$ quantum antiferromagnet on the square lattice still under discussion, and it has until today not been possible to obtain strong experimental evidence nor rigorous proof, indicating its existence. Actually some results indicate a high degree of classical ground state order [31]. Still, the idea is at play as a possible admixture of the true ground state, see e.g. [23].

2.7.2 Ring exchange

The Heisenberg model, Eqn. (2.1) have despite its simplicity, been relatively successful in describing many aspects of the spin-$\frac{1}{2}$ quantum antiferromagnet on a square lattice. However, other models have turned out to be relevant as the governing Hamiltonian and we shall now briefly comment on one of those.
This model originates from HTSC, where the 2DQHAFSL is too simple to describe the copper planes of the cuprate, and goes under the name *ring exchange*. It stems from considerations whether nearest neighbor coupling is too simplified to catch small details, a notion that is supported by experimental results [21, 33]. The considerations are based on the Hubbard model, which is given by the Hamiltonian

$$\mathcal{H} = \sum_{\sigma} \sum_{\langle xy \rangle} -\mathfrak{t} \left[c^{\dagger}_{x\sigma} c_{y\sigma} + c^{\dagger}_{y\sigma} c_{x\sigma} \right] + U \sum_{x} n_{x\uparrow} n_{x\downarrow} \tag{2.77}$$

[11] By Bardeen, Schrieffer and Cooper

Here σ is the summation index for spin, which can take two values; up and down. The indices x and y sums over lattice sites and $\langle\rangle$ means sum over nearest neighbors. c and $c^\dagger$ are the usual fermionic number operators and $n = c^\dagger c$.
Transforming Eqn. (2.77) from the Hubbard space (expressed by the many-body formalism) to the spin-space and going to third order in t/U yields [21]

$$\begin{aligned}\mathcal{H}^{\text{extended}} &= \left(\frac{4t^2}{U} - \frac{24t^4}{U^3}\right)\sum_{\langle ij\rangle}(\mathbf{S}_i\cdot\mathbf{S}_j) + \left(\frac{4t^4}{U^3}\right)\sum_{\langle\langle ij\rangle\rangle}(\mathbf{S}_i\cdot\mathbf{S}_j) + \left(\frac{4t^4}{U^3}\right)\sum_{\langle\langle\langle ij\rangle\rangle\rangle}(\mathbf{S}_i\cdot\mathbf{S}_j) \\ &+ \frac{80t^4}{U^3}\sum_{\langle ijkl\rangle}(\mathbf{S}_i\cdot\mathbf{S}_j)(\mathbf{S}_k\cdot\mathbf{S}_l) + (\mathbf{S}_i\cdot\mathbf{S}_l)(\mathbf{S}_k\cdot\mathbf{S}_j) - (\mathbf{S}_i\cdot\mathbf{S}_k)(\mathbf{S}_j\cdot\mathbf{S}_l) \qquad (2.78)\end{aligned}$$

The indices i, j, k, l run over the four corners of a square plaquette and it is due to the negative sign in the last term, important that i and k are in each end of the same diagonal. The first three terms are nearest-, next-nearest and next-next-nearest neighbors respectively, therefore essentially containing the same physics as Eqn. (2.1), just longer range. The fourth term that goes under the name *ring exchange* is morphologically different, as it includes multi spin interactions. In order to illustrate the physics of this extended model, we ignore all two spin interactions except nearest neighbors, but keep the four spin ring exchange term. Naming the constant belonging to the ring exchange term J_R we get

$$\mathcal{H} = -\sum_{\langle ij\rangle} J_{ij}\mathbf{S}_i\cdot\mathbf{S}_j + J_R\sum_{\langle ijkl\rangle}\{(\mathbf{S}_i\cdot\mathbf{S}_j)(\mathbf{S}_k\cdot\mathbf{S}_l) + (\mathbf{S}_i\cdot\mathbf{S}_l)(\mathbf{S}_k\cdot\mathbf{S}_j) - (\mathbf{S}_i\cdot\mathbf{S}_k)(\mathbf{S}_j\cdot\mathbf{S}_l) \quad (2.79)$$

The first term in Eqn. (2.79) can be recognized as the Heisenberg Hamiltonian Eqn. (2.1), where $J = 4\frac{t^2}{U} - 24\frac{t^4}{U^3}$. We will in the outlook return to the idea of ring exchange.

Chapter 3

Experimental work

As mentioned in the introduction it is important to realize, what it exactly is, that one wants to investigate and why it is interesting. Here the result of experiment plays a crucial role, as the documentation of the physical reality, that must be explained by the theoretical models. If the result of experiment is explainable to a satisfactory degree by the already existing theory, the topic should be considered as settled. On the other hand, if experiment reveals phenomenons not fully understood within the existing theory, the race has begun. The situation is often, that experiment supplies the scientist with clues about what is going on, hence pointing to an appropriate starting point. In this chapter the reader will be familiar with experimental results on the 2DQHAFSL - or rather physical realizations of this system, that should convince the reader of the relevance of the proceeding thesis. During the process of connecting experiment to theory, a tool turns out to be of great use: Numerical simulations - the subject of this thesis. The next chapter will present an outline of the numerical work on the 2DQHAFSL, putting into perspective the efforts of this thesis work. Now, back to the experiments.

The 2DQHAFSL has many physical realizations on which neutron scattering experiments has been carried out. On top of the before mentioned cuprates we find $K_2V_3O_8$ [27], Rb_2MnF_4 [28], $Cu(pz)_2(ClO_4)_2$ [29] and CFTD [19, 23]. It is as stated earlier the latter compound CFTD, that in this work will be the primary target of comparison with the numerical studies of RLexact.

3.1 Focus on the $(\pi, 0)$ anomaly

In this section the reader will be presented the experimental result on what is known as the $(\pi, 0)$ anomaly.

3.1.1 CFTD

In 2001 Rønnow *et al.* [19] performed an investigation by neutron scattering of the spin dynamics of CFTD. One conclusion of their work is the existence of a quantum induced ZB dispersion relation, seen as a dip in the energy branch around $(\pi, 0)$ wrt. what is expected from LSWT, see left panel of Fig. 3.1. The result have been confirmed by N.B. Christensen *et al.* [23], whose results for reference are presented in the right panel of Fig. 3.1. Along the direction from $(\frac{\pi}{2}, \frac{\pi}{2})$ towards $(\pi, 0)$ both groups[1] find a substantial dip in energy at $(\pi, 0)$ which was

[1] Note that N.B. Christensen *et al.* scans from $(\frac{3\pi}{2}, \frac{\pi}{2})$ to $(\pi, 0)$ which due to symmetry is a physically similar path in the Brillouin zone.

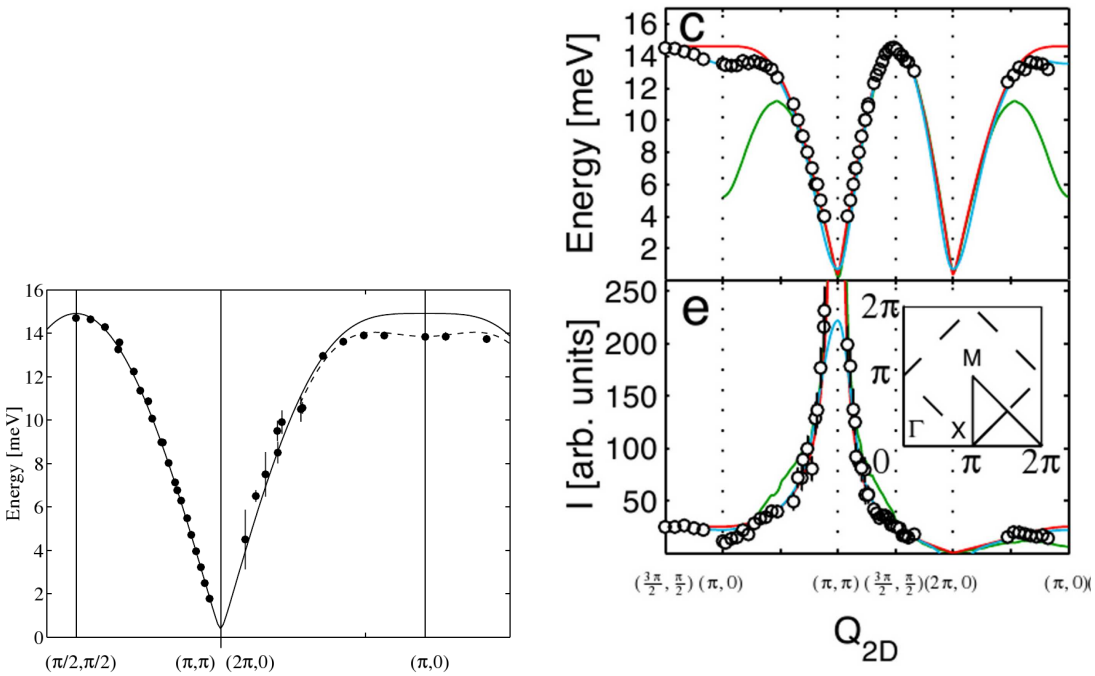

Figure 3.1: Left: The SW dispersion in CFTD at 8 K. The solid line is a fit by nearest neighbor LSWT, giving $J = 6.31 \pm 0.02$ meV. The dashed line is a result of an expansion from the Ising limit using $J = 6.31$ meV. The dots are the neutron scattering data. The picture is taken directly from Rønnow *et al.* [19]. Right (top): The dip in energy at $(\pi, 0)$. The open symbols are experimental data, the red line is the nearest neighbor LSW prediction, Eqn (2.40) and the green (blue) lines are due to series expansion (flux-phase RVB). Right (bottom): The intensity of spin excitations. Symbol- and color coding is as above. The inset shows the scan direction in Q_{2D}-space. Both panels are taken directly from N.B. Christensen *et al.* [23].

determined to 6(1)% and 7(1)% by Rønnow *et al.* and Christensen *et al.* respectively. The dip is expressed relative to the value at $(\frac{\pi}{2}, \frac{\pi}{2})$, since LSWT predicts constant energy along the magnetic ZB and therefore gives the same value at $(\frac{\pi}{2}, \frac{\pi}{2})$ and $(\pi, 0)$, see Eqn. (2.41).
Christensen *et al.* also measured the intensity of the scattered neutrons, and their results are displayed in Fig. 3.2. As is clearly visible from the two uppermost pictures, the intensity at $(\pi, 0)$ indeed experiences a substantial reduction in intensity wrt. $(\frac{\pi}{2}, \frac{\pi}{2})$. This feature is displayed in the lower panel of this figure, where it is seen that exactly at $(\pi, 0)$ the intensity drops markedly seen relative to the LSW predicted value. This feature is not present at other points in the 2D Brillouin zone. Christensen *et al.* report that 54(15)% of the LSW predicted intensity[2] at $(\pi, 0)$ is removed [23]. It turns out, that even though the dip in energy at $(\pi, 0)$ can be explained by LSWT with next-nearest neighbor interactions[3], the reduction in intensity can not [23]. This tells us that sizable quantum effects are present and according to Christensen *et al.* the length scale of this effect [23] is about[4] 10 Å, which is about two times the nearest neighbor distance in the Copper planes. Hence, it seems as if the interaction governing the $(\pi, 0)$ anomaly must include more spins than just nearest neighbors.

[2] See Sec. 2.5.1

[3] See Sec.2.3.1 Fig. 2.4 and Rønnow *et al.* [19]

[4] This result is obtained by measuring the half-width in momentum space at the $(\pi, 0)$ intensity anomaly to be 0.1 $Å^{-1}$.

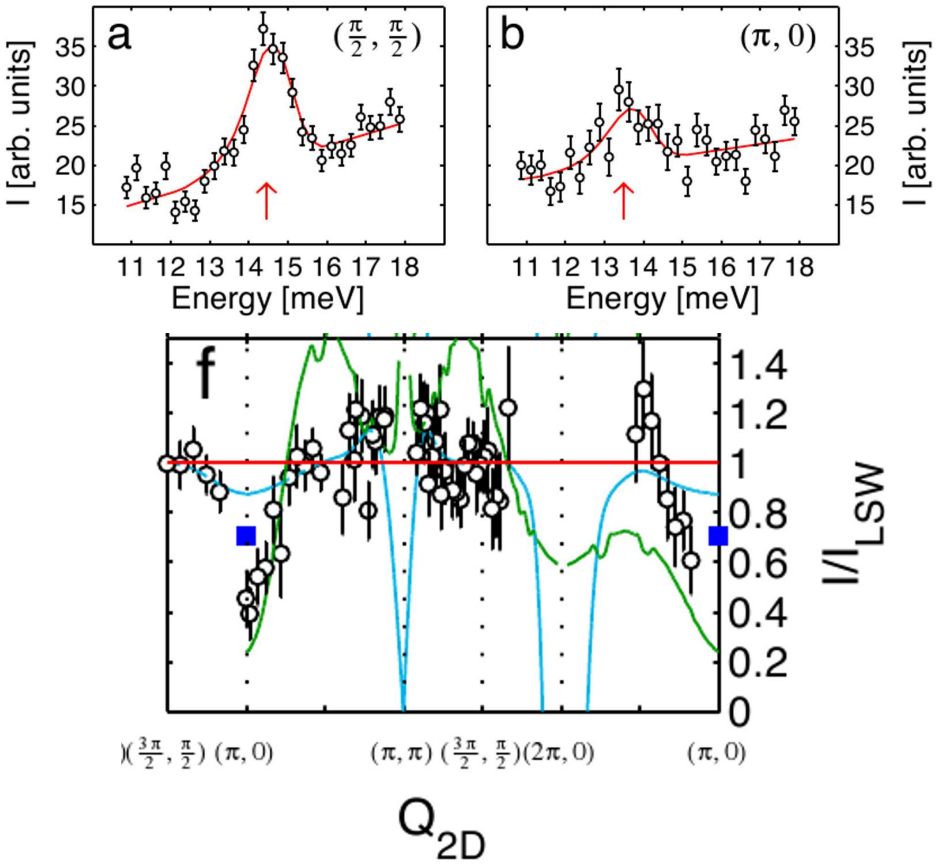

Figure 3.2: Top: Constant wave vector cuts at the high symmetry points $(\frac{\pi}{2}, \frac{\pi}{2})$ and $(\pi, 0)$ of the magnetic Brillouin ZB. The red arrow indicates the center of the peak. The red line is a fit through the data points, used to derive the dispersion and intensity at the points in the two dimensional Brillouin zone. Bottom: Intensity divided by the LSW intensity prediction that best describes data between (π, π) and $(2\pi, 0)$. The red line represents the LSW predicted intensities. The blue and green lines are fits by other methods. The figure is taken directly from Christensen *et al.* [23].

3.1.2 LCO

Another physical realization of the 2DQHAFSL is LCO. This layered cuprate is from the point of view of superconductivity very interesting, since it is the parent compound of the high temperature superconductor LSCO.

In neutron scattering experiments, LCO has revealed [33] a ZB quantum effect similar to that of CFTD. This result is shown in Fig. 3.3. In picture A an important feature is revealed: The dip in energy dispersion between $(\frac{1}{2}, 0) \sim (\pi, 0)$ and $(\frac{3}{4}, \frac{1}{4}) \sim (\frac{\pi}{2}, \frac{\pi}{2})$ is more pronounced at $T = 10$ K than at $T = 295$ K. The authors explain this by a Heisenberg model, with nearest plus next-nearest neighbor interaction with coupling strengths J and J', see Sec. 2.3.1. The solid lines in picture (A) and (B) are nearest plus next-nearest LSW fits, resulting in an antiferromagnetic $J = 111.8 \pm 4$ meV and an ferromagnetic $J' = -11.4 \pm 3$ meV. The ferromagnetic J' is problematic, since it directly contradicts theoretical predictions [24] and further is not compatible with experimental results for $Sr_2Cu_3O_4Cl_2$, which contains an exchange path be-

tween the Cu atoms, similar to that in LCO [33].
According to Coldea *et al.* the data of Fig. 3.3 (A) can also be fitted by a Hubbard model[5], that if expanded to fourth order in the hopping constant t, regains the form given by Eqn. (2.78). The fit from this model is indistinguishable [33] to that from the Heisenberg model with J and J' being the only nonzero coupling strengths. Hence, we cannot from experiment judge which model is correct. As is obvious from the above outline, LSW theory based on the Heisen-

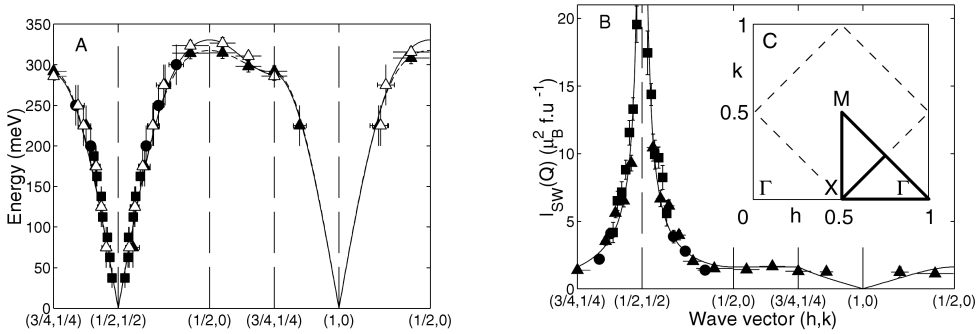

Figure 3.3: (A) Dispersion relation along high symmetry directions in the 2D Brillouin zone (See inset C) of LCO obtained at $T = 10$ K (open symbols) and $T = 295$ K (solid symbols). The shape of the symbol tells the energy of the incoming neutrons, which for the purpose of displaying the quantum effect is not important. The solid and dashed lines are fits to LSW dispersion (see text).(B) Wave vector dependence of the spin wave intensity at $T = 295$ K (all points) compared with predictions of LSW theory (solid line).(C) The Brillouin zone in units of $\frac{2\pi}{a}$. The bold line shows the scan direction through the 2D Brillouin zone. The figure is taken directly from Coldea *et al.*[33].

berg model, though surprisingly accurate at all points in the Brillouin zone except from $(\pi, 0)$, do not facilitate the complete understanding of the 2DQHAFSL. Therefore other ideas has emerged.
In [23] Christensen *et al.* notes by reference to two earlier work by Anderson *et al.* [14] and Reger *et al.* [32], that the static magnetic moment of the 2DQHAFSL is only about 60% of what is expected from classical theory. The paper by Reger *et al.* also discusses the subject of possible longe range order in the antiferromagnet and concludes that at zero temperature the 2DQHAFSL experiences long range AFM order, albeit with a staggered momentum reduced to about 60 % of its saturation value, due to quantum fluctuations [32]. This changes dramatically when the temperature is raised above 0 Kelvin, where longe range order is destroyed by thermal fluctuations and the ordering is reduced to short range, described by the correlation length $\zeta(T)$ [19]. In this paper from 2001 Rønnow *et al.* presents an overview of already settled topics and questions that remain unanswered for the scientific world. According to this, a full understanding of the correlation length for temperatures $J/5 < T < J$ has been obtained through various experimental and numerical techniques and it is the spin dynamics that remain the interesting topic from a research perspective.
Summarizing, there are many indicators telling us that new or modified models must be made, if the spin dynamics of the 2DQHAFSL are to be understood. These indicators are among others:
i) It has been calculated that the ground state energy of the 2DQHAFSL is lower than that of the Néel state [32], who find that that $\frac{E}{E_{Nel}} = 1.340 \pm 0.004$.

[5]See Eqn. (2.77).

ii) The static magnetic moment is only about 60 % of what is expected classically [14, 32].
Based on the above review, it seems reasonable to expect some degree of correlation between the electrons on the square lattice, despite the fact that this existence has not yet been proven by experiment. As mentioned in Chapter 2, various groups have followed the RVB idea e.g. Dagotto *et al.* and Christensen *et al.* [30, 23].

3.1.3 Discussion on the experimental situation

The literature contains numerous results which deliberately have been left out, since the picture at this stage should be clear: Experiments have shown that the quantum magnetical quadratic lattice possesses a pronounced anomaly relative to what is expected from LSW theory, in particular near $(\pi, 0)$. This anomaly manifests itself in both the energy dispersion and the scattering intensity. The anomaly can be modeled by various models including the Heisenberg model with nearest plus next-nearest neighbor interaction[6], and an extended Heisenberg model[7] including a four spin ring exchange[8]. As was noted in at least one case by Coldea *et al.* the different models do not always produce consistent values for the underlying physics, despite the the fact that they are obtained from data fitting which seems convincing. In other words, it is from experiment not possible to unambiguously determine the physics behind the $(\pi, 0)$ anomaly.

The lack of unambiguous experimental results that can answer the questions that the $(\pi, 0)$ anomaly brings about, demands the use of other methods to study the quantum magnetical systems. One answer to this challenge is numerical studies on small square lattices, with the number of sites reaching from what can be counted on two hands and up to a few hundreds. The status of numerical studies will be introduced in chapter 4 by a summary of the results presented in the literature until today. In chapter 6 will follow a presentation of the numerical studies of this thesis work.

[6] See Sec.2.3
[7] See Sec. 2.7.2.
[8] Finally there is the possibility of an series expansion from the Ising limit which we have not treated here.

Chapter 4

Numerical work on 2DQHAFSL

The literature presents a number of papers containing numerical work on the 2DQHAFSL and this chapter will go through a selection of those, relevant to this thesis. 'Numerical studies' is an umbrella term for various methods of numerical computations. Within numerical studies one distinguishes between 'exact' and 'non-exact' methods. Using exact numerical methods, the obtained results are exact in the sense, that the they will be consistent[1] with an analytical result that in principle could be reached, if one had enough pencils, paper and time. Contrary to this is f.x. Quantum Monte Carlo, which is based on probability algorithms.
Before starting our review it is relevant to line up a few conditions under which numerical work must be done. It is self evident, that the more calculations needed, the longer time the calculations take. Hence, the scientist working with numerical studies must at all times have the number of calculations in mind, in order not to exceed the limit for what is possible on a cluster of computers. For a N-site system the number of states in the Hilbert space are 2^N which is exponentially increasing in the number of sites. Hence the first limitation we face, is the size of the system possible to simulate.

4.1 QMC

This ultra-short resume on QMC is written by inspiration from a report on the topic [41].
One of the widest used 'non-exact' numerical methods is Quantum Monte Carlo simulations (QMC). The advantage of this method is that larger systems can be investigated than when using exact methods. The disadvantage of QMC is, that it relies on stochastic processes and can as such be encumbered with uncertainty. In the following the idea behind QMC will be sketched briefly.
In QMC one is interested in determining the thermal average $\langle A \rangle = \sum_s A_s W_s$ of an observable A, where A_s are the possible values of A and W_s are their weights. The way to do this by a real experiments, is by performing a large number N of experiments and then taking the mean value. When N goes towards infinity this mean value approaches the thermal average.
In QMC the weights W_s are are given by the Boltzmann distribution

$$W_{s_i} = \frac{e^{\beta A_{s_i}}}{\sum_s e^{-i\beta A_s}} = \frac{e^{\beta A_{s_i}}}{Z} \quad ,$$

where $\beta = 1/T$ is in units of J. Z is known as the partition function, and the number of terms in its sum increases exponentially with the system size. Hence one cannot compute Z

[1] One can never get around numerical rounding errors, but these are negligible in exact numerical work.

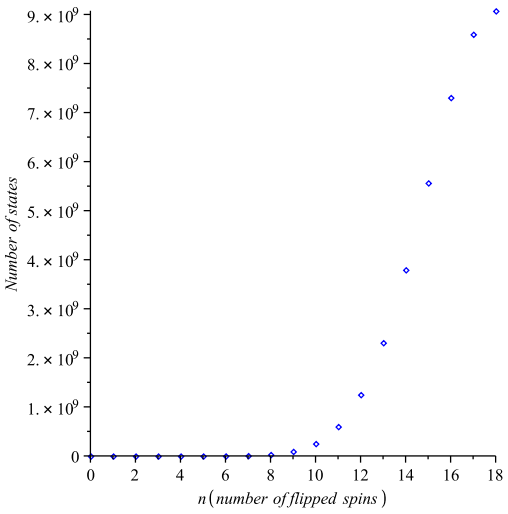

Figure 4.1: The number of states in a m-invariant subspace of the 2^N-dimensional Hilbert space is given by the binomial coefficient $\binom{N}{n}$. In this figure $N = 36$ giving that $n = 0$ corresponds to $m = 18$ and $n = 18$ corresponds to $m = 0$. The number of states are symmetrical around $n = \frac{N}{2} = 18$.

and instead the ratio between two weights are found

$$\frac{W_{s_i}}{W_{s_j}} = \frac{e^{-\beta A_{s_i}}}{e^{-\beta A_{s_j}}}$$

This is clever, since one can generate two configurations s_i and s_j of the system and let the system propagate to the configuration with the highest relative probability[2]. The generation of these configurations are done stochastically, which is the reason for the name 'Monte Carlo'. This thesis will only refer to work based on QMC when directly relevant. For a reference to QMC on the 2DQHAFSL one can read [20].

4.2 Exact Diagonalization(ED)

When one is working with a Hamiltonian having m-symmetry, that is conservation of the total S^z, the 2^N dimensional Hilbert space can for a spin-$\frac{1}{2}$ system be divided into $2N+1$ m-invariant subspaces of which only $\frac{N}{2} + 1$ are morphologically different. In the $m = \frac{N}{2}$ subspace all spins points in the same direction classically speaking, and hence the number of states are no more than N. Decreasing the value of m from $m = \frac{N}{2}$ the dimensionality of the sub-Hilbert space is given by the binomial coefficient $\binom{N}{n}$, where n are the number of spins pointing opposite to the rest. The number of states as a function of the number of flipped spins for a 36 spin lattice is seen in Fig. 4.1, from which it is clear that the most cost full calculations correspond to low values of m.
It follows that the higher the m-value, the larger the system can be simulated. This can be exploited in some cases, but for the task of finding the ground state energy, this does not help us, since the ground state only lives in the $m = 0$ subspace.

[2]There exist various QMC algorithms, each having constraints on the propagation. This will however be too far from the topic of this thesis to treat here.

Exact numerical work is in its essence 'to diagonalize the Hamiltonian', and this is exactly what Exact Diagonalization (abreviated ED) refers to. For a 36 spin lattice with dimensionality $2^{36} \approx 9 \cdot 10^9$ this is absolutely impossible by brute computer force, since the corresponding matrix is almost 10^{10}x10^{10}. One therefore has to use advanced diagonalization algorithms, that can decrease the dimension of the matrix to be diagonalized, while the eigenenergies and eigenstates are unaffected. A choice for such an algorithm is the Lanczos algorithm, see Sec.5.4, which has been used in a number of studies (f.x.[30]). This algorithm is indeed the mathematical cornerstone in RLexact, used in this work.
As long ago as in 1988 Dagotto *et al.* published their numerical studies of the 2DQHAFSL by exact diagonalization using the Lanczos algorithm [30]. At that time the computational power limited their studies to systems of maximally 24 sites with $m = 0$. This limit has gradually increased ever since and today it seems that the limit is 36 spins for $m = 0$.
When summarizing the numerical work in the field of 2DQHAFSL one paper by Lüscher and Läuchli [39] stands out, both with regard to care and extend. The paper presents work on finite clusters that for $m/N = 0$ handles lattices up to 32 spins and for non-zero m/N deals with samples up to 64 sites. The paper presents numerous calculations of which we shall only treat the ones relevant for this thesis. This amounts to magnetization curves, susceptibility, energy dispersions, dynamical structure factors and staggered magnetization.

The Hamiltonian governing the simulations of Lüscher *et al.* is the Heisenberg Hamiltonian Eqn. (2.1) with nearest neighbors. Based on this Hamiltonian, we shall start by presenting what is known as the ground state magnetization curve, defined for $m = 0$.
As described in Fig. 2.1 the spins considered as classical vectors, will gradually align along an applied field when the strength is increased. This means that state with the lowest lying energy, for an increasing field has an m-value increasing in integral steps, resulting in the magnetization curve $m(h)$ being a step function[3]. In the thermodynamic limit where $N \to \infty$ the number of steps N goes towards infinity, and since they all have to fit into the interval $h \in [0; 4]$[4], the step length goes towards zero. I.e. in the thermodynamic limit the magnetization curve becomes continuous. Such a continuous magnetization curve is seen in the inset of Fig. 4.2. Here the dashed line is the classical curve. Open squares are due to ED from clusters of at least 40 sites [39] and open triangles are QMC at $T \leq 0.02J$. It is from [39] not clear how this extrapolation is made.
The magnetization curve can be considered as the conversion between h and m, making the last term in Eqn. (2.1) expressible by m instead of h. Since real experiments at nonzero h are always expressed by the value of h, it can in order to increase the clearness be relevant to express numerical experiments by the value of h corresponding to the value of m, under which the numerical calculations were performed. Actually the way to do numerical work at nonzero fields *is* to carry out calculations at the corresponding nonzero m. In effect, the conversion m to h is done by the inverse of $m(h)$. This can either be determined by a polynomial fit to the data points in the m vs. h plot or by derivation through LSWT, of which [39] have used the latter.
The main panel of Fig. 4.2 reveals, that the numerical calculations (QMC and ED) captures a behavior of the magnetization curve $m(h)$, not possible to obtain from LSW theory (the solid line). However, the deviations in $m(h)$ between LSWT and numerical work (ED and QMC) are everywhere smaller than 5%, a fact that is used as a justification for using the LSW prediction for $m(h)$ as the convesion between m and h.
Before leaving Fig. 4.2 one should note that the deviation between LSWT and numerical re-

[3]For a more detailed explanation of this, see Sec. 6.1.
[4]Since the saturation field is $h_s = 8JS = 4$, $J = 1$.

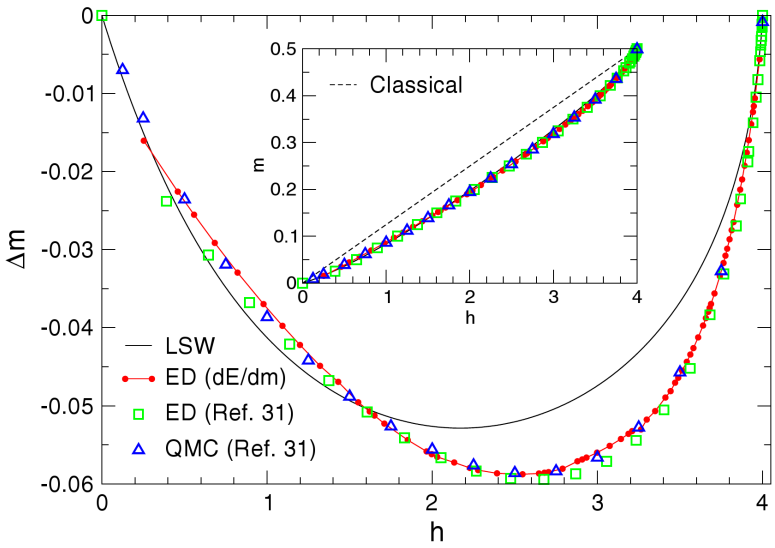

Figure 4.2: Inset: Uniform magnetization m as a function of applied field h. The dashed line is the classical curve, the solid line is the LSW result, small red dots are obtained from the derivative of the ground state energy extrapolated to the thermodynamic limit. Open squares are ED results from clusters with at least 40 sites and open triangles are QMC at $T \leq 0.02J$. The inset displays the magnetization curve $m(h)$ as described in the text. Main panel: The deviation between the ED results and the classical prediction, that is $\Delta m(h) = m(h) - m_{cl}$. The picture is taken directly from [39].

sults are not symmetric around $h = 0$ as one could naively expect. The lack of symmetry in the deviation is explained by considering the situation with $m = 0$, in which no alignment of spins are present, and the situation in which $m = N/2$, in which all spins are aligned. When h is increased/decreased respectively toward $h = 2$ from these two configurations, it is seen that the physics is not symmetric at all, due to the different starting points: In both cases one spin will be flipped, but from a starting point with no alignment and full alignment respectively.

We shall now proceed to another physical observable reachable by numerical work. Having obtained an expression for $m(h)$, the magnetic susceptibility which is given by[5] $\chi = \frac{\partial m}{\partial h}$ is within reach, being obtainable from the magnetization curve $m(h)$ by simple differentiation. A curve for the susceptibility is seen in Fig. 4.3, which reveals that the data points from both QMC and ED are described surprisingly well by the LSW prediction (solid line). It is also noted that the classical result represented by the dashed line does not capture the quantum mechanical susceptibility. The divergence at $m = 0.5$ is due to the slope of $m(h)$ going towards infinity at the point $(h, m) = (4, 0.5)$ on the magnetization curve.
Inspecting Fig. 4.3 the before mentioned asymmetry is once again visible, though in a somewhat different version. It is clearly seen, that the susceptibility is neither anti-symmetric around the line $\chi = 0.125$ nor the line $m = 0.25$. By inspecting the inset in Fig. 4.2 it is seen that the slope of the line based on numerical data points are not symmetric neither wrt. the midpoint of the classical dashed line nor the line $h = 2 \sim m = 0.25$, leading to the asymmetry of Fig. 4.3. That the deviations between the classical and numerical results in both Fig. 4.2 and 4.3 are smaller for low h (and low m) than for large h (and large m), tells us that the

[5] See Sec. 2.2

finite samples on which the numerical work are performed, behave more quantum mechanically at high fields ($h \approx 3$) than at low fields ($h < 2$).

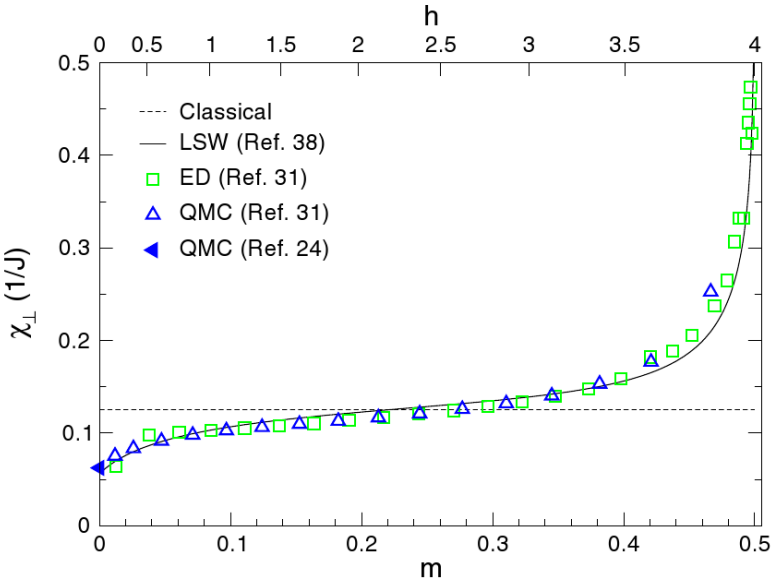

Figure 4.3: Transverse susceptibility χ as a function of the magnetization m and the applied field h. The dashed line are the classical curve, the solid line is the LSW result and the data points are obtained by both QMC and ED. The picture is taken directly from [39] FIG. 4.

4.2.1 The longitudinal dynamical structure factor $S^{zz}(\mathbf{q},\omega)$

We shall now jump to a variable which is directly comparable to real experiments. As mentioned previously the aim of numerical studies is to simulate real experiments as they ideally would come out on pure systems, and therefore it is highly relevant to treat the dynamical structure factor $S^{\alpha\beta}(\mathbf{q},\omega)$ where $\alpha,\beta \in \{x,y,z\}$, defined in Eqn. 2.64. We shall however, only be concerned with results displaying the structure factor $S^{zz}(\mathbf{q},\omega)$, since this is what RLexact is capable of calculating for a two dimensional sample. In order to plot $S^{zz}(\mathbf{q},\omega)$ together with the corresponding energy and q-vector, one needs to plot three variables, i.e. a 3D plot. This is a problem, since 3D plots can be inexpedient due to their visual complexity. Fortunately there is a way to avoid this. In a (Q_{2D},ω) coordinate system the value of $S^{zz}(\mathbf{q},\omega)$ is plotted by a circle, such that the area of the circle is proportional to value of $S^{zz}(\mathbf{q},\omega)$. The paper by Lüscher *et al.* [39] presents a very profound work investigating the dynamical structure factor. We shall in this short review on the status of numerical work present a few selected figures, but the reader is encouraged to read the paper for a complete picture.
For this review is chosen six pictures displayed in Fig. 4.4, and it is worth noting a couple of features of the plot. We start examining the upper left panel:
i) It is seen that the dominating structure factors[6] belong to the highly symmetric X-point (π,π) and Γ-point $(0,0)$. Their corresponding energy is almost zero. These two poles we shall name the magnon poles. The reason that the energy of the magnon poles are not exactly zero, is due to a finite size effect, that scales[7] like $1/N$, classifying the mode as a Goldstone mode

[6] Note that the structure factor in $\mathbf{q} = (0,0)$ (the Γ-point) is removed from all plots. This is because it is so big, that it would cover a great part plot for $h > 0$.

[7] See Fig. 6.8 in Sec. 6.3.

in the thermodynamical limit.
ii) As the field is increased, the pole at the X-point suddenly jumps in energy indicating that an energy gap has been established (the Goldstone mode of $h = 0$ has vanished). As is indicated by the second panel of Fig. 4.4, this jump is provoked by even a small increase in the field away from zero. We shall return to this in Chapter 6. One also notes that the data is still well described by LSW theory.
iii) At $h = 2.02$ the structure factor at the X-point starts to rise in energy, leaving the LSW prediction incorrect at this point. When the field is increased even higher (at $h = 3.16$) the behavior at the X-point is once again captured satisfactory by LSW theory, but at new feature has occurred:
iv) The splitting in two energy branches between the M-point $(\pi, 0)$ and the S-point $(\frac{\pi}{2}, \frac{\pi}{2})$. At $h = 3.33$ this branch splitting is still present, but at $h = 3.79$ it seems as if the two branches have begun melting together. That the branch splitting occurs between $(\pi, 0)$ and $(\frac{\pi}{2}, \frac{\pi}{2})$ is very interesting, having in mind the $(\pi, 0)$ anomaly. A further comment to this path in the scan, is that the position of the poles wrt. the LSW prediction is reversed when the field increases: For $m \lessapprox 1/8$ the poles are higher lying than the LSW prediction and the slope (of a line through them) are positive in the scan direction. For $m \gtrapprox 1/8$ both these two features are reversed.
v) Another feature is very clear from the lower row: The structure factor at the X-point, that for zero and low non-zero field had the dominating spectral weight, has clearly decreased in intensity. Although still being relatively strong, it has a magnitude comparable with the remaining structure factors, which have increased their spectral weight markedly. The results is that the spectral weights are distributed relatively evenly throughout the scan at $h = 3.79$. One also notes that at this field the data is very well described by LSWT.
vi) One feature has to be commented when examining Fig. 4.4 as a whole. From fields up to $h \approx 2$ there is a clear gap between the one-magnon excitations corresponding to the big circles and the densely placed smaller poles, referred to as the two- and multi-magnon excitations. Above $h \approx 2$ this continuum approaches the one magnon excitation branch from above, connecting with it for $h \approx 3$ in all points except between M and S. Increasing the field even more eventually results in the disappearance of the two- and multi magnon continuum, as is seen in the last picture of Fig. 4.4.
vii) The thin pink line in the last two panels connects the lowest lying poles of the 64-site cluster. It is interesting that the shape of this line resembles that of the main branch poles. The paper notes that the possibility of resolving poles with little spectral weight is a conceptual advantage of ED compared to QMC.

4.2.2 The staggered magnetization

The staggered magnetization which are defined in Eqn. (2.71) and (2.76), has as discussed earlier, been investigated by many different methods. In this review the result by Reger *et al.* [32] is presented in Fig. 4.5. The value of $m^\dagger$ are determined by a $1/L$ interpolation of two different variables (see caption) to be $m^\dagger = 0.30(2)$, consistent with experimental observations by N.B. Christensen *et al.* [23]. Note that the interpolation used by [32] is a $1/L$ interpolation, where the square lattice are $LxL = N$. In the Sec. D.1 of the appendix an alternative presentation of the staggered moment by Lüscher *et al.* is presented for reference.

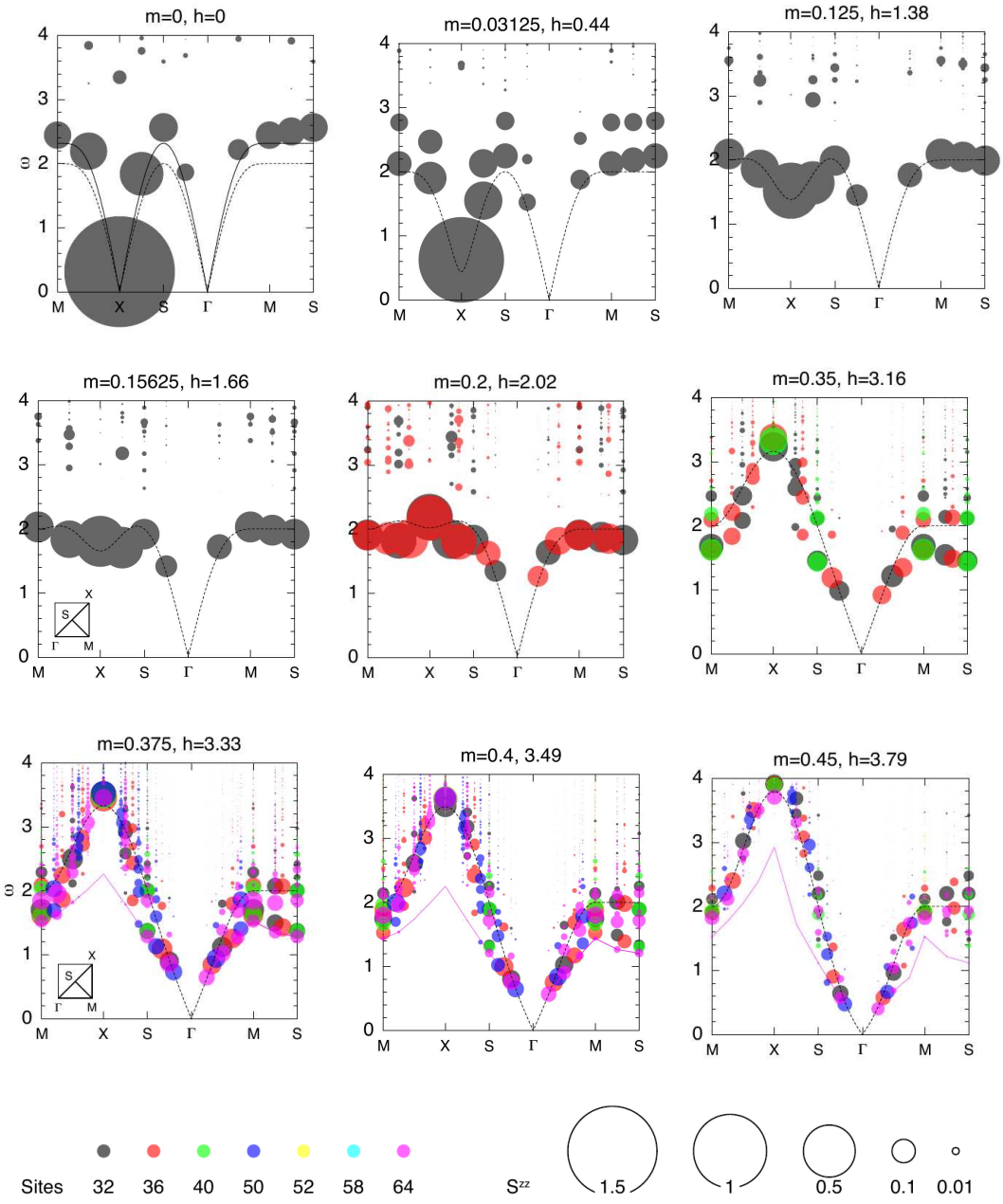

Figure 4.4: The area of the circles is proportional to the longitudinal structure factor $S^{zz}(\mathbf{q},\omega)$ and the center of the circle(Q_{2D},ω) points out the corresponding point in Q_{2D}-space with belonging energy given in units of J. The color tells from which samples the data is obtained. The dashed line is the dispersion obtained from LSW theory and the solid line in the picture for $h = 0$ is LSW theory with first order corrections. The thin pink line in the last two panels connects the lowest lying poles of the 64-site cluster. The values of m and h are seen at the very top of each picture frame. The picture is modyfied from [39].

4.2.3 Discussion on the status of numerical work

As pointed out by Lüscher and Läucli [39] one should be careful in interpreting ED results based on near-saturation fields. The reason is that the basis of the Hilbert space with only a

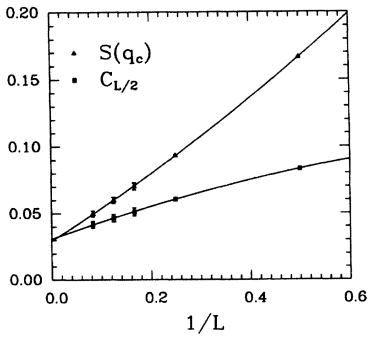

Figure 4.5: The staggered moment $m^\dagger$ vs. $1/L$ determined by a $L \to \infty$ interpolation by two methods. Here the notation $LxL = N$ for the square lattice. $C_{L/2}$ represents the correlation between spins as far apart as possible and $S(q_c)$ are the mean square staggered magnetization, which except for a different normation are similar to Eqn. (2.75).

few spins flipped ($\binom{N}{m}$) $\sim 10^1 - 10^2$, N is the number of sites and m are the number of spin-up ions) is so small that it is not representative for a thermodynamically big system. For this reason Lüscher and Läuchli only present results where $m \leq 1/2 - 4/N$.
We shall divide the discussion into the various topics discussed above. Starting with the magnetization it is clear that the results based on ED and QMC coincide satisfactory, agreeing upon a curve somewhat different from the LSW result, though not dramatically different. The deviation to the classical result is huge in all three cases. These conclusions can be carried directly over to the susceptibility, since it is related to the magnetization by differentiation.
Continuing to the dynamical structure factor the conclusions of Fig. 4.4 can be summarized to the following:
a) The spectral weight that for zero field is concentrated at (π, π) gradually smears out over the entire BZ when the field strength is increased. This can be understood from the reduced symmetry introduced by the field, which, when increased, gradually destroys the symmetry in the X-point, such that all points in the BZ have equal spectral weights in the saturated limit.
b) The energy of the X-point excited magnons is increasing for increasing field, and the Goldstone mode present at zero field vanishes as soon as the field is turned on. The latter is most clearly seen from the second panel of Fig. 4.4. To understand this, one should keep in mind, that a Goldstone mode implies that an arbitrarily small energy will create an excitation of the system. This is not possible when a field is present, since all spins now have a preferred direction, from which they are turned away only by a finite energy. It appears that the ED results at the X-point in general have slightly higher energy than the LSW prediction. This is probably due to a finite size effect which we will return to in Chapter 6. The paper further notes that the finite gap now characterizing the X-point is proportional to the field.
c) The gap between the one-magnon excitations and the two- and multi-magnon continuum closes for increasing field, such that at fields close to saturation only one relatively well defined branch exists (except between M and S). This branch will equal the ferromagnetic dispersion when saturation is reached, see. Eqn. (2.62) and Fig. 2.5. d) The observed branch splitting seems to consist of two branches. One branch is well described by the LSWT, though slightly higher lying in energy. The other branch separates somewhere between the Γ- and M-point, having a local peak at $M = (\pi, 0)$ and deviating maximally from the LSW-like branch at S. Judging from the last two pictures of Fig. 4.4, it seems as if the non LSW-like branch melts together with the LSW-like branch rather suddenly somewhere close to saturation, forming

a smeared out branch between M and S at the second-highest field investigated (second-last panel of Fig. 4.4). In this connection it is interesting that the pink line in the last two panels, connecting the lowest lying poles, maintains its shape independent of the field.

Having presented necessary theory and outlined the status on experimental and numerical work in the first four chapters of this thesis, we are now ready to move on to the presentation of the results of this thesis work. The Results are presented in Chapter 6. Chapter 5 is an outline of the details of RLexact.

Chapter 5

RLexact

5.1 Introduction

The number of states even in a relatively small lattice is enormous. Recall that N sites each with the possibility of either a spin-up or a spin-down ion results in 2^N possibilities, i.e. a 2^N dimensional Hilbert space. For $N = 36$ the dimension is approximately 64 billions, which makes the matrix $64 \cdot 10^9 \times 64 \cdot 10^9$. As mentioned it is impossible to solve eigenvalue problems of such systems by brute force, with the aid of todays computers. This is due to two factors: 1) Calculation time and 2) RAM for saving the necessary results. The complexity and magnitude of steps in the procedure would reach such a high number, that it would not be possible to obtain a result within a reasonable time, even with great access to RAM. The systems treated in this work consists of 8, 16, 32 and 36 spins, making it necessary somehow to reduce the number of steps leading to a final result. This is done in two ways: *i*) By symmetry considerations the matrix representing the original 2^N dimensional system, which due to the form of the Heisenberg Hamiltonian (2.2) is relatively sparse[1], is transformed into block diagonal form and the matrices of smaller dimension can then be handled separately. There are two types of symmetries to exploit; m-symmetry and translational symmetry. This we will return to in the next section. *ii*) Since the block matrices of reduced dimension is still very large, one applies some kind of computational procedure which (often) at the cost of precision in the solutions makes the problem practically solvable for a cluster of computers. Many such procedures exists and we shall in this work make use of a procedure known as Lanczos algorithm. Lanczos algorithms is a generic term for a class of algorithms suitable for determining extreme eigenvalues for huge matrices and for our purpose we will use the algorithm suitable for hermitian matrices.

5.2 The symmetries

One of the basic results of quantum mechanics is the existence of a complete set of common eigenvectors for two commuting operators. This result turns out to be of great use in our task of obtaining a numerical result for the ground state of our 2^N dimensional Hilbert space $\mathcal{H}$. The overall idea is to determine all symmetries of our system, that is finding all the symmetry operators that commute with the Hamiltonian $\hat{H}$. For a start we recall some results about the eigen-properties of two commuting operators.

[1] A sparse matrix is a matrix with many zero-entries. Since the Hamiltonian conserves the z-component of spin, only states with the same z-component of spin will be connected by non-zero entries. Furthermore translational invariance will turn out to reduce the complexity of the diagonalization-problem.

If $\hat{A}$ is a operator that commutes with the Hamiltonian $\hat{H}$ and $|\phi_n\rangle$ is an eigenvector of $\hat{A}$ such that $\hat{A}|\phi_n\rangle = a_n|\phi_n\rangle$, the following identities can be obtained

$$\hat{H}(\hat{A}|\phi_n)\rangle = \hat{H}a_n|\phi_n\rangle = a_n\hat{H}|\phi_n\rangle$$

and

$$\hat{H}\hat{A}|\phi_n\rangle = \hat{A}\hat{H}|\phi_n\rangle$$

From which it can be deduced that

$$\hat{A}(\hat{H}|\phi_n\rangle) = a_n(\hat{H}|\phi_n\rangle)$$

This proves that $\hat{H}|\phi_n\rangle$ is an eigenvalue of $\hat{A}$, with the same eigenvalue as $|\phi_n\rangle$ has wrt. $\hat{A}$. Hence, the eigenvalues of $\hat{A}$ is invariant under $\hat{H}$. If the matrix for $\hat{H}$ is written such that basis vectors with the same eigenvalue of the symmetry operator $\hat{A}$ is grouped together, then $\hat{H}$ will consist of invariant diagonal blocks, where the invariance refers to the fact that $\hat{H}$ will only mix states if they belong to the same block.
If we identify another symmetry of the system represented by the operator $\hat{B}$, such that $[\hat{A}, \hat{B}] = [\hat{H}, \hat{B}] = 0$, then the blocks of $\hat{H}$ can be diagonalized to even smaller blocks by ordering the basis vectors of the $\hat{A}$-invariant subspace of $\hat{H}$ cleverly[2].

m-symmetry

If we turn to the Hamiltonian in question - the Heisenberg Hamiltonian Eqn. (2.2), it follows by inspection of the various terms, that the z-component of the total spin $\mathbf{S} = \sum_i S_i$ is conserved. The argument is simple: The first term $\mathbf{S}_i^z\mathbf{S}_j^z$ basically counts the number of spin-ups, hence not being capable of changing the z-component. The two last terms of Eqn. (2.2) takes the form $\mathbf{S}_i^+\mathbf{S}_j^-$ and $\mathbf{S}_i^-\mathbf{S}_j^+$ which clearly adds a spin-up (down) at site i when a spin-up (down) is removed at site j. Hence there is no overall change in z-component of the total spin. Altogether the Heisenberg Hamiltonian conserves the total z-component of spin. This symmetry will be denoted m-symmetry[3] and the standard basis continues to be the appropriate basis, when the order is changed such that m-invariant blocks appear. This is because m is the S^z quantum number.

Translational symmetry

The second symmetry we will exploit is the translational invariance that follows by assuming that our system will coincide with itself if being translated by a lattice vector. The Square lattice that we work with clearly has two directions in which a translation along a lattice vector exist. The lattice vectors are $(1, 0)$ and $(0, 1)$. We will denote the corresponding operators that translate the entire system either in the x direction or in the y direction, by $\hat{T}_x$ and $\hat{T}_y$ respectively. The effect of the translation operator is that when applied a certain number of times denoted N_x, then the entire crystal is taken into itself due to periodic boundary conditions. The Translation Operator is defined through its eigenvalue equation

$$\hat{T}_x|\Psi\rangle = e^{2\pi i\frac{k_x}{N_x}}|\Psi\rangle \tag{5.1}$$

[2]Note the the relation $[\hat{A}, \hat{B}] = [\hat{H}, \hat{B}] = 0$ is important, since if this were not so, $\hat{H}$ would not be diagonalized further by the $\hat{B}$-symmetry, hence merely offering an alternative but not improved block diagonalization of $\hat{H}$

[3]Such that the name is consistent with the notation used to comment the program code.

such that $\hat{T}_x^{N_x}|\Psi\rangle = e^{2\pi i k_x}|\Psi\rangle$, making the N_x different k_x values $k_x = 0, 1, N_x - 1$ the appropriate quantum number to label the translation eigenvectors and eigenstates. Generalizing to two dimensions we can then write the eigenvalue of the translation operator as $e^{\mathbf{k}\cdot\mathbf{R}}$, remembering that $\mathbf{k}\cdot\mathbf{R} = 2\pi i(k_x n_x + k_y n_y)$, where n_x, n_y and k_x, k_y are the two principal components of the lattice vectors in direct- and reciprocal lattice respectively.
The task is then from the standard basis to construct new basis vectors for the translation operator. If we limit ourself to combine elements from the standard basis only within each block dictated by m-symmetry, these new basis vectors have the property of block diagonalizing each block, if they are ordered cleverly. If we consider a $LxL \equiv N$ spin square lattice the number possibilities for the values of k_x and k_y is for both exactly N. The only exception is for $m = \pm\frac{M}{2}$ where the lattice is taken into itself already by one translation, resulting in just one value for k_x and k_y respectively.
This means that every original block except for the $m = \pm\frac{N}{2}$ block, due to m-symmetry can be split up in exactly L more sub-blocks, independent of the size of the original block.
To understand that every original block does not have the same dimension, recall that the subspace with $m = m_{max} = \frac{N}{2}$ is spanned by only one state, namely the one with all spins pointing up. The subspace with $m = m_{max} - 1$ is spanned by N states, since the configuration of the remaining sites are given, when the one and only spin-down site is placed. This can be done in N ways. Continuing with the subspace of $m = m_{max} - 2$, it is spanned by $\binom{N}{2}$ states, since this is the number of ways one can place two spin-downs at N sites. Generalizing the dimensions of the original blocks with $m = m_{max} - i$, the dimensionality is given by $\binom{N}{i}$, $i = 1, 2, \ldots, \frac{N}{2}$. For $i = \frac{N}{2}, \ldots, M$ the situation is symmetrical corresponding to placing $i = 1, 2, \ldots, \frac{N}{2}$ spin-ups.
The above means that the subspaces of $\hat{H}$ onto which the Lanczos algorithm is applied has increasing size up to a certain limit given by $\frac{\binom{N}{N/2}}{L}$. In Fig. D.2 and Fig. D.3 the dimensions of the original m-blocks of the Hamiltonian are seen.

5.3 The Uniques

It is necessary to minimize the amount of RAM needed to carry out the exact diagonalization of large matrices. The way this is handled in RLexact is by the introduction of uniques, here denoted $|u\rangle$. A unique represents a state of the system and it is like all other states represented by a bitmap. The special thing about uniques, is that they can be translated along the x- and y direction a number of times, to obtain the other states of the system. A unique has the property that it cannot be obtained by translation of any other unique - hence the name. The concept of uniques lowers drastically the demand to RAM, since these are the only configuration-vectors (bitmaps), that has to be stored by the computer. In order to illustrate how RLexact carries out the block diagonalization expressed by the uniques, the simplest system that displays the complexity of the square lattice and still being doable by hand, will be examined. This is a 2x4 lattice.

5.3.1 The 2x4 square lattice in the $m = 0$ subspace

The aim of this subsection is to calculate the matrix of $\hat{H} = \hat{H}_{zz} + \frac{1}{2}\hat{H}_{\pm}$ in the subspace of $m = 0$, in which the ground state is found. In other words we will explicitly write down the block of $\hat{H}$ with $m = 0$, for two arbitrarily chosen $\mathbf{q}$'s, namely $\mathbf{q} = \binom{0}{0}$ and $\mathbf{q} = \binom{3}{1}$.
The 2x4 lattice has eight sites and for $m = 0$ we have four spin-up and four spin-down ions. Taking the possibilities for the spins on each site to be either up or down, one should from the

binomial coefficient expect $K(8,4) = 70$ different states, since all the spin-downs(ups) are given once having placed the spin ups(downs). A closer examination reveals that twelve uniques is needed to obtain the 70 states by x- and y translation. These uniques are

$$
\begin{array}{lll}
|1\rangle = \left| \begin{array}{cccc} 0 & 0 & 0 & 0 \\ 1 & 1 & 1 & 1 \end{array} \right\rangle & |2\rangle = \left| \begin{array}{cccc} 0 & 0 & 0 & 1 \\ 1 & 1 & 1 & 0 \end{array} \right\rangle & |3\rangle = \left| \begin{array}{cccc} 0 & 0 & 0 & 1 \\ 1 & 1 & 0 & 1 \end{array} \right\rangle \\
|4\rangle = \left| \begin{array}{cccc} 0 & 0 & 0 & 1 \\ 1 & 0 & 1 & 1 \end{array} \right\rangle & |5\rangle = \left| \begin{array}{cccc} 0 & 0 & 0 & 1 \\ 0 & 1 & 1 & 1 \end{array} \right\rangle & |6\rangle = \left| \begin{array}{cccc} 0 & 0 & 1 & 1 \\ 0 & 0 & 1 & 1 \end{array} \right\rangle \\
|7\rangle = \left| \begin{array}{cccc} 0 & 0 & 1 & 1 \\ 1 & 1 & 0 & 0 \end{array} \right\rangle & |8\rangle = \left| \begin{array}{cccc} 0 & 0 & 1 & 1 \\ 0 & 1 & 1 & 0 \end{array} \right\rangle & |9\rangle = \left| \begin{array}{cccc} 0 & 0 & 1 & 1 \\ 0 & 1 & 0 & 1 \end{array} \right\rangle \\
|10\rangle = \left| \begin{array}{cccc} 0 & 0 & 1 & 1 \\ 1 & 0 & 1 & 0 \end{array} \right\rangle & |11\rangle = \left| \begin{array}{cccc} 0 & 1 & 0 & 1 \\ 0 & 1 & 0 & 1 \end{array} \right\rangle & |12\rangle = \left| \begin{array}{cccc} 0 & 1 & 0 & 1 \\ 1 & 0 & 1 & 0 \end{array} \right\rangle
\end{array}
$$

The binary notation used by the computer is adapted here, so that 0 and 1 represent spin down and spin up respectively. Each unique represents a number of states, that can be obtained by translation. The number of states represented is not the same for all uniques, which can be seen from table 5.1[4] The idea then, is to represent the matrix of $\hat{H} = \hat{H}_{zz} + \frac{1}{2}\hat{H}_{\pm}$ in the basis of certain linear combinations of uniques, which are eigenstates for the translation operator $\hat{T}_{(x,y)}$. Since all 70 states can be created from the twelve uniques, all states can also be created from linear combinations of these translation eigenstates. Formally the linear combinations are made as follows:

A Total Translation Operator $\hat{T}_T$ is defined as

$$\hat{T}_T = \sum_{j=0}^{3} \sum_{j'=0}^{1} e^{2\pi i(\frac{q_x}{N_x} j + \frac{q_y}{N_y} j')} \hat{T}_{(x,y)} \tag{5.2}$$

where $\mathbf{q} = \binom{q_x}{q_y}$, $N_x = 4$, $N_y = 2$ and finally $\hat{T}_{(x,y)}$ is the usual translation operator defined in Eqn. 5.1, that translates the system by the vector $\binom{x}{y}$ along x and y respectively. The linear combination of the uniques are then defined as

$$|\Phi_n^q\rangle = \hat{T}_T |u_n\rangle \tag{5.3}$$

where $|u_n\rangle$ is the n'th unique. Having in mind that $[\hat{H}, \hat{T}_{(x,y)}] = 0$ it follows that $[\hat{H}, \hat{T}_T] = 0$ and one gets that

$$
\begin{aligned}
\hat{H}|\Phi_n^q\rangle &= \hat{H}\hat{T}_T|u_n\rangle = \hat{T}_T\hat{H}|u_n\rangle \\
&= \hat{T}_T \sum_m a_m e^{2\pi i(\frac{q_x}{N_x} j_m^x + \frac{q_y}{N_y} j_m^y)} |u_{l(m)}\rangle \\
&= \sum_m a_m e^{2\pi i(\frac{q_x}{N_x} j_m^x + \frac{q_y}{N_y} j_m^y)} \hat{T}_T |u_{l(m)}\rangle \\
&= \sum_m a_m e^{2\pi i(\frac{q_x}{N_x} j_m^x + \frac{q_y}{N_y} j_m^y)} |\Phi_{l(m)}^q\rangle
\end{aligned} \tag{5.4}
$$

The expression $\sum_m a_m |u_{l(m)}\rangle$ in the second line is the result of letting $\hat{H}$ work on $|u\rangle$, seen in fourth and fifth column of table 5.1. That $\hat{T}_T|u_{l(m)}\rangle = |\Phi_{l(m)}^q\rangle$ in the last line, follows from the definition Eqn. (5.3) and once again the fourth or fifth column of table 5.1.

[4] The number of states represented by each unique has to be found systematically by hand, and cannot be "'seen easily"'.

$\|u\rangle$	a_n	$\hat{H}_{zz}$	$\frac{1}{2}\hat{H}_{\pm}\|u\rangle, \mathbf{q} = \binom{0}{0}$	$\frac{1}{2}\hat{H}_{\pm}\|u\rangle, \mathbf{q} = \binom{3}{1}$
$\|1\rangle$	2	0	$2\|2\rangle$	Not defined
$\|2\rangle$	8	-2	$2\|1\rangle + \|3\rangle + \|5\rangle + 2\sqrt{2}\|7\rangle + 2\|12\rangle$	$\frac{1-i}{2}\|3\rangle + \frac{1+i}{2}\|5\rangle$
$\|3\rangle$	8	0	$\|2\rangle + \|4\rangle + 2\|10\rangle$	$\frac{1+i}{2}\|2\rangle + \frac{1-i}{2}\|4\rangle$
$\|4\rangle$	8	0	$\|3\rangle + \|5\rangle + 2\|8\rangle$	$\frac{1+i}{2}\|3\rangle + \frac{1-i}{2}\|5\rangle$
$\|5\rangle$	8	0	$\|2\rangle + \|4\rangle + 2\|9\rangle$	$\frac{1-i}{2}\|2\rangle + \frac{1+i}{2}\|4\rangle$
$\|6\rangle$	4	2	$\frac{1}{\sqrt{2}}\|9\rangle + \frac{1}{\sqrt{2}}\|10\rangle$	Not defined
$\|7\rangle$	4	-2	$2\sqrt{2}\|2\rangle + \frac{1}{\sqrt{2}}\|9\rangle + \frac{1}{\sqrt{2}}\|10\rangle$	Not defined
$\|8\rangle$	8	0	$2\|4\rangle + \|9\rangle + \|10\rangle$	$\frac{1-i}{2}\|9\rangle + \frac{1-i}{2}\|10\rangle$
$\|9\rangle$	8	-1	$2\|5\rangle + \frac{1}{\sqrt{2}}(\|6\rangle + \|7\rangle) + \|8\rangle + \|11\rangle + \|12\rangle$	$+\frac{1+i}{2}\|8\rangle$
$\|10\rangle$	8	-1	$2\|3\rangle + \frac{1}{\sqrt{2}}(\|6\rangle + \|7\rangle) + \|8\rangle + \|11\rangle + \|12\rangle$	$\frac{1+i}{2}\|8\rangle$
$\|11\rangle$	2	0	$\|9\rangle + \|10\rangle$	Not defined
$\|12\rangle$	2	-4	$2\|2\rangle + \|9\rangle + \|10\rangle$	Not defined

Table 5.1: The result of letting $\hat{H}$ work on the twelve $|u\rangle's$ when $\mathbf{q} = \binom{3}{1}$ and $\mathbf{q} = \binom{0}{0}$ respectively. Column 1: The twelve different uniques for the 4x2 lattice. Column 2: Number of states that each unique represent. Note that the column sums to 70 as necessary. Column 3: Values of the diagonal elements(not depending on $\mathbf{q}$). Column 4: Value of the off diagonal elements when $\mathbf{q} = \binom{0}{0}$. Column 5: Value of the off diagonal elements when $\mathbf{q} = \binom{3}{1}$. Note that all uniques are defined for $\mathbf{q} = \binom{0}{0}$ whilst less uniques are defined for $\mathbf{q} = \binom{3}{1}$.

At this point one has to normalize the basis states involved - a calculation that is a little more subtle than assumed at first sight. The problem is, that each unique $|u\rangle$ by translation represents a different number of states. This means that each basis vector $|\Phi_n^q\rangle$ has the normalization factor $\sqrt{\frac{1}{a_n}}$ and that the resulting basis vectors $|\Phi_{l(m)}^q\rangle$ have the normation $\sqrt{\frac{1}{a_{l(m)}}}$. The a_n and $a_{l(m)}$ is found in the second column of Table 5.1. Taking this potential normation error into account, it turns out that one explicitly must multiply each term of the sum in Eqn. (5.4) with $\sqrt{\frac{a_n}{a_{l(m)}}}$. In order to test the results of RLexact the matrix for two values of $\mathbf{q}$ is made, $\mathbf{q} = \binom{0}{0}$ and $\mathbf{q} = \binom{3}{1}$. For $\mathbf{q} = \binom{0}{0}$ all uniques are defined which is seen from the fourth column of table 5.1, but for $\mathbf{q}$'s different from $\mathbf{q} = \binom{0}{0}$ one has to be alert. As is seen from the second column, the uniques $|1\rangle$, $|6\rangle$, $|7\rangle$, $|11\rangle$ and $|12\rangle$ does translate into eight different states and hence they are not defined for all eight $\mathbf{q}$-vectors (all eight points in q-space). The calculations to determine the not-defined uniques for different $\mathbf{q}$-vectors are found in Sec. B.0.3 of the appendix.
Letting $\hat{H}_{zz} = \sum_{\langle i,j \rangle} \mathbf{S}_i^z \cdot \mathbf{S}_j^z$ operate on the uniques is easy, since it merely count S^z, hence making no difference between the two $\mathbf{q}$-values, since no translation of the product is necessary. One readily obtains column three of table 5.1. The values are simply obtained by carrying out the sum over spin interactions between all nearest neighbor pairs once - avoiding double counting. The energy of the square lattice depends on the $\mathbf{q}$-value and given the relation $\mathbf{q} = 2\pi(\frac{q_x}{N_x}, \frac{q_y}{N_y})$ it follows that (π, π) corresponds to $(q_x, q_y) = (2, 1)$ and $(0, 0)$ corresponds to $(q_x, q_y) = (0, 0)$.
Things get more complicated when $\hat{H}_{\pm}$ is operating on the uniques in order to reach the off diagonal elements. An example of these calculations are found in the Sec. B of the appendix and the results are stated in the fourth and fifth column of table 5.1.

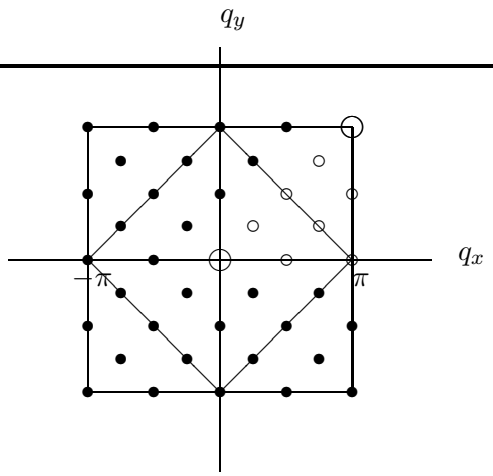

Figure 5.1: The Brillouin zone (BZ) for the $\sqrt{32}$x$\sqrt{32}$ square lattice of 32 spins. The open symbols denote the 9 distinct q-points. The solid symbols are due to symmetry equal (in total there are four 'copies' of each point). The points $(0,0)$ and (π,π) in which the energy takes its minimum is marked by bigger symbols. The biggest square are the structural BZ and the smaller square are the magnetic BZ.

5.4 The lanczos algorithm

The Lanczos algorithms are as mentioned a generic term for a vast number of computing algorithms enabling the user to obtain approximative solutions to the extreme eigenvalues and eigenvectors of large matrices. Since the block diagonal block-matrices, see Fig. D.3, of our system are hermitian, the algorithm that is chosen for this work applies only to hermitian matrices. The first versions of the program code is written by Christian Rischel and Kim Lefmann of the University of Copenhagen, and the math behind it will be explained in this section. After some years the code was further developed by Frederik Treue and in this thesis the author has worked a little bit on the code as well.
The outline is based on [7][Chap. 3], [8][Chap.4, Sec.9] and a program-report by Frederik Treue [40].
The Lanczos algorithm is a method to find the extreme eigenvalues of a matrix. In this case the matrix we are dealing with is the matrix for the Heisenberg Hamiltonian (2.2), and what is of interest is the energetically lowest lying states. Hence, the extreme eigenvalue we seek is the lowest eigenvalue. The algorithm is build upon two main principles:
a) One part of the algorithm finds a set of orthonormal basis vectors $\mathbf{q}_i$ with the property that the Hamiltonian matrix $\mathbf{H}$ will be a tridiagonal matrix[5], $\mathbf{T}$, when projected onto this basis.
b) If the number of basis vectors, $\mathbf{q}_i$, are less than the dimension of $\mathbf{H}$, the latter will be projected onto a subspace of the original Hilbert space, spanned by the $\mathbf{q}_i$'s. In this subspace, $\mathbf{H}$ has been transformed into $\mathbf{T}$ but the extreme eigenvalues of $\mathbf{T}$ will converge to the extreme eigenvalues of $\mathbf{H}$ as more vectors $\mathbf{q}_i$ are added to the basis.

5.4.1 The tridiagonalization method

We shall start this section with a definition.

Definition 1 (Hermitian matrix). *A matrix* $\mathbf{A}$ *is hermitian if and only if* $\mathbf{A} = \mathbf{A}^\dagger$

This means that every entrance satisfies $a_{ij} = a^*_{ji}$, where $*$ denotes complex conjugation. The Lanczos algorithm for a hermitian matrix is a recursive algorithm. The aim of the algo-

[5] In a tridiagonal matrix nonzero elements can only occur in the diagonal and the two sub diagonals.

rithm is to construct the before mentioned real symmetric tridiagonal matrix[6].

$$\mathbf{T} = \begin{pmatrix} \alpha_1 & \beta_2 & & & & 0 \\ \beta_2 & \alpha_2 & \beta_3 & & & \\ & \beta_3 & \alpha 3 & \ddots & & \\ & & \ddots & \ddots & \beta_{m-1} & \\ & & & \beta_{m-1} & \alpha_{m-1} & \beta_m \\ 0 & & & & \beta_m & \alpha_m \end{pmatrix} \tag{5.5}$$

The entries of $\mathbf{T}$ is determined directly by the Lanczos algorithm, which consists of a number of steps.

The first task is to generate the set of orthonormal basis vectors $\{\mathbf{q}_1, \mathbf{q}_2, \dots \mathbf{q}_m\} \in \mathcal{H}$. A unitary transformation matrix $\mathbf{Q}$ having the $\mathbf{q}_i$'s as its columns is then constructed which makes it possible to make the transformation[7]

$$\mathbf{Q}^\dagger \mathbf{H} \mathbf{Q} = \mathbf{T} \tag{5.6}$$

The orthonormal basis vectors are together with the α_i's and β_i's generated recursively by a method which for reference is named *the direct method.*
The first thing to do, is to choose a random complex starting vector $\mathbf{q}_1$ such that $||\mathbf{q}_1||_{\mathbb{C}} = 1$, where the complex norm is defined as $||\mathbf{x}||^2_{\mathbb{C}} = \sum_{i=1}^n x_i^* x_i$ with $x_i \quad , i = 1, 2, \dots n$ being the n components of $\mathbf{x} \in \mathbb{C}^n$. Any vector with the correct norm will do, since $\mathbf{H}$ projected onto a one dimensional subspace is a one by one matrix which clearly is tridiagonal. The elements of $\mathbf{T}$ is found through rewriting[8] Eqn. (5.6) as $\mathbf{HQ} = \mathbf{QT}$. One can by evaluating column-wise obtain the relation[9]

$$\mathbf{H}\mathbf{q}_l = \mathbf{Q}\mathbf{T}_l = \mathbf{q}_{l-1}\beta_l + \mathbf{q}_l\alpha_l + \mathbf{q}_{l+1}\beta_{l+1} \tag{5.7}$$

If $l = 1$ (we are in the first column of $\mathbf{T}$) the first term of the right side of Eqn. (5.7) includes β_1 and $\mathbf{q}_0$. Since β_1 does not exist in $\mathbf{T}$ it is by definition put equal to zero. Similarly the choice $\mathbf{q}_0 = \mathbf{0}$ is obvious since the first term of Eqn. (5.7) is $\mathbf{q}_{l-1}\beta_l$. From Eqn. (5.7) it is now possible to recursively construct $\mathbf{q}_{l+1}$, α_l and β_{l+1} when knowing $\mathbf{q}_{l-1}$, $\mathbf{q}_l$ and β_l. This is done by applying to Eqn. (5.7) a procedure that recursively generates the Lanczos vectors by iteration for $l = 1, 2, \dots, m$. First Eqn. (5.7) is rewritten as

$$\mathbf{r}_l \equiv \beta_{l+1}\mathbf{q}_{l+1} = \mathbf{H}\mathbf{q}_l - \alpha_l\mathbf{q}_l - \beta_l\mathbf{q}_{l-1} \tag{5.8}$$

The values of α_l is then defined through the hermitian inner product[10]

$$\alpha_l = \langle \mathbf{q}_l^\dagger, \mathbf{H}\mathbf{q}_l \rangle \tag{5.9}$$

Having the value of α_l the values of β_{l+1} are found by the relation

$$\beta_{l+1} = ||\mathbf{r}_l||_{\mathbb{C}} \tag{5.10}$$

[6] Recall that when $\mathbf{T}$ is symmetric one needs only one subindex per entry, for the sub diagonal entries as well as for the diagonal itself. For the sub diagonal symmetry dictates the value of entry ij, when the value of entry ji is known. A diagonal entry is always uniquely given by one subindex. The reason to why $\mathbf{T}$ is symmetric and real we will return to in the following.

[7] It is always possible to transform a hermitian matrix into a real symmetric tridiagonal matrix[7][page 119.].

[8] Using that $\mathbf{Q}\mathbf{Q}^\dagger = \mathbf{Q}^\dagger\mathbf{Q} = \mathbf{1}$

[9] Here the equation will be written for the lth column of $\mathbf{T}$.

[10] In Dirac notation this would be

$$\alpha_l = \langle \mathbf{q}_l | \mathbf{H} | \mathbf{q}_l \rangle$$

It should be noted that if one accidentally chooses $\mathbf{q}_1$ as an eigenvector of $\mathbf{H}$ the $\mathbf{r}_l$ as defined in Eqn. (5.8) takes the value zero[11]. If this happens, another starting vector must be chosen, since $\mathbf{q}_l$ as an eigenvector would bring us no further in the generation of $\mathbf{T}$.
A further note is that the β's must be real since they are the norm of a vector. Since $\mathbf{T}$ is a unitary transform of a hermitian matrix it must itself be hermitian, making it real through the relation $\alpha_i = \alpha_i^\dagger$ and symmetric, due to the relation $\beta_i = \beta_i^\dagger$.
To understand why the expressions for the α_i's and β_i's are consistent with Eqn. (5.5) one has to manipulate Eqn. (5.8), keeping in mind that $\mathbf{q}_i^\dagger \mathbf{q}_j = \delta_{ij}$[12]. It can be proven[8][Lemma 4.9.2] that the complex phase of the β's can be put equal to zero without changing the set of eigenvalues for the Lanczos vectors $\{\mathbf{q}_1, \dots \mathbf{q}_i\}$ and not affecting their rate of convergence. Hence we can justify the choice of removing the 'magnitude of' when taking the norm on both sides of Eqn. (5.8) yielding $|\beta_{l+1}| = ||\mathbf{H}\mathbf{q}_l - \alpha_l \mathbf{q}_l - \beta_l \mathbf{q}_{l-1}||_{\mathbb{C}}$ arriving at Eqn. (5.10).

5.4.2 Convergence

The whole idea of applying the Lanczos algorithm is to obtain a precise estimate for the lowest eigenvalues of $\mathbf{H}$ without diagonalizing it in its full 2^N states basis. If the algorithm is appropriate it should be so, that the lowest eigenvalue of $\mathbf{T}$ converge fast towards the lowest eigenvalue of $\mathbf{H}$, where the convergence is a result of more vectors being added to the basis of $\mathbf{T}$[13].
The expression (5.9) is related to the so called Rayleigh quotient $\rho(\mathbf{x}, \mathbf{A})$ which for a real symmetric matrix[14] $\mathbf{A}$ and general vector $\mathbf{x}$ is defined[8][p. 8] as

Definition 2 (Rayleigh Quotient)**.**

$$\rho(\mathbf{x}, \mathbf{A}) \equiv \frac{\mathbf{x}^T \mathbf{A} \mathbf{x}}{\mathbf{x}^T \mathbf{x}}$$

If $\{\mathbf{x}_1, \dots, \mathbf{x}_n\}$ is an complete set of eigenvectors of $\mathbf{A}$ ordered such that $\{\lambda_i\}_{i=1}^n$ is an increasing sequence, then $\rho(\mathbf{x}, \mathbf{A})$ can be expressed using the complete basis of eigenvectors as

$$\rho(\mathbf{x}, \mathbf{A}) = \frac{\sum_k a_k x_k^\dagger \mathbf{A} \sum_m a_m x_m}{\sum_k a_k x_k^\dagger \sum_m a_m x_m} = \frac{\sum_{k,m} a_k a_m \lambda_m x_k^\dagger x_m}{\sum_{km} a_k a_m x_k^\dagger x_m} = \frac{\sum_k a_k^2 \lambda_k}{\sum_k a_k^2} \tag{5.11}$$

, where the general vector $\mathbf{x}$ has been written as a sum of the complete basis of eigenvectors of $\mathbf{A}$.
From Eqn. (5.11) it follows that

$$\rho(\mathbf{x_k}, \mathbf{A}) = \lambda_k \tag{5.12}$$

$$\lambda_1 \leq \rho(\mathbf{x}, \mathbf{A}) \leq \lambda_n \tag{5.13}$$

[11] If $\mathbf{q}_l$ is an eigenvector for $\mathbf{H}$ then $\mathbf{H}\mathbf{q}_l = \alpha_l \mathbf{q}$

[12] Isolating $\alpha_l \mathbf{q}_l$ from Eqn. (5.8) and letting $\mathbf{q}_l^\dagger$ work from the left gives

$$\alpha_l \mathbf{q}_l^\dagger \mathbf{q}_l = \mathbf{q}_l^\dagger \mathbf{H} \mathbf{q}_l - \beta_l^* \mathbf{q}_l^\dagger \mathbf{q}_{l-1} - \beta_{l+1} \mathbf{q}_l^\dagger \mathbf{q}_{l+1}$$

Using $\mathbf{q}_i^\dagger \mathbf{q}_j = \delta_{ij}$ one obtains $\alpha_l = \mathbf{q}_l^\dagger \mathbf{H} \mathbf{q}_l$.
Further taking the complex norm on each side of Eqn. (5.8) gives

$$||\mathbf{q}_{l+1}\beta_{l+1}||_{\mathbb{C}} = |\beta_{l+1}| \; ||\mathbf{q}_{l+1}||_{\mathbb{C}} = |\beta_{l+1}| = ||\mathbf{H}\mathbf{q}_l - \alpha_l \mathbf{q}_l - \beta_l \mathbf{q}_{l-1}||_{\mathbb{C}}$$

[13] Note that if we just construct 2^N basis vectors for $\mathbf{T}$ the result is just a full-dimensional transformation of $\mathbf{H}$ into tridiagonal form. A situation that would not solve our problem in terms of reducing the amount of RAM and time required for determining the ground state.

[14] If $\mathbf{A}$ is hermitian the hermitian conjugate † should replace the transpose T in the following calculations

I.e. the value of the Rayleigh fraction of a general vector is limited by the two extreme eigenvalues and the Rayleigh quotient of a eigenvector is the corresponding eigenvalue. We are interested in what happens to the Rayleigh quotient of a vector $\mathbf{x}$, if this vector in terms of norm difference is very close to an eigenvector $\mathbf{x}_k$ of $\mathbf{A}$. This is done by evaluating the Rayleigh quotient[15][16] of the vector $\mathbf{x}_k + \delta$, where $\delta = \mathbf{x} - \mathbf{x}_k$

$$\begin{aligned}
\rho(\mathbf{x}_k + \delta) - \rho(\mathbf{x}_k) &= \frac{(\mathbf{x}_k + \delta)^\dagger \mathbf{H}(\mathbf{x}_k + \delta)}{(\mathbf{x}_k + \delta)^\dagger(\mathbf{x}_k + \delta)} - \lambda_k \\
&= \frac{\lambda_k(\mathbf{x}_k^\dagger \mathbf{x}_k) + (\delta + \mathbf{x}_k)^\dagger \mathbf{H}\delta}{\mathbf{x}_k^\dagger \mathbf{x}_k + \delta^\dagger \mathbf{x}_k + \mathbf{x}_k^\dagger \delta + \delta^\dagger \delta} - \frac{\lambda_k(\mathbf{x}_k^\dagger \mathbf{x}_k + \delta^\dagger \mathbf{x}_k + \mathbf{x}_k^\dagger \delta + \delta^\dagger \delta)}{\mathbf{x}_k^\dagger \mathbf{x}_k + \delta^\dagger \mathbf{x}_k + \mathbf{x}_k^\dagger \delta + \delta^\dagger \delta} \\
&= \frac{\delta^\dagger \mathbf{H}\delta + \mathbf{x}_k^\dagger \mathbf{H}\delta - \lambda_k(\mathbf{x}_k^\dagger \delta + \delta^\dagger \delta - \delta^\dagger \mathbf{x}_k)}{\mathbf{x}_k^\dagger \mathbf{x}_k + \delta^\dagger \mathbf{x}_k + \mathbf{x}_k^\dagger \delta + \delta^\dagger \delta} \qquad (5.14)
\end{aligned}$$

Since δ is represented in every term in the numerator it is clear that Eqn. (5.14) tends to zero as δ approaches zero. What has been shown is actually that the Rayleigh fraction is a continuous function. This is fortunate, since it then from Eqns. (5.12), (5.13) and (5.14) follows that

$$\lambda_{\text{lowest},\mathbf{T}} = min(\lim_{\delta \to 0} \rho_{k,\mathbf{T}}(x_k + \delta, \mathbf{T})) = min\Big(\frac{\mathbf{x}_k^\dagger(\mathbf{Q}_k^\dagger \mathbf{H}\mathbf{Q}_k)\mathbf{x}_k}{\mathbf{x}_k^\dagger \mathbf{x}_k}\Big) = min\Big(\frac{(\mathbf{Q}_k\mathbf{x}_k)^\dagger \mathbf{H}(\mathbf{Q}_k\mathbf{x}_k)}{\mathbf{x}_k^\dagger \mathbf{x}_k}\Big) \qquad (5.15)$$

From the last equality sign of Eqn. (5.15) it follows that the minimal Rayleigh fraction of $\mathbf{T}$ which equals the lowest eigenvalue of $\mathbf{T}$, also equals the minimal Rayleigh fraction of the Ritz vector[17] wrt. $\mathbf{H}$, which by Eqn. (5.13) is greater than or equal to the minimal eigenvalue of $\mathbf{H}$, the ground state value. Hence it is shown, that the minimal eigenvalue of $\mathbf{T}$ approaches the minimal eigenvalue of $\mathbf{H}$ if adding more vectors $\mathbf{q}_i$ to the basis of $\mathbf{T}$ makes the lowest eigenvalue $\mathbf{T}$ converge to the lowest eigenvalue of $\mathbf{H}$.
Hence, the final property of the Lanczos algorithm that has to be argued for, before we feel convinced that the lowest eigenvalue for $\mathbf{T}$ converge towards the true ground state value of $\mathbf{H}$, is how the algorithm selects the 'next q-vector'.
The gradient of the Rayleigh fraction is given by [40]

$$\nabla\rho(\mathbf{x}) = \frac{2}{\mathbf{x}^\dagger \mathbf{x}}(\mathbf{H}\mathbf{x} - \rho(\mathbf{x})\mathbf{x}) \qquad (5.16)$$

The 'next q-vector' is the vector that will be added to the basis of the subspace of $\mathcal{H}$ that spans $\mathbf{T}$.
From the Eqn. (5.16)[18] it is seen the properties of the gradient is controlled by the terms $\mathbf{H}\mathbf{x}$ and $\rho(\mathbf{x})\mathbf{x}$. Recalling that $\mathbf{x}$ is any random vector in the space spanned by $\{\mathbf{q}_k\}_{l=1}^{l}$, that is in the span of all the previous generated q-vectors, it can be written as a sum of these. But this means that the term $\mathbf{H}\mathbf{x}$ is the only part of the gradient which is not contained in the span of the previous $\mathbf{q}_i$'s, hence getting the idea that the 'next q-vector' has something to do with $\mathbf{H}\mathbf{x}$. Realizing that this eventually boils down to $\mathbf{H}\mathbf{q}_1$ we write $\mathbf{x}$ as a sum of $\mathbf{H}$ working on

[15] This method is taken from the program report by Frederik [40].

[16] From now on it is implicitly assumed that the matrix in the expression for $\rho(\mathbf{x}, \mathbf{A})$ is the Hamiltonian $\mathbf{H}$ and it will hence not be stated explicitly and the notation will just become $\rho(\mathbf{x})$.

[17] If $(\mu, \mathbf{u})$ is an eigenvalue-eigenvector pair of a tridiagonal matrix $\mathbf{T}_l$, l being the column dimension, obtained by Lanczos algorithm from the hermitian matrix $\mathbf{H}$, then the vector defined by $\mathbf{y} \equiv \mathbf{Q}_l\mathbf{u}$ is called the Ritz vector of the matrix $\mathbf{H}$ and μ the Ritz value [8, Sec.0.5].

[18] Which I havn´t been able to show and therefore is taken from a report by F. Treue [40] without proof.

the previous q-vectors

$$\mathbf{x} = \alpha \mathbf{H}^{l-1}\mathbf{q}_1 + \beta\big(\sum_{n=0}^{l-2} a_n \mathbf{H}^n \mathbf{q}_1\big)$$

, where $\mathbf{H}^{l-1}\mathbf{q}_1 = \mathbf{q}_l$. Letting $\mathbf{H}$ work on this we arrive at

$$\mathbf{Hx} = \alpha \mathbf{H}^{l}\mathbf{q}_1 + \beta\big(\sum_{n=1}^{l-1} a_{n-1} \mathbf{H}^n \mathbf{q}_1\big)$$

We see that the nature of $\mathbf{Hx}$ in terms of finding the 'next q-vector' is $\mathbf{H}^l\mathbf{q}_1 = \mathbf{q}_{l+1}$, as the remaining terms already belong to the span of the previous q-vectors - which are the terms including the basis vectors $\{\mathbf{H}^n\mathbf{q}_1\}_{n=0}^{l-1} = \{\mathbf{q}_n\}_{n=1}^{l}$ already spanning the subspace. Returning to Eqn. (5.8) ensures us that the choice of the 'next q-vector' that Lanczos algorithm uses, exactly has the necessary form in order to add what is missing to the subspace, so as to make $\rho(\mathbf{x})$ change in the 'direction' where its gradient is maximized. Hence the selection of 'next q-vector' that the Lanczos algorithm uses, ensures that the lowest eigenvalue of $\mathbf{T}$ in the subspace spanned by $\{\mathbf{q}_k\}_{l=1}^{l}$ converge as fast as possible towards the ground state of $\mathbf{H}$ when $\mathbf{q}_{l+1}$ as given by Eqn. (5.8) is added to the previous basis.

5.4.3 Convergence in RLexact

This subsection will offer a brief explanation of the way RLexact decides if the Lanczos algorithm has converged. In this connection the notion of a Ritz vector is crucial. A Ritz vector is a vector in the basis (see Eqn. (5.6) and the surrounding text) for the tridiagonal matrix $\mathbf{T}$ that the Lanczos algorithm creates iteratively. After each iteration RLexact investigates the last entrance in the eigenvector of the lowest eigenvalue. This entrance is the amplitude of the latest generated basis vector in the ground state. When this amplitude gets very small it means that the last iteration have not made the vector approach the true eigenvector considerably. In RLexact 'small' is defined by the constant RITZ_CONV, such that the algorithm stops when the above mentioned amplitude gets smaller than RITZ_CONV. Since the way the basis vectors are created iteratively ensures that the convergence is as optimal as possible, see previous sub section, we can be sure, that the true lowest eigenvalue and belonging eigenvector are found when RLexact aborts the Lanczos algorithm.
All calculation except a few, were done with RITZ_CONV = 10^{-9}. When other values are used, this will be mentioned explicitly.

5.5 The parallelization

The parallelization of RLexact from its original version was mainly done by Frederik Treue, while the final part was done by the author.
This section is devoted to a brief description of how the parallelization of RLexact works.
RLexact is run on a cluster at Danish Center for Scientific Computing (DCSC). When using DCSC the process is controlled by scripts, written in the programming language of Perl. The parallelization is divided into four steps named step0.pl, step1.pl, step2.pl and step3.pl. These

four steps[19] take a varying number[20] of arguments and are run from a console at your DCSC account. The Perl-scripts create a number of shell-scripts which are feeded to a 'distant' console of DCSC. The task of the shell-scripts, is to control the file copying, file reading etc. between the various parallelized parts of RLexact.

5.5.1 The four steps of the parallelized RLexact

For this entire subsection the 4x2 lattice will be use as an example. The brackets [...] is included for graphical ease and should not be typed into the console.

step0.pl

step0.pl takes either three or four arguments - three if no m-symmetry is present and four if m-symmetry is present[21]. When running this step one should in the console enter the following:
Without m-symmetry: ./step0.pl [#spins in x-direction] [#spins in y-direction] [0]
With m-symmetry: ./step0.pl [#spins in x-direction] [#spins in y-direction] [1] [m-value]

Quite logically the third argument which can be either 0 or 1 contains the information of whether m-symmetry is present, if so the fourth argument tells for what m-value the calculations by RLexact should be carried out.
The product of step0.pl depends again on the presence of m-symmetry, but in both cases the output is file(s) that is(are) essential for step1.pl and step2.pl.
If the calculations are done for a 4x2 system, entering ./step0.pl 4 2 0 would generate the files named 4x2.un and 4x2.uno respectively.
If m-symmetry is present the .uno file is not generated since it contains information about the magnetization which is known, since it is the invariant m-value which we have feeded to RLexact. For the 4x2 lattice in the $m = 3$ subspace entering ./step0.pl 4 2 1 3 would generate the output 4x2-3.un.
The name of the file indicates its content; the .un files contain the necessary uniques and the .uno files contain the observables corresponding to the uniques - in this case the magnetization.

step1.pl

step1.pl generates two types of files; .dat and .gs. The .gs files are binary files which is to be used in step2.pl, hence not containing any directly extractable results. The .dat files are somewhat more interesting, since they contain a list of the energies of the different states of the system. Since this energy depends on the point in q-space, RLexact generates one .dat file for every point in k-space. Hence, once again using the 4x2 system as an example, 8 files will be generated for the q-points $(0,0)$ to $(3,1)$.
What should be entered in the console to run step1.pl is simply

[19] Actually there exist three more steps: step0_32.pl, step1_32.pl and step2_32.pl. These are used instead of the normal steps, when one is interested in running a sample $\sqrt{N} \times \sqrt{N}$ lattice. The _32 steps works by selecting every second spin and every second **q**-vector. The name is due to the $\sqrt{32} \times \sqrt{32}$ lattice that is run by the _32 steps on a 8×8 lattice. We shall in the proceeding text only mention step1.pl to step3.pl, since the _32 steps are similar with respect to the output.

[20] This feature is made by the author, in order to be able to find ground state energies of systems with m-symmetry but with varying m-values. The m-value is defined simply as $m = \frac{1}{2}(N_\uparrow - N_\downarrow)$.

[21] The information of whether m-symmetry is present is given manually by either activating or deactivating line 25 of RLexact.h

./step1.pl 4 2, since the information of m-symmetry (and m-value) is carried over to step1 from step0 by the .un unique files.

step2.pl

step2.pl generates only one type of files but one file for every point in q-space. The files are named .szz and contain three informations: The length of the vectors $S^{zz}(q,\omega)|\text{gs}>$, the value of ω and finally the value of $S^{zz}(q,\omega)$. ω is the energy from step1.pl in units of $\hbar$.
To run step2.pl from the console one has to type ./step2.pl 4 2 0 or ./step2.pl 4 2 1
, depending on the presence of m-symmetry.

step3.pl

step3.pl does not do any new calculations, it merely collects the results of the previous steps in one file for each q-point. To run step3.pl from the console one has to type ./step3.pl 4 2
, also here using 4x2 as example.

The input-file

The information about the physical system enters RLexact through an input-file, read by the .pl scripts. This input file contains information about the number of sites, the type of coupling etc. It must be written manually and contain exactly the right number of parameters having certain names.
Regarding the type of coupling, the information about a Heisenberg square lattice with nearest neighbor coupling is contained in this input-file.

5.6 Three programming tasks

When I started my project RLexact it was not working. The reason was, that a previous attempt to parallelize the program so as to lower the calculation time on the cluster, had been left partly unfinished. By the competent guidance of Frederik Treue, we succeeded after some time in running the program, but only with no m-symmetry. At this point three task lay ahead.
The first task was to change the C-code in RLexact enabling it to calculate the magnetization of the ground state, when no m-symmetry is present. This will be treated in Sec. 5.7.
The second task was to change the Perl scripts, so that RLexact could run step0, step1 and step2 *with m-symmetry and for any m-value (any given m invariant subspace)*, since up to this point the parallelized program had only been capable of working in the subspace of $m = 0$.
This programming task took some time, but will not be discussed further in this thesis. Should future users of RLexact be interested in discussing the changes, they are welcome to contact me.
Finally the third task was to optimize the part of RLexact itself, that relates the bit pattern representing a state of the sample, with the unique representing the given state. The hope was that this would enable RLexact to run a 36 spin lattice within the two days time limit at DCSC. This task was quite difficult and was done by Frederik Treue with the author as apprentice. At the time of writing, this task was not completed.

5.7 The magnetization of the ground state when no m-symmetry is present.

This section treats the first programming task done by the author[22] on RLexact. The background was actually a misunderstanding, since the theme of physical interest from the perspective of the CFTD results made by N. B. Christensen *et al.*, was the magnetization curve treated in Sec. 4.2. At first I did not understand this, and instead developed the program code, such that it can calculate the magnetization when no m-symmetry is present[23]. However I will in the following subsection present the work, in order to document what RLexact is capable of for future use.

5.7.1 Magnetization of the ground state

We start by a few physical considerations. The magnetization operator is denoted $\hat{M}_0$, since the quantum mechanical expectation value of the ground state magnetization given by $\langle gs|\hat{M}_0|gs\rangle$. The initial block diagonalization of the original Hamiltonian of dimension 2^N for a N-spin system is carried out by the uniques $|u\rangle$. From the theory of the Lanczos algorithm, it follows that the ground state vector of the system represented by the tridiagonal matrix converges to the true ground state, as more vectors are added to this subspace. From these two observations it must follow that the ground state can be written as a linear combination of the uniques, since these constitute the basis of the Lanczos vectors, that is $|gs\rangle = \sum_u a_u|u\rangle$. The magnetization operator simply counts the number of spin-ups and spin-downs and hence the uniques are eigenstates of this operator, i.e. $\hat{M}_0|u\rangle = m_u|u\rangle$. Having all this in mind it follows that

$$\begin{aligned} M_{|gs\rangle} &= \langle gs|\hat{M}_0|gs\rangle = \sum_{u,u'} a_u a^*_{u'}\langle u'|\hat{M}_0|u\rangle \\ &= \sum_{u,u'} a_u a^*_{u'}\langle u'|m_u|u\rangle = \sum_{u,u'} a_u a^*_{u'} m_u\langle u'|u\rangle \\ &= \sum_u a_u a^*_u m_u = \sum_u |a_u|^2 m_u \end{aligned} \tag{5.17}$$

This calculation were easily converted into C code, since the $|u\rangle$'s and the a_u's already were stored by RLexact.

5.8 Optimizing RLexact

The optimization of RLexact was done on the function FindUnique. What this function do, is to find the Unique corresponding to to a given bit pattern obtained after $\hat{H}^{\pm}$ has worked. This is in the present version of RLexact done by a linear search through a table of Uniques, which per lookup will cost $\mathcal{O}(N)$ in calculation time, since the number of uniques are exponential[24] in N. The idea in the optimization is to replace the linear search with a number of clever translations. These translations are x- and y translations and are chosen such that they minimize the number of translations needed to identify the bit pattern with the lowest

[22] heavily guided by Frederik Treue

[23] When m-symmetry is present, the magnetization of a given state is trivial, since the magnetization of the random starting vector in the Lanczos algorithm is invariant. That is, the basis vectors $\mathbf{q}_i$ will remain in the m subspace to which $\mathbf{q}_1$ belongs.

[24] Discussion with Frederik Treue.

corresponding binary number, starting with 2^0 in the upper left corner of a square bitmap with N sites. The optimization was unfortunately not completely finished, at the time of handing in the thesis. However, only a little debugging is missing. It is hard to say precisely how much this optimization will save in calculation time when implemented, but a guess is a factor of 10 every time FindUnique is called. The total time-saving then, depends on how much time FindUnique consumes out of the total time consumption of RLexact. I do not have an estimate for this.

5.9 RLexact and $S^{zz}(\mathbf{q},\omega)$

For the purpose of exact diagonalization which on the bottom line is linear algebra, $S^{zz}(\mathbf{q},\omega)$ can be expressed through the Lehmann representation

$$S^{zz}(\mathbf{q},\omega) = \sum_e M_e^{zz}(\mathbf{q},\omega)\delta(\omega + E_0 - E_e) \tag{5.18}$$

where

$$M_e^{zz}(\mathbf{q},\omega) = 2\pi|\langle e|s_q^z|\mathrm{gs}\rangle|^2 \tag{5.19}$$

This is nothing but an inner product ready to calculate.
In Eqn. (5.19), $|\mathrm{gs}\rangle$ is the ground state and $|e\rangle$ is any of the exited energy eigenstates. The operator s_q^z is the Fourier transform of the spin-z operator s_n^z and is defined by

$$s_q^z = \frac{1}{\sqrt{N}}\sum_{n=1}^{N} e^{iqn}s_n^z \tag{5.20}$$

In zero field which corresponds to the ground state of the $m = 0$ subspace, $S^{zz}(\mathbf{q},\omega)$ fulfills the sum rule [34, Eqn.(15)]

$$\int_{-\infty}^{\infty} d\omega \sum_{\mathbf{q}}\sum S^{\alpha\alpha}(\mathbf{q},\omega) = \sum_{e,\mathbf{q}} M_e^{\alpha\alpha}(\mathbf{q},\omega) = \frac{N\pi}{2} \tag{5.21}$$

Selected output $S^{zz}(\mathbf{q},\omega)$ output from RLexact were tested by the sum rule Eqn. (5.21).

5.9.1 Calculations by hand

$S^{zz}(\mathbf{q},\omega)$ was for the purpose of testing the reliability of RLexact, calculated by hand for a few simple systems - 2x1 and 4x1. These calculations found in the Appendix, Sec. A.1 and were found to agree with the results of RLexact to within the accuracy of RLexact.

Chapter 6

Results

This chapter will present the results of this thesis work. The uniform magnetization, the susceptibility and the staggered moment are in the given order the first topics. After this follows a presentation of the energy dispersion, and finally, results for the dynamical structure factor will be stated. Each section contains in the end a discussion of the results.

6.1 Magnetization and susceptibility

The data output from step1 of RLexact is the the energy of the state of the square lattice under investigation. This energy is calculated upon an assumption of zero h-field, since the last term of Eqn. (2.1) the Zeeman term is vanishing. Nevertheless it is at this point possible to calculate how the energy for the different states of the square lattice would evolve if an h-field is turned on. This is simply done by considering the effect of adding the Zeeman term $\hat{H}_{\text{Zeeman}} = h \cdot \sum_i^N S_i^z$ once again. This is readily done, since the resulting function $E(h) = E_0(m) + h \cdot \sum_i^N S_i$ is nothing but a straight line with the slope equal to the m-value of the system and the second axis intersection being the lowest lying energy $E_0(m)$ of the corresponding m-value. It is then possible to make a multiple straight-lines plot, each line having as starting point $E_0(m)$ and a slope equal to the corresponding m-value. These curves contain interesting information, since the state of lowest energy for any value of h can be identified from inspection of the curves. This type of plot is seen in the left panel of Fig. 6.1.

The magnetization[1] is given by $m(h) = -\frac{\partial E_0(h)}{\partial h}$, where $E_0(h)$ at every value of h is determined from the curve corresponding to the lowest energy of Fig. 6.1.

$$E(h) = E_0(m) + h \cdot \sum_i^N S_i$$

As is seen from Fig. 6.1, many energies are related to a given value of h. However, a given system will naturally choose the state which minimizes the energy. Hence one can obtain a curve for the magnetization by displaying the slope of the lowest lying Zeeman energy branch for a given h-interval, going from[2] $m = -\frac{N}{2}$ to $m = \frac{N}{2}$. This magnetization curve is a multi-step function. The result of this procedure for the 4x2 lattice is seen in the right panel of Fig. 6.1. Note that the step length decrease for increasing h.
By plotting every value of m with the numerically smallest value of the corresponding h-field[3]

[1] See Sec. 2.2 Eqn. (2.9)
[2] The negative values follow from symmetry.
[3] We shall argue for this procedure in the discussion of the results.

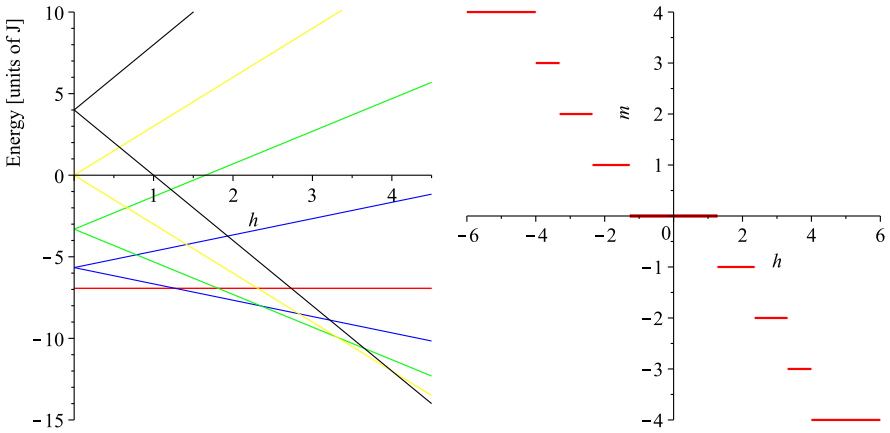

Figure 6.1: Left: The energy $E(h)$ in units of J for the 4x2 lattice (a small lattice is chosen for visual simplicity). The intersection with the second-axis is the lowest lying energy level of the Hamiltonian (2.1) for the m-value corresponding to the slope of the line. The slopes of the lines take the integral value from 0 to 4, with the red line corresponding to $m = 0$ and the black line corresponding to $m = 4$. Right: The magnetization step function $m(h)$ for the 4x2 lattice (a small lattice is chosen for visual simplicity) obtained from the procedure described in the text.

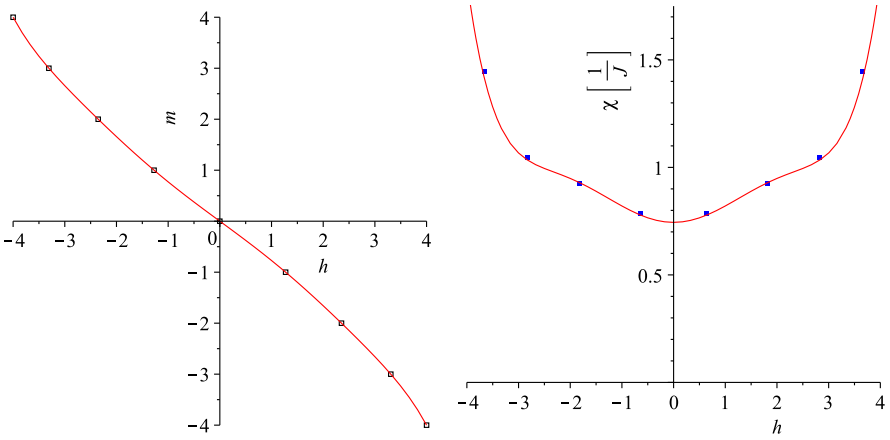

Figure 6.2: Left: The magnetization curve extrapolated to the thermodynamic limit. The unit of m is $g\mu_B$. Right: The magnetic susceptibility $\chi = \frac{\partial m}{\partial h}$. The red line is obtained from differentiation of the polynomial fit to the data points in the right panel of Fig. 6.2. The blue points are found by a method based on the mean value theorem described in the text.

a number of discrete points are obtained and if subjected to a polynomial fit a continuous curve for the magnetization is reached. The result of this for the 4x2 lattice is seen in the left panel of Fig. 6.2. The yield of the polynomial fit is a function that by differentiation gives the magnetic susceptibility $\chi = \frac{\partial m}{\partial h}$, exemplified in the right panel of Fig. 6.2 for the 4x2 lattice. In order to verify the results for χ a number of points are calculated by means of the mean value theorem. Specifically this is done by plotting the slope of the line between two points in the left panel of Fig. 6.2 (which by the mean value theorem is the average slope of the curve between these two points) vs. the midpoint of the corresponding h-interval. The points obtained from this are the blue squares in the right panel of Fig. 6.2. Hence, dealing with the

susceptibility in this thesis one should remember that it is not a direct product of RLexact's numerical results. The results are therefore to be interpreted with a certain scepticism.

RLexact was run for the systems; 10x1, 4x2, 4x4, $\sqrt{32}$x$\sqrt{32}$ and 6x6 and the above procedures for the energy, magnetization and susceptibility were carried out. The results, except for the 6x6 lattice, are presented in Fig. 6.3. The first column displays the energy, the second- and third column present the magnetization and the fourth column displays the susceptibility.

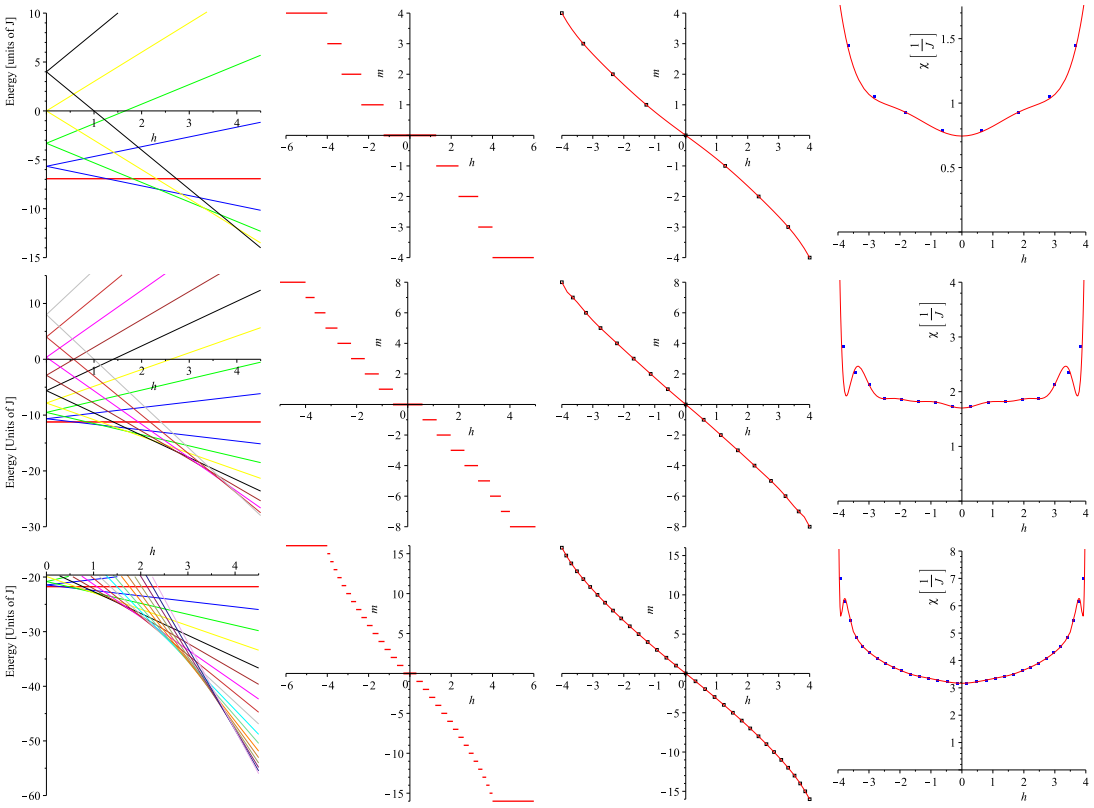

Figure 6.3: Results from step1 of RLexact. The rows represents from top to bottom the lattices: 4x2 (rectangular), 4x4 (quadratic) and $\sqrt{32}$x$\sqrt{32}$ (quadratic). First column shows the energy E as a function of magnetic field h. E is in units of J. Second column shows a step curve for the magnetization. Third column displays the magnetization in the thermodynamical limit; a polynomial fit to the numerically smallest value of m as given in column two, for any value of h. Finally the fourth column shows the magnetic susceptibility. Here the solid line is obtained from differentiation of the polynomial fits of column three, and the points are reached by plotting the average slope between two points on the thermodynamical magnetization vs. the interval midpoint, as described in the text.

6.1.1 Discussion of magnetization

For all the systems calculated by RLexact, it is seen that the m-value of the energetically lowest lying curve starts at $m = 0$ for $h = 0$ and then increases (decreases) in integral values up to $m = +(-)\frac{N}{2}$, when $h = 8SJ = 4$, in units of J. Why this occurs at the same value for h in all systems, can be understood from the ferromagnetic spin wave dispersion Eqn. (2.62)

evaluated in the point (π,π), such that $\hbar\omega = 2\frac{1}{2}(J(0) - J(\pi,\pi)) + g\mu_b h = 4J + g\mu_b h$. When $g\mu_B = 1$ then $\hbar\omega \geq 0$ only if $h \geq 4J$. To be the ferromagnetic ground state we must have that $\hbar\omega = 0$. Hence $h = \pm 4J$ is the limit

When examining column one and two of Fig. 6.3 a tendency stands out: It is seen, that the interval of h in which m has a fixed value decreases by two mechanisms: i) the higher the value of h the shorter m-stable h-interval and ii) the more spins in the system, the shorter m-stable h-interval. The second observation is trivial but the first is interesting, since the classical magnetzation curve is a straight line. Hence, remark i) is a quantum effect.
At this point it is natural to argue for the method used to obtain these points based on ED of finite systems. Lets name the method 'interpolation by fixed endpoint' for reference. A name that shortly will make sense. As mentioned, these points are obtained by plotting each m-value with the numerically lowest of its corresponding h-values. Hence, interpolation by fixed endpoint relies upon the assumption that the numerically lowest endpoint of the intervals (the left(right) endpoint for positive(negative) h) is fixed, making the interval shrink from the right(left) when going to the thermodynamic limit. A way to test the reliability of the method, is to plot all the magnetization curves obtained on this background in the same figure and investigate whether the set of points belonging to the same m-value coincide. This is done in left panel of Fig. 6.4[4], where new results for the 6x6 lattice are presented as well[5]. But, before consulting the figure a remark is needed: If interpolation by fixed endpoint is correct and finite size effects did not exist, then every set of (h, m_{fixed}) would coincide, in effect making the simulation of large systems superfluous. Now, we turn to left panel of Fig. 6.4. Here it is seen that the above mentioned points in each set do not coincide (the blue points corresponding to an AFM chain should be neglected at present). This can be due to two reasons; finite size effects and/or drawbacks in the method of interpolation by fixed endpoint. Finite size effects are present as is seen in the right panel of Fig. 6.4. This we will return to.
I have not been able to come up with a rigorous argument to justify interpolation by fixed endpoint, but from a physical point of view it seems natural to plot the m-value with the lowest corresponding h, since it is at this field that m increases one step[6].
Fortunately it is from Fig. 6.4 clear, that the points corresponding to the 32 and 36 spin lattices behave very similarly, convincing us that these two results are trustable and have already converged.

Continuing to the third column of Fig. 6.3, it is from all samples clear, that the $m(h)$ curve is slightly 'S-shaped'. This feature is a quantum effect which does not exist for classical systems. In order to visualize this effect the points in third column of Fig. 6.3 are weighted with the number N of sites in the sample and plotted in the the same figure. This is left panel of Fig. 6.4, where also the classical curve and a plot of a 10 spin AFM chain is found. The tendency is clear: The pronounced 'S-shape' for the 1D chains is straightened out in the 2D case, approaching but not equaling the straight classical curve[7] $m(h) = \frac{h}{8}$. Hence, the S-shape is a genuine quantum effect.
With respect to these magnetization curves a few features need a comment: Examining the region around the origin (from symmetry we can restrict our attention to the second quadrant),

[4]This is not the main purpose of the figure. The main purpose of the figure will be presented in a while.

[5]The results for the 6x6 lattice have not been presented seperately, since points corresponding to $m \leq 5$ have not been possible to obtain. The remaining points for $m \geq 6$ are all found in Fig. 6.4.

[6]I have not been able to find any paper in details describing their method of interpolating $m(h)$, but I have in agreement with K. Lefmann used interpolation by fixed endpoint.

[7]See Eqn. (2.7), Sec. 2.2

there seems to be a tendency in each sample, that a line through the three numerically smallest points belonging to the lowest value of h will approach a nonzero m. This is a finite size effect, the nature of which is revealed by plotting the m-axis intersection of a straight line through these three numerically smallest points vs. $1/N^3$, where N as usual is the sample size. This is done in the right panel of Fig. 6.4, from which it is seen, that the effect scales as approximately $1/N^3$.

Further one notes that all functions are clearly antisymmetric, i.e. $m(-h) = -m(h)$. This is to be expected from the symmetry of the Heisenberg Hamiltonian Eqn. (2.1) governing the 2DQHAFSL. When differentiating wrt. h, see Eqn. (2.9), the only term having a influence on $m(h)$ is $g\mu_b h \sum_i S_i^z$, which clearly will yield an anti-symmetric function in h after differentiation, since $h \to -h$ reverses the slope of the line. Also from a physical point of view it is natural to expect $m(h)$ to be an odd function, since reversing the field must reverse the magnetization.

As a final remark, the comparison with the literature will not be done for the uniform magnetization separately, since it qualitatively is very hard to note any possible differences between Fig. 6.4 and the inset of Fig. 4.2. However, should there be any differences these will be revealed in the coming discussion of χ, which being related to the $m(h)$ through differentiation is perfect for revealing differences.

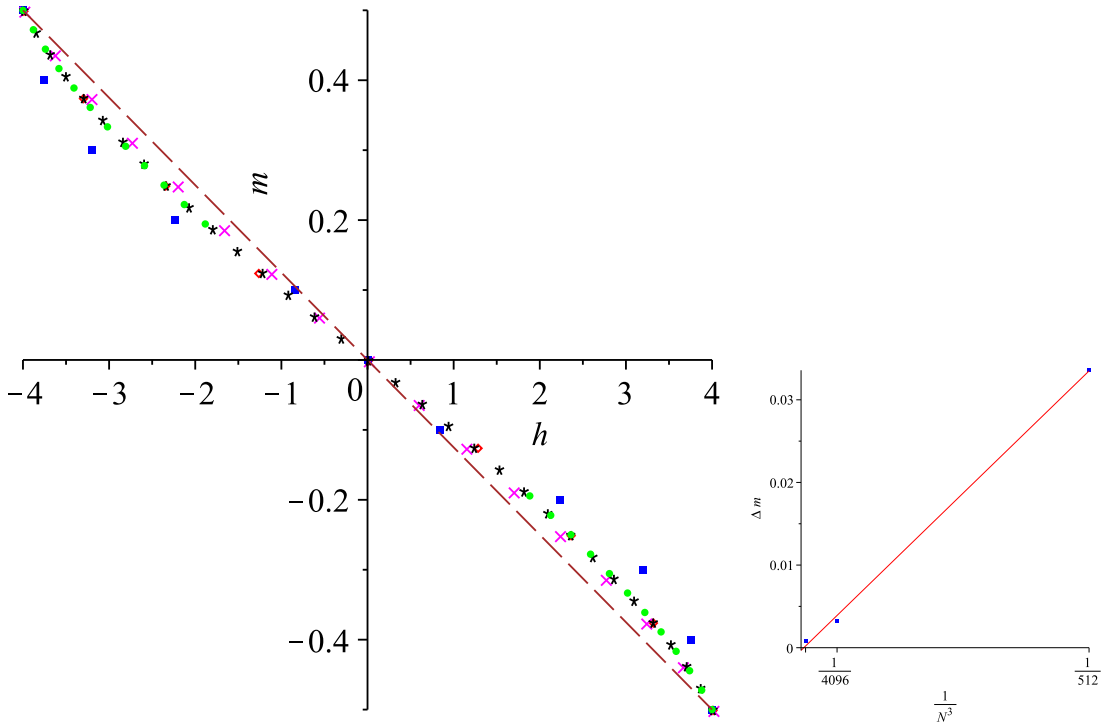

Figure 6.4: Left: Magnetization curves for the the 2DQHAFSL. The data points are from clusters of 2x4 (red diamond), 4x4 (pink diagonal crosses), $\sqrt{32}$x$\sqrt{32}$ (black stars), 10x1 (blue solid squares) and 6x6 (solid green circles). These points are constructed by plotting the numerically smallest h-value of each m-stable h-interval vs. the corresponding m-value. The dashed line is the classical result having the constant slope 1/8. Right: The 'linear slope gap', revealing that the abscissa intersection of the straight line through the three numerically smallest h-values on each of the magnetization curves goes to zero approximately as $1/N^3$, where N is the number of sites in the sample.

6.1.2 Discussion of the susceptibility

The susceptibilities for all samples in the fourth column of Fig. 6.3 can like the magnetizations be displayed in a common plot, and this is done in Fig. 6.5. Examining this figure it is seen that the abscissa intersections are different between the various samples. In table 6.1 these intersections are displayed and by inspection it is seen, that the intersections of the 2D samples are not decreasing nor increasing monotonically as a function of N. A reason could be a finite size effect due to the fact that the 4x2 sample is different from the 4x4 and the $\sqrt{32}$x$\sqrt{32}$, since the latter two are quadratic while the 4x2 is rectangular. The classical value

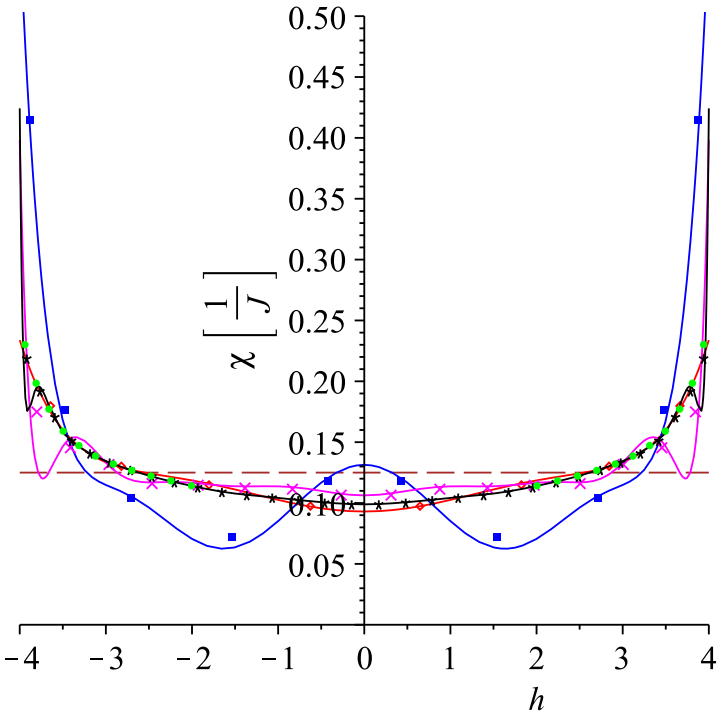

Figure 6.5: The susceptibility for the the 2DQHAFSL. The data points are from clusters of 2x4 (red diamond), 4x4 (pink diagonal crosses), $\sqrt{32}$x$\sqrt{32}$ (black stars), 10x1 (blue solid squares) and 6x6 (green solid circles). These points are constructed by at each midpoint of the m-stable h-interval, plotting the slope of a straight line connecting neighboring points on the corresponding magnetization curve, Fig. 6.4. The solid lines (same color coding) originate from numerical differentiation of a polynomial fit to the magnetization points. Note that no line exists for the 6x6 data. This is because the lack of points around $m = 0$ makes numerical differentiation impossible. The dashed brown line is the classical result, taking the constant value 1/8. See the text for a comment about the chain.

is $\chi = 1/8 = 0.125$ and once again we see that the AFM chain displays more pronounced quantum behavior than the square lattices. The $\sqrt{32}$x$\sqrt{32}$ lattice has at zero field $\chi \approx 0.099$ while the 4x4 lattice has $\chi \approx 0.108$. At $h \approx 2.5$ all 2D curves, which for $h \lessapprox 2.5$ lay lower than the classical line, cross this line and stay above for $h \gtrapprox 2.5$. That the crossing happens at $h \approx 2.5$ is consistent with the results of Lüscher and Läuchli [39]. The same is the feature, that the deviation between ED results and the classical line is maximal as saturation is reached. One also notes the consistency of the points representing the 32 and the 36 spin lattice.
A feature that is revealed by this work, is the general tendency that the higher the field the

system	m- axis intersection
1x10	0.1314
4x2	0.0930
4x4	0.1063
$\sqrt{32}$x$\sqrt{32}$	0.0989

Table 6.1: The abscissa intersection of the magnetic susceptibility obtained from the numerically differentiated polynomial fits to the magnetization curves of Fig. 6.4.

better agreement between the various finite square lattices. This information is not extractable from [39], since only one ED points for one lattice are displayed, see Fig. 4.3.
The sudden dip that the 4x4 curve of Fig. 6.5 displays at $h \approx \pm 3.75$, is probably an effect of numerical differentiation. But, the outermost diagonal cross on this curve indicates a deviation from the 4x2 and $\sqrt{32}$x$\sqrt{32}$ lattices. This is unexpected, since from a physical point of view, the 4x4 is more like the $\sqrt{32}$x$\sqrt{32}$ than the 4x2 system. Hence, it would be interesting to run more finite systems in order to investigate this pathologic behavior. Also the literature presents no sign of this anomaly, see Fig. 4.3, which is based on results from three papers.
Note also the asymmetry of the curve about the midpoint of the h interval and the classical value 0.125, as already discussed in Sec. 4.2.
Finally, the curve for the 10 spin chain needs a comment. As is noted its shape with the 'bump' at zero field is different from the rest. This is not to be expected, since the spin chains though displaying more pronounced quantum effect should not behave topologically different[8]. Furthermore such a bump is unphysical, since there should be nothing special about the interval $|h| \leq 1.5$. Hence, what we see for the 10 spin chain is probably a finite size effect. However, since the topic of this thesis work is the 2DQHAFSL, we shall not follow this any further.

6.2 The staggered magnetization - results and discussion

When presenting data for the staggered magnetization, it is important to state exactly what is presented. In table 6.2, the results from RLexact for $S(\pi, \pi)$ is shown in the second column. Note that there is no ω dependence, indicating that only the result for the strongest pole of $S((\pi, \pi), \omega)$ are presented. One could have chosen to sum up the contributions from all ω per $\mathbf{q}$ and present this result. This is however not chosen here, since it is the strongest pole that normally is measured in neutron scattering experiments, when the staggered magnetization is investigated. When reading the table 6.2, recall Eqn. (2.76) giving that $m^{\dagger} = \langle S \rangle = \sqrt{\frac{S((\pi,\pi))}{2\pi N}}$.

System Lx$L = N$	$S((\pi, \pi))$	$\sqrt{S((\pi, \pi))/2\pi N}$
4x2	5.191	0.321
4x4	9.145	0.302
$\sqrt{32}$x$\sqrt{32}$	14.376	0.267.

Table 6.2: Results for the staggered magnetization found on the background of ED.

As discussed in Sec. 2.6 one should be careful when interpolating the staggered magnetization, found from finite clusters, to the thermodynamical limit. And, we shall use an $1/\sqrt{N}$ interpolation as an alternative. We shall use a $1/N$ interpolation, knowing that it theoretically is

[8] Discussion with K. Lefmann.

shown to overestimate the value of $m^\dagger$ in the thermodynamical limit. A least squares interpolation of $\sqrt{S((\pi,\pi))/2\pi N}$ vs. $1/N$ ($1/\sqrt{N}$) is seen in the left (right) panel of Fig. 6.6. Since the abscissa through Eqn. (2.76) is the staggered moment, we have from the $1/N$ interpolation ($1/\sqrt{N}$ interpolation) determined the value $m^\dagger = 0.285$ ($m^\dagger = 0.219$) which is $\approx 52\%$ ($\approx 44\%$) of the classical value $m^\dagger_{cl} = 0.5$. Table 6.3 presents a comparison of the result for the staggered magnetization of this thesis work with the literature[9]. The uncertainty on the results of this

Reference	[32]	[15]	[16]	This work
$m^\dagger$	0.30(2)	$\simeq 0.313$ & $\simeq 0.321$	0.42(1)	0.258(*)&0.219(*)

Table 6.3: Results for the staggered magnetization $m^\dagger$. The two results by [15] is due to series expansion and SWT respectively. The SWT calculation was done to first non-linear order. Note also that no uncertainty is stated in [15]. This is for the series result due to the value being obtained from series expansion evaluated in three different ways and with almost equal results. In the case of SWT I cannot explain the lack of uncertainty. The results of this work is explained in the text.

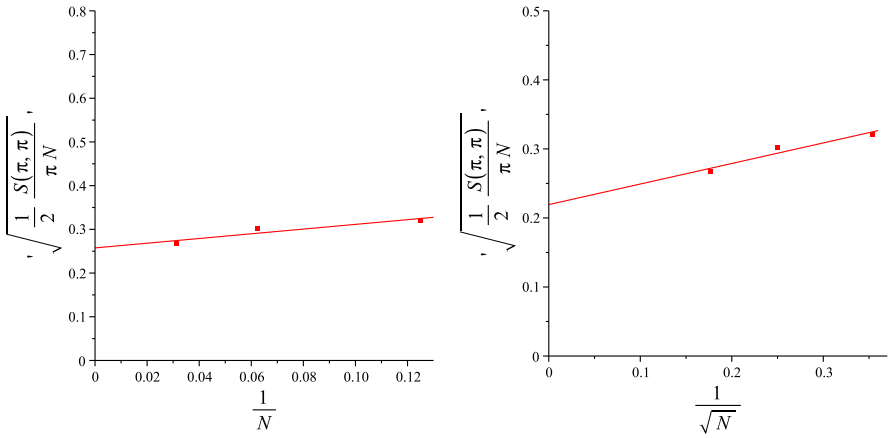

Figure 6.6: Left (right), a plot of $\sqrt{S((\pi,\pi))/2\pi N}$ vs. $1/N$ ($1/\sqrt{N}$). A linear fit using the method of least squares yields the abscissa intersection $m^\dagger = 0.258(*)$ ($m^\dagger = 0.219(*)$). For an explanation of the uncertainties, see the text.

work is difficult to estimate. The results from RLexact are as exact as possible, since they rely on exact diagonalization. On the other hand, when performing the least squares fit there is a rounding error in the values entering the fit. This error can be made negligible by using all decimals calculated. However, the least squares fit introduces an uncertainty expressed by a standard deviation. These deviations are found to be $\sigma_{m^\dagger} = 0.07$ and $\sigma_{m^\dagger} = 0.12$ for the $1/N$ and $1/\sqrt{N}$ interpolations respectively. The calculations can be found in Appendix D.1.
Using these uncertainties which are really big, the results of RLexact are consistent with the leterature, e.g. the value of $m^\dagger = 0.30(2)$ by [32] based on QMC. It should be noted, that this conclusion is not very strong, since a result with such a relatively big uncertainty is consistent with many results. Hence, despite this potential consistency it seems, by looking at the RLexact data, reasonable to conclude that $m^\dagger$ is underestimated wrt. e.g. [32]. This is the opposite tendency as described by [15], which stated that a $1/N$ interpolation would overestimate $m^\dagger$.

[9] I have not been able to access the original work of Oitmaa and Betts and hence their result is due to reference from A. D. Huse [15].

On the other hand, we have earlier in this thesis seen, that the smaller the system, the more pronounced quantum effects. Since the deviation from the classical value of $m_{cl}^{\dagger} = \frac{1}{2}$ are a quantum effect, a possible explanation to the underestimation is that the interpolation points come from relatively small finite clusters.
As a final note, the result from RLexact based on a $1/\sqrt{N}$ interpolation is possibly wrong. The reason is that the 2x4 lattice is rectangular instead of quadratic, hence making the incorrect assumption that $1/\sqrt{N} = 1/L$ in the interpolation of the Lx$L = N$ lattice. As a general comment, the number of points (three) in the interpolation is too low to really trust the results. Furthermor, it is not clear to me whether the $1/N$ and/or $1/\sqrt{N}$ interpolations are correct from a mathematical point of view.

6.3 The energy dispersion - results and discussion

In order to compare the experimental results for CFTD by N.B. Christensen *et al.* [23] with the numerical work of this thesis, a plot of the energy dispersion is indispensable, and such a plot is seen in Fig. 6.7. The two LSW dispersions are based on Eqn. (2.40) and (2.61) for nearest and

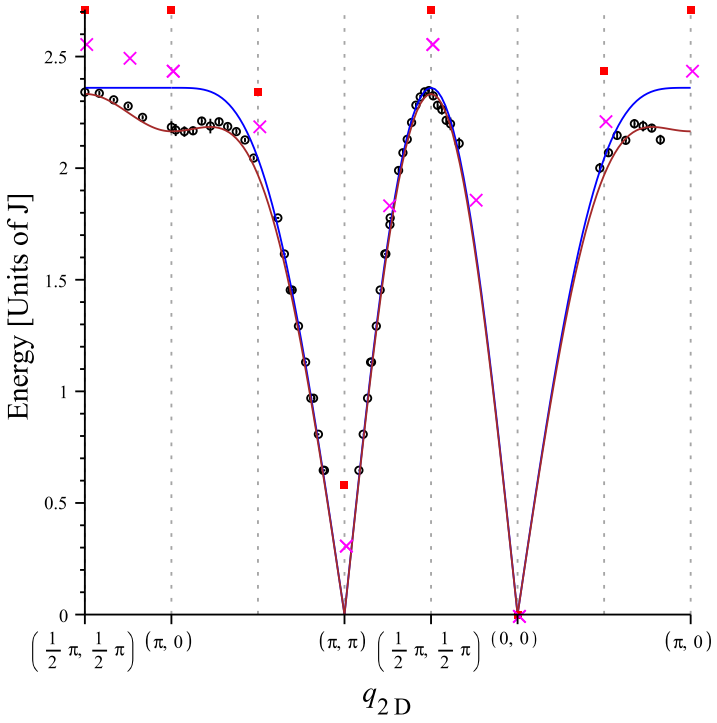

Figure 6.7: The energy dispersion of the 2DQHAFSL represented by a scan through Q_{2D} space. The solid blue and brown lines are the LSW prediction for nearest and nearest plus next-nearest neighbors (Eqn. (2.40) and (2.61)). For nearest neighbor dispersion a quantum renormalization of 1.18 is used as determined by [23]. For the nearest plus next-nearest neighbor dispersion a scaling of 1.25 is chosen, see text for comments. The black circles are neutron scattering data for CFTD obtained by N.B. Christensen *et al.* [23], where the error bars are so small, that they are contained within the symbol. The red squares and the pink diagonal crosses are the ED data from RLexact for 16-spin (4x4) and 32-spin ($\sqrt{32}$x$\sqrt{32}$) respectively.

nearest plus next-nearest neighbors respectively. For the pure nearest neighbor dispersion a quantum normalization of 1.18 is used [23]. In the case of nearest plus next-nearest neighbors a

scaling factor of 1.25 has been chosen together with a antiferromagnetic next-nearest neighbor coupling $J' = 0.067J$, the latter taken from Rønnow *et al.* [19]. The 1.25 scaling was chosen to fit the data in the best way. This is problematic, since the quantum renormalization is not a fitting parameter but a prefactor having a physical content, making it in principle possible to calculate. Hence, the scaling of 1.25 should be considered as no more than a scaling parameter used to make one point clear; the experimental data for CFTD by Christensen *et al.* can be explained from the Heisenberg model with nearest plus next-nearest neighbor coupling and with a weak antiferromagnetic J'. This was also observed by Rønnow *et al.* in their studies on CFTD, see Sec. 3.1.2 and [19]. Furthermore, Coldea *et al.* have drawn the same conclusion on another realization of the 2DQHAFSL, LCO [33].

Inspecting Fig. 6.7 one notes that the curve from nearest neighbor LSW theory (blue) fits the experimental results extraordinary well at all points in the Brillouin zone except between $(\frac{\pi}{2}, \frac{\pi}{2})$ and $(\pi, 0)$ in the left part of the dispersion and again going from $(\frac{\pi}{2}, 0)$ to $(\pi, 0)$. The problems that LSW theory faces at the $(\pi, 0)$ anomaly, and which as mentioned are solved when next-nearest neighbors are included, are also solved by the exact diagonalization results from RLexact for the 32-spin system. This is remarkable, since the Hamiltonian of RLexact only includes nearest neighbors. Hence, the $(\pi, 0)$ energy anomaly *is* an intrinsic property of the Heisenberg model with nearest neighbors, Eqn. (2.1).
The supression in energy for the 32 spin lattice at $(\pi, 0)$ wrt. $(\frac{\pi}{2}, \frac{\pi}{2})$ is $\frac{2.564-2.4444}{2.564} \approx 4.7\%$, a number that is slightly lower than the 7(1)% found by Christensen *et al.* [23] and the 6(1)% found by Rønnow *et al.* and both displayed in Fig.3.1. That the depressions are not equal in magnitude is to be expected, since the numerical results are based on finite systems. Note also that the red squares in Fig. 6.7 display no supression in energy at $(\pi, 0)$, a result in complete accordance with Rønnow *et al.* who note, that this implies a significant number of spins (at least greater than 16) to be involved in the quantum effect that lowers the energy at this point in q-space.
Another feature that deserves a comment, is the fact that the ED based results are placed energetically higher than the LSW predictions. This is illustrated clearly at e.g. (π, π), which has a nonzero energy as opposed to what is expected from LSWT. This pathologic feature is a finite size effect. The nature of this effect can be revealed by plotting the energy gap vs. $1/N$. This is done in Fig. 6.8. The straight line clearly illustrates the $1/N$ dependence of the energy gap, going to zero as N goes to infinity, assuring that we need not worry about the gap inherent in the numerical data.
Having convinced ourselves about the behavior of this finite size effect, it makes sense to scale the experimental data from N. B. Christensen *et al.* such that the point $(\frac{\pi}{2}, \frac{\pi}{2})$ coincide with the ED result from RLexact for the 32 spin lattice. The reason the the point $(\frac{\pi}{2}, \frac{\pi}{2})$ is chosen, is that, it is with respect to the energy in this point, that the energy of $(\pi, 0)$ is suppressed. In Fig. 6.9 a plot of the scaled experimental data is seen. There is no new information in Fig. 6.9, but the way data is presented, emphasizes the conclusion that can be drawn on background Fig. 6.7: The $(\pi, 0)$ energy anomaly is a generic property of the Heisenberg model with nearest neighbors only, Eqn. (2.1). Before a conclusion can be drawn, it is interesting to note from Fig. 6.7, that between $(\frac{\pi}{2}, 0)$ and $(\pi, 0)$ the energy is also depressed relative to nearest neighbor LSWT. In this model the dispersion is increasing when going from $(\frac{\pi}{2}, 0)$ to $(\pi, 0)$, but here it is seen to decrease from a local maximum at $(0.64\pi, 0)$ determined from differentiation of the nearest plus next-nearest LSWT dispersion, Eqn. (2.61). The value of this local maximum is ≈ 1.31 whereas the local maximum at $(\frac{\pi}{2}, \frac{\pi}{2})$ takes the value 1.6. Inspecting Fig. 2.4 one finds that this difference is a property of a C_4 rotational symmetry of the $(\pi, 0)$ anomaly.

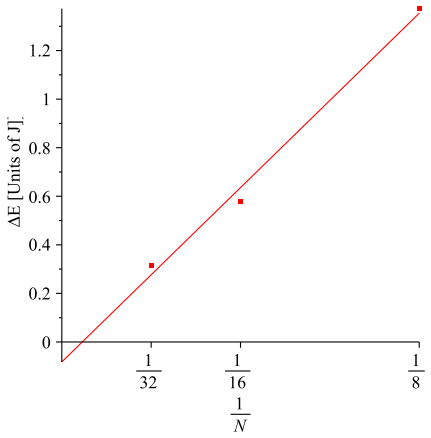

Figure 6.8: The energy gap vs. the inverse sample size $1/N$. The three data point come from the samples of 2x4, 4x4 and $\sqrt{32}$x$\sqrt{32}$, of which only the last two are displayed in Fig. 6.7. The red solid line is a linear fit yielding $\Delta m = -0.0821 + 11.49\frac{1}{N}$

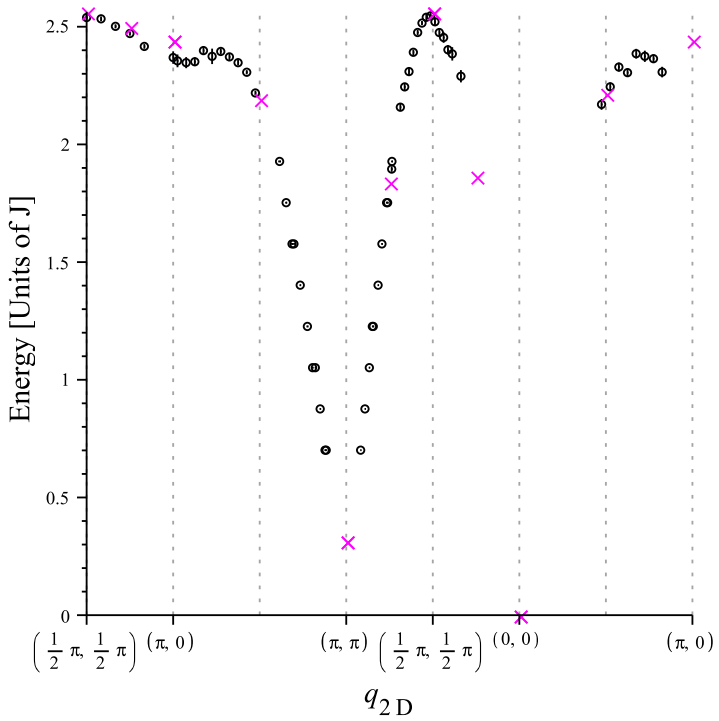

Figure 6.9: A scaled energy dispersion. The experimental CFTD data (open circles) from N. B. Christensen *et al.* is scaled such that it coincides with ED data for the 32 spin lattice (pink diagonal crosses) at the point $(\frac{\pi}{2}, \frac{\pi}{2})$. The scaling factor is 1.085 and the error bars of the experimental data are so small, that they are contained within the open symbols.

We are now ready to conclude on Fig. 6.7. From the above we have two models that describe the observed CFTD neutron scattering data, with special focus on the $(\pi, 0)$ anomaly. The first possibility is the LSW result of the Heisenberg model with nearest plus next-nearest neighbors and with a 1.25 scaling (brown line). An alternative explanation is provided by the ED result from the 32 spin lattice based on the Heisenberg model with *only nearest neighbors*, which also captures the $(\pi, 0)$ anomaly, though with the energy having almost the same magnitude as the experimental results and with a finite size effect. The ED result also reveals that more than 16 spins are needed for the quantum nature of $(\pi, 0)$ to be visible.
So how should we understand this? Well, since the ED result based on the nearest neighbor Heisenberg model captures the essential physics, one should conclude, having in mind that the LSW dispersion with nearest plus next-nearest neighbors is an approximate result, that the 2DQHAFSL with nearest neighbors only, indeed has the $(\pi, 0)$ anomaly as an intrinsic feature. If one had the computational power, it seems reasonable to expect that ED results at the $(\pi, 0)$ anomaly for samples larger than 32 sites, would converge relatively fast to the magnitude of the anomaly for thermodynamically large systems, on which real experiments are performed. The 36 spin lattice is within reach of RLexact, but at the moment the convergence criteria, discussed in Sec. 5.4.3, has to be set so weak, that the results are not reliable due to numerical errors. This may be solvable if the optimization discussed in Sec. 5.8 is implemented.

6.3.1 The dynamical structure factor

Step2 of RLexact produces the longitudinal dynamical structure factors $S^{zz}(\mathbf{q}, \omega)$, as they would appear in an ideal experiment. These results are very important, since they compare directly to the numerical data of Lüscher *et al.* [39], Dagotto *et al.* [30] and the experimental results of among others Christensen *et al.* [23] and Rønnow *et al.* [19]
Before reporting the dynamical structure factors for larger systems, it is necessary to compare selected results of RLexact with hand-calculated results and results from the literature in order to test the reliability of RLexact. This was done for the 2x1, 4x1 and the 10x1 chain, which was also investigated numerically by Müller *et al.* [35], as displayed in its original version in Fig. A.1.
Finally the results for these systems were tested against the sum rule as stated in Eqn. (5.21), which predicts the individual terms as well as the total sum. The results of this, is found in Appendix A.1. The results agree within the precision of RLexact and convince us that RLexact is reliable. However, during the work with RLexact it was discovered that $S^{zz}(\mathbf{q}, \omega)$ for the $\sqrt{32}$x$\sqrt{32}$ lattice were wrong by a factor of 4. This is not an error in RLexact, but originating from the input file and the Perl scripts. The reason is, that a $\sqrt{N}$x$\sqrt{N}$ lattice is made from a NxN lattice only with q-vectors obeying $q_x + q_y = 2n$, n being an integer. Hence, remembering to divide all $S^{zz}(\mathbf{q}, \omega)$ for the $\sqrt{32}$x$\sqrt{32}$ lattice by a factor 4, we shall continue to report the results for the dynamical structure factor.

This is done by circle plots inspired by the procedure used by Lefmann & Rischel [34] and Lüscher & Läuchli [39] presented in Sec. 4.2.1, however with a somewhat different visual setup. As was noted by the latter two, results for the magnetization close to saturation are to be interpreted with scepticism due to small Hilbert spaces. Following the rule of thumb stated in [39], gives us that only subspaces with $m \leq 1/2 - 4/N$ will be representative for thermodynamically large systems. For $N = 36$ ($N = 32$) this demands $m \leq 14$ ($m \leq 8$) .
In Fig. 6.10 the simulations of $S^{zz}(\mathbf{q}, \omega)$ at zero field ($m/N = 0$, $h = 0$) are presented for the 16 and 32 spin lattice. The red (blue) diagonal crosses mark the position of the largest (second largest) dynamical structure factor.
In Figs. 6.11, 6.12 and 6.13 more data for the structure factor is presented. The axes, the

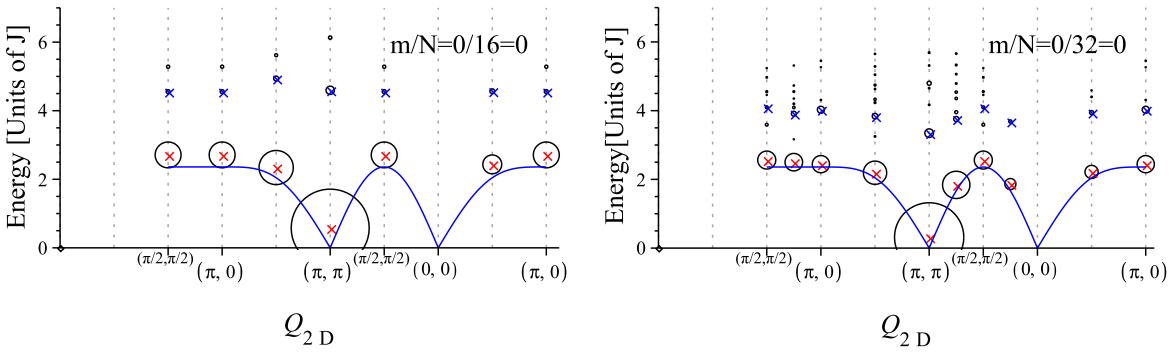

Figure 6.10: Results from step2 of RLexact for $S^{zz}(\mathbf{q},\omega)$. The scan direction which is along the ordinate is as indicated by the dashed blue line in Fig. 2.3. The solid blue line displays the LSW nearest neighbor prediction. The red (blue) diagonal crosses are the centers of the circles representing the largest (second largest) dynamical structure factors. In this figure $m = 0$ for all samples. The left and right panel displays the 16-spin (4x4) and the 32-spin ($\sqrt{32}$x$\sqrt{32}$) system respectively. Only $S^{zz}(\mathbf{q},\omega)$ with $\frac{S^{zz}(\mathbf{q},\omega)}{N} > 10^{-4}$ are displayed. The radius of each circle is $1.5 \cdot \sqrt{\frac{S^{zz}(\mathbf{q},\omega)}{N}}$, where N is the number of sites in the lattice.

center marking and the area of the circles are to be interpreted as described above. Fig. 6.11 displays $S^{zz}(\mathbf{q},\omega)$ for selected systems in which m/N takes the values $m/N = \{\frac{1}{8}, \frac{1}{4}, \frac{3}{8}\}$. Hence, the columns have fixed N and variable m/N while the rows have fixed m/N and variable N. Fig. 6.12 contains almost the same information as the middle row of Fig. 6.11, but includes one panel more[10].
Since the higher the number of spins the more reliable result, Fig. 6.13 presents selected data for the 36 spin 6x6 lattice, which is the largest lattice investigated. The brown line in the upper left panel is the nearest neighbor ferromagnetic LSW dispersion in zero field, Eqn. (2.62).

Before we can continue to the discussion of the dynamical structure factor, it is necessary to present a figure that, like Fig. 6.7, is comparable to the experimental literature. This is done in Fig. 6.14. Here, the left panel displays at each **q**-value the pole for the largest structure factor and the sum of the remaining smaller poles for the 16 and 32 spin lattices, and the CFTD data from Christensen *et al.* [23]. All poles are scaled relatively to the value in $(\frac{\pi}{2}, \frac{\pi}{2})$ and plotted together with the LSW prediction, Eqn. (2.67). The LSW prediction is constant along the magnetic ZB between $(\frac{\pi}{2}, \frac{\pi}{2})$ and $(\pi, 0)$. It is seen that the 32 spin ED results have the same tendency as the experimental data presented, but the intensity reduction is not as strong as experimentally determined. Christensen *et al.* reported that 54(15)% of the LSW predicted intensity was removed, while the corresponding percentage for the ED results of the 32 spin lattice are $(3.896 - 3.543)/3.896 \approx 9\%$.

[10] If this three-panel row had been included in Fig. 6.11, all panels would have been too small.

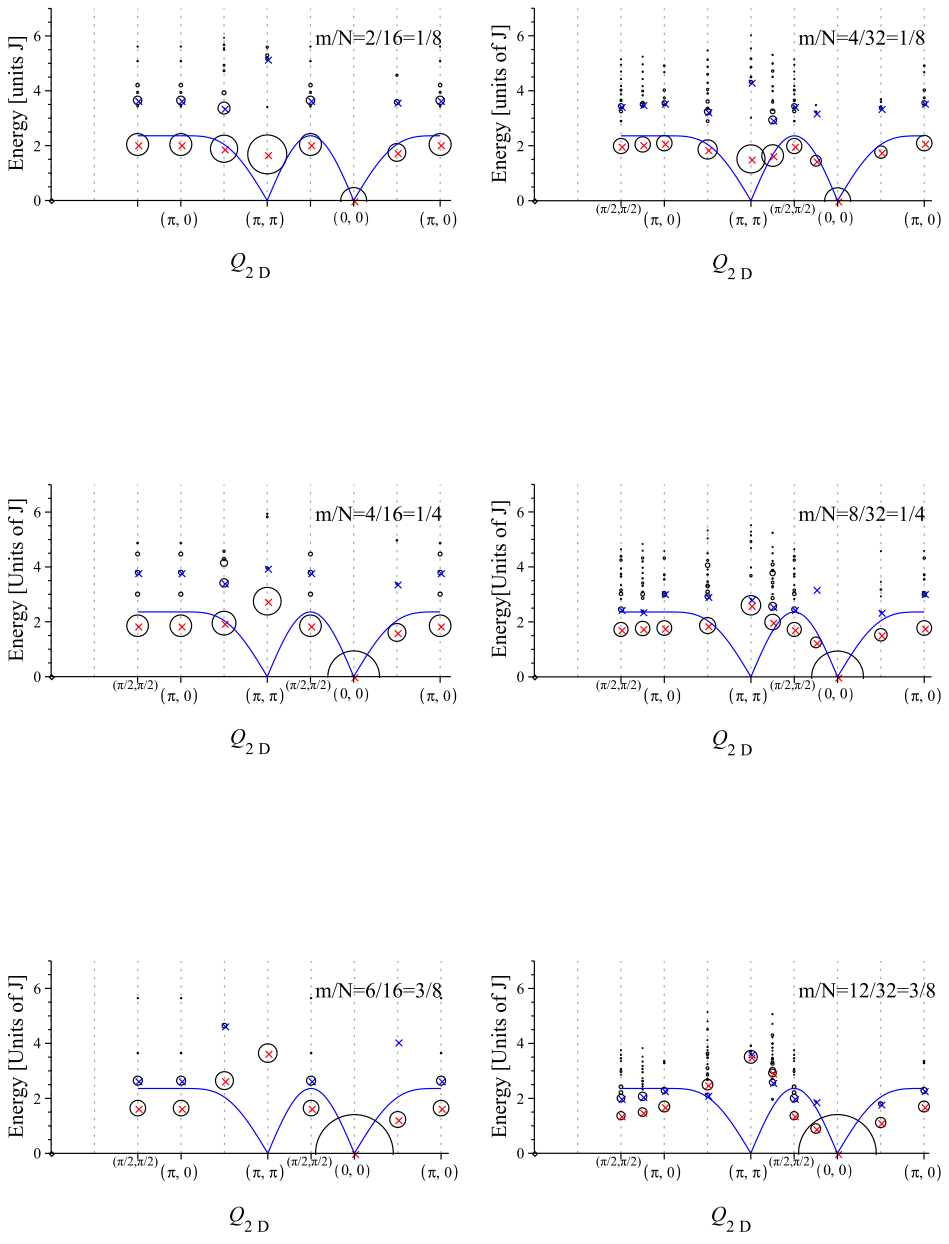

Figure 6.11: Results from step2 of RLexact for $S^{zz}(\mathbf{q},\omega)$ in a field. The scan direction which is along the first axis is as indicated by the dashed blue line in Fig. 2.3 and the second axis is the energy of the system in units of J. First column shows data from the 16-spin lattice and second column of the 32-spin lattice. The red (blue) diagonal crosses mark the position of the largest (second largest) dynamical structure factor. In the upper row all systems have $m/N = \frac{1}{8}$. The middle row has $m/N = \frac{1}{4}$ and the bottom row has $m/N = \frac{3}{8}$. Only $S^{zz}(\mathbf{q},\omega)$ with $S^{zz}(\mathbf{q},\omega)/N > 10^{-4}$ are displayed. The radius of each circle is $1.5 \cdot \sqrt{\frac{S^{zz}(\mathbf{q},\omega)}{N}}$, where N is the number of sites in the lattice. The blue line are the nearest neighbor LSW dispersion *in zero field*, Eqn. (2.40), included for visual reference.

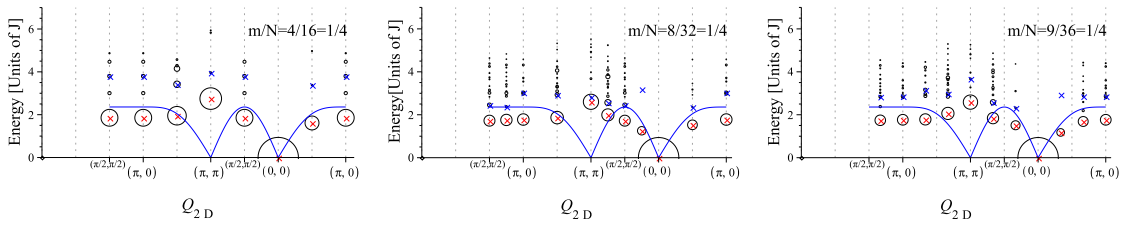

Figure 6.12: Results from step2 of RLexact for $S^{zz}(\mathbf{q},\omega)$. The scan direction which is along the first axis is as indicated by the dashed blue line in Fig. 2.3 and the second axis is the energy of the system in units of J. All panels have $m/N = \frac{1}{4}$. The red (blue) diagonal crosses mark the position of the largest (second largest) dynamical structure factor. Only $S^{zz}(\mathbf{q},\omega)$ with $S^{zz}(\mathbf{q},\omega)/N > 10^{-4}$ are displayed. The radius of each circle is $1.5 \cdot \sqrt{\frac{S^{zz}(\mathbf{q},\omega)}{N}}$, where N is the number of sites in the lattice. The blue line is the nearest neighbor LSW dispersion *in zero field*, Eqn. (2.40), included for visual reference.

An interesting feature is that along the magnetic ZB, when the value of the largest pole decreases, the sum of the smaller poles increases. This is contrary to all other scan-intervals. Quantitatively the highest pole decreases in absolute numbers by 0.352, while the sum of the remaining poles increase by 0.331, indicating that the spectral weight is almost conserved. This hypothesis is investigated in the following calculation

$$\frac{\left(S^{zz}_{\text{max}}(\pi,0) + S^{zz}_{\text{rest}}(\pi,0)\right) - \left(S^{zz}_{\text{max}}(\frac{\pi}{2},\frac{\pi}{2}) + S^{zz}_{\text{rest}}(\frac{\pi}{2},\frac{\pi}{2})\right)}{S^{zz}_{\text{max}}(\frac{\pi}{2},\frac{\pi}{2}) + S^{zz}_{\text{rest}}(\frac{\pi}{2},\frac{\pi}{2})} \approx -0.5\% \tag{6.1}$$

This reveals that only 0.5% of the total spectral weight is lost going from $(\frac{\pi}{2},\frac{\pi}{2})$ and $(\pi,0)$. Inspired by this, it makes sense to make a new plot, displaying at each q-point the total spectral weight relative to the total spectral weight in $(\frac{\pi}{2},\frac{\pi}{2})$. This is done for the 32 spin ED results in the right panel of Fig. 6.14, from which it is seen, that the *total spectral weight* relative to the weight of $S((\pi,\pi),\omega)$ is very well described by LSWT. Hence, Fig. 6.14 suggests that a possible explanation of the $(\pi,0)$ intensity anomaly observed experimentally by e.g. Christensen *et al.* [23], could be, that the intensity lost in the dominating pole is gained in the sum of the weaker poles. In more physical terms: *The spectral weight lost in the one-magnon branch ends in the multi-magnon continuum.*

6.3.2 Discussion and comparison with the literature

We are now ready to interpret the results for the dynamical structure factors and compare with the literature. This will be done for one figure at a time, ending up with a final conclusion. But before starting this discussion it is important to make clear which type of information we are seeking to extract.

The main purpose of this thesis is with respect to data analysis, to gain physical insight to the 2DQHAFSL and compare this with the neutron scattering data from CFTD by Christensen *et al.* [23]. To complete this task satisfactory it is during the data analysis necessary to investigate the strength and weaknesses of ED results based on finite systems.

For the purpose of gaining physical insight it is the effect of physical parameters such as h-field

(magnetization) that should be investigated and it is furthermore adequate to focus on as large systems as possible, still using the smaller systems as check for consistency. On the other hand, if one should understand the nature of finite systems the parameter that one should vary is the system size. Hence, for the purely physical discussion we shall focus on the columns of Fig. 6.11, Fig. 6.13 and 6.14. To draw conclusions on finite systems however, we should direct our attention to the rows of Fig. 6.11 and Fig. 6.12, which is chosen such that the panels are comparable, since they within each row has the same value of m/N.
In the discussion to come, we shall mainly focus on the physical information, but when relevant information about the nature of finite systems is accessible these will be pointed out.

The results of Fig. 6.10 illustrate that in zero field, the spectral weight is concentrated about the X-point(π,π), with the highest structure factor belonging to exactly this point and with a tendency of the surrounding points to have slightly more weight than the remaining points, though being relatively homogeneously spread out. In $(0,0)$ there is no structure factor, consistent with the theoretical prediction Eqns. (5.18), (5.19) and (5.20) in zero field, and with the result of Lüscher *et al.*, see upper left panel of Fig. 4.4. Note again, that $S^{zz}(\mathbf{q},\omega)$ at (π,π) does not have zero energy due to the $1/N$ finite size effect illustrated in Fig. 6.8.
Another feature that catches the eye, is the gap between the lowest excitations (the circles with red center), which we interpret as a one-magnon branch, and the beginning of the smaller closely spaced poles, interpreted as the SW continuum (blue diagonal crosses). Both results for the 16 and 32 spin lattice agree on the one-magnon branch being centered about an energy of $2.5J$ and with a substantial gap to the energetically higher multi-magnon continuum. However, there seems to be disagreement about the size of the gap; while the 16 spin result predicts the gap to be $\approx 1.5J$, the corresponding result for the 32 spin lattice is $\approx 1J$. This disagreement is probably due to the 16 spin lattice being so small, that finite size effects have a strong influence, that the results do not compare to the thermodynamical limit, to which the 32 spin results probably have almost converged. The latter is also found by Lüscher *et al.*, see Fig. 4.4 upper left.
Finally, one notes that a virtual line through the poles between $(\frac{\pi}{2},\frac{\pi}{2})$ and $(\pi,0)$ in the right panel of Fig. 6.10 tend to have a negative slope in the scan direction. Following the scan-direction from $(\frac{\pi}{2},0)$ to $(\pi,0)$ the slope is positive. The pink diagonal crosses in Fig. 6.7 display exactly the same behavior.
As a final remark to Fig. 6.10 the number of poles is much greater for the 32 spin system than for the 16 spin system. Since the system size is the only difference between the simulations leading to these two panels, the deviation must be due to a finite size effect, revealing that the smaller the system the smaller the number of poles. But, one also notes that the tendency in the position of the poles is the same. Hence, even very small systems can display the tendency of larger systems, but details are not accessible. Therefore, in order to look for details in thermodynamically big systems, the small systems are disqualified.

In Fig. 6.11, a few of the panels are directly comparable to results from the literature. This is the case for the second panel displaying the results for the 32 spin lattice with $m/N = 1/8$, which compares directly to third panel of Fig. 4.4, where $m = 0.125$. Comparing these two figures one should have in mind, that in Fig. 6.11 the path from $S = (\frac{\pi}{2},\frac{\pi}{2})$ to $M = (\pi,0)$ is chosen as the start of the Q_{2D}-scan. In Fig. 4.4 the same path has been reversed going from M to S and is now placed in the end of the Q_{2D}-scan. Taking this potential confusion into account, it is seen, that the figures display consistent results; the spectral weight is centered around $X = (\pi,\pi)$ which also corresponds to the lowest energy, the one magnon excitation branch is centered around an energy of $\approx 2J$ and the gap to the multi-magnon continuum is

about 1J.
That these selected results of RLexact agree with the results of Lüscher *et al.* for both zero- and non-zero field convince us even more, that RLexact can be trusted.

Continuing to Fig. 6.11, we obtain information about how $S^{zz}(\mathbf{q},\omega)$ responds when a magnetic field is turned on. The most conspicuous effect which is clear from all panels of Fig. 6.11, is that $S^{zz}((\pi,\pi),\omega)$ no longer has a vanishing energy; from the 16 and 32 spin columns it is clear, that this energy is increasing with the field. This is consistent with [39], see Fig. 4.4.
Another tendency which is displayed in both the 16 and 32 spin columns, is that the spectral weight at (π,π) decreases when the field is increased while the weight at $(0,0)$ increases with the field. These two features are well understood. The decrease in spectral weight at (π,π) is the staggered moment approaching zero while the increment at $(0,0)$ is the ferromagnetic peak becomming more and more visible.
In order to understand the gap between the single magnon branch and the start of the multi-magnon continuum, we shall focus on second column of Fig. 6.11, because of the relatively high number of spins. It is clearly seen, that the gap approaches zero when the field is increased, in accordance with the observations by Lüscher *et al.* presented in Fig. 4.4. When Fig. 6.13 is discussed we shall return to this feature.
In the review of the numerical work, Chapter 4, it was noted, that the scan between $(\frac{\pi}{2},\frac{\pi}{2})$ and $(\pi,0)$ exhibits a branch splitting in two relatively high intensity branches for m/N between 0.35 and approximately 0.375, where they start melting together in a continuum that shrinks into the uppermost branch as saturation is approached. The value $m = 0.35$ corresponds to $h = 3.16J$ [39] which for LCO (CFTD) having $J = 136$ meV ($J = 6.19(2)$ meV) corresponds to $h \approx 7425$ T ($h \approx 338$ T), which are unaccessible high fields.
The results of this work is not as detailed as [39] and therefore it is not possible from Fig. 6.11 to see the before-mentioned continuum between branches, seen in the last panel of the second column of Fig. 4.4. However, one notes from the bottom row, that a branch splitting is starting to form. Also this we shall return to in Fig. 6.13.
A final remark to the physics of Fig. 6.11 concerns the lower right panel displaying $m/N = 12/32$. Note that the pole at $(\pi,0)$ has higher energy than the pole at $(\frac{\pi}{2},\frac{\pi}{2})$. This relative position is reversed when compared to case of zero field. This must be a temporary effect, since the dispersion is flat at saturation, see Fig. 6.13 upper left.

Fig. 6.13 presents the results based on the biggest cluster investigated; the 6x6 lattice, and is in that sense the most reliable result of this thesis work. From the upper left corner it is seen, that the poles of the $m/N = 17/36$ are very well described by the nearest neighbor ferromagnetic LSW dispersion. This is to be expected, since for $m/N = 18/36 = 1/2$ we have the ferromagnetic state.
Returning to the gap between the one- and multi-magnon branches discussed above, it is from the 36-spin results even clearer what the 32-spin results suggested: At low fields the gap is sizable but closes as the field is increased, in the end melting together with the ferromagnetic dispersion branch. Also the number of poles is dependent on the field strength such that high fields have the smallest number of poles[11], whereas intermediate and low fields have a greater number of poles.
From [39] we know that the branch splitting occurs most pronouncedly between $m/N = 0.35$ and 0.37. For the 36-spin lattice with $m = 12$, $m/N = 0.33$ and in the corresponding panel of Fig. 6.13 the branch splitting is seen relatively clear in the interval between $(\frac{\pi}{2},\frac{\pi}{2})$ and $(0,0)$.

[11] Since it was not possible to run RLexact for $m \leq 5$ with a acceptable value of RITZ_CONV we must use Fig. 6.10 and Fig. 6.11 to argue for this statement at low fields.

When comparing the results of this work with [39], see Fig. 4.4, it is clear that [39] has more points pr. q-position in Q_{2D} space. This is due to two reasons; i) [39] have by interpolation along a line connecting the lowest lying poles, moved the structure factors originating from different q-points and close-lying m/N-values, thereby enabling the plotting of more clusters in the same plot. This has not been done in this thesis work and it is not clear to me why this procedure is correct ii) In this thesis work a choice of only plotting structure factors with $S^{zz}(\mathbf{q},\omega)/N > 10^{-4}$ has been made. Since [39] states nothing about a similar choice it is possible, that they have plotted every pole regardless of its weight.

The $(\pi, 0)$ intensity anomaly

Fig. 6.14 is the main result of this thesis work, that together with Fig. 6.7 relates directly to the experimental work on CFTD discussed in Chapter 3. We can from the left panel of Fig. 6.14 draw the conclusion that the 32 spin lattice indeed does exhibit an intensity reduction of the strongest pole at $(\pi, 0)$ wrt. LSWT, but with a $\approx 9\%$ reduction, which is a lot smaller than the experimentally determined 54(15)% reduction of CFTD [23]. It is also seen, that the 16 spin lattice does not exhibit a $(\pi, 0)$ strongest-pole intensity reduction. This is interesting, because the situation wrt. the energy anomaly at $(\pi, 0)$, seen in Fig. 6.7 was same; the experimental results are modelled by the 32 spin lattice but not by the 16 spin lattice. Hence the remark by Rønnow *et al.* [19], that the phenomenon governing the $(\pi, 0)$ anomaly includes more that 16 spins is strengthened.
It was from the right panel of the same figure revealed, that the total spectral weight of the ED data, when going from $(\frac{\pi}{2}, \frac{\pi}{2})$ to $(\pi, 0)$, is conserved along the magnetic zone boundary, despite the reduction in the strong one-magnon pole. It was also seen that the 'lost' spectral weight ended up, in what we named the multi-magnon continuum. *The mutual dependence of the one- and multi-magnon at the magnetic zone boundary* is very interesting, since the same correlation is not present other places in the BZ. This could be a possible explanation of the $(\pi, 0)$ intensity anomaly observed in CFTD by neutron scattering [23]. A related conclusion is drawn in [38], which based on QMC simulations estimates that the spin-interaction neglected in LSWT, at the point $(\pi, 0)$ lowers the energy by almost 10% and transfers $\approx 40\%$ of the one-magnon spectral weight into the multi-magnon continuum. At $(\frac{\pi}{2}, \frac{\pi}{2})$ the excitation energy is found to be almost unaffected be these interactions, and the continuum weight is much smaller. It could indeed be very interesting to carry out an neutron scattering experiment on f.x. CFTD, which investigated this further.

Concluding comparison with Lüscher & Läuchli

Having discussed the figures of this thesis work that present information on the dynamical structure factor, we are now able to state a few concluding remarks on the 2DQHAFSL, related to the wotk by Lüscher and Läuchli [39].
In Sec. 4.2.3 where the numerical work from the literature were discussed, we ended up with four concluding remarks and we shall when possible try to fit the conclusion on the dynamical structure factor into these categories. Since the physics of most features were already discussed in Sec. 4.2.3, we will in these occasions not repeat the same arguments again, but merely refer to Sec. 4.2.3.
a) Like [39] we also find that the spectral weight, which at zero field is concentrated at (π, π), gradually smear out over the entire BZ when the field is increased.
b) This work also finds that the energy of the X-point (π, π) excited magnons is increased

for increasing field. From the lower right panel of Fig. 6.13 it seems reasonable to conclude that the X-point Goldstone mode present at zero field moves up to a higher energy, as soon as the field is turned on. It would have been nice to base this conclusion on a lattice with $N \geq 36$. Unfortunately this have not been possible due to reduced capacity and time limits on the DCSC cluster.
Since we in this work have not plotted the LSW dispersion with field, it is not, other than for $m = 0$, possible to verify the tendency in [39], that the ED results at the X-point are slightly energetically higher lying than the LSW prediction.
c) This work concludes that the gap between the one magnon excitations and the two- and multi-magnon continuum closes for increasing field (Fig. 6.13) and that at fields close to saturation only one relatively well-defined branch exists (upper row of Fig. 6.13). In this relation another interesting feature is noted from the rows of Fig. 6.11, namely that the gap seems to be closing for increasing system size. This indicates that a part of the explanation of the gap is a finite size effect. On the other hand a well-defined branch is to be expected when h reaches saturation, since the ferromagnetic state is classical without a continuum for $T = 0$. The conclusion must be that the expected gap-closing for increasing fields, occurs earlier when N is large.
d) As far as the branch splitting is concerned, we can from the last row of Fig. 6.11 which has $m/N = 3/8 = 0.37$, and the first panel in the second row of Fig. 6.13 with $m/N = 12/36 \approx 0.33$, see the tendency of a splitting behaving as the one found in [39]. But, the number of structure factors in the region are so few, that had it not been for the profound work of Lüscher and Läuchli [39] this tendency would not have been noted. However, in [39] it seems as if not much attention were directed towards this splitting. This we will do here, since the splitting occurs right where the $(\pi, 0)$ anomaly exists. Using the results of both [39] and this thesis work, it is possible to note that the lower branch at $(\pi, 0)$ is placed at an energy of approximately $1.8J$, see Fig. 4.4 and the $m/N = 1/3$ panel of Fig. 6.13. This *in-field* energy reduction of about 10% could be related to the *zero-field* reduction of 7(1)% found by Christensen *et al.* [23], since both occur at the magnetic ZB. However, it is interesting that the observed branch splitting has a local maximum and minimum in width at $(\frac{\pi}{2}, \frac{\pi}{2})$ and $(\pi, 0)$ respectively. The experimentally observed $(\pi, 0)$ anomaly [23, 19, 33] in the physical realizations of the 2DQHAFSL behaves opositely, with $(\pi, 0)$ deviating the most from LSWT.
e) A phenomenon that is possible to investigate in this thesis work is to which degree small finite systems exhibit the same features as the bigger systems. [39] only investigates clusters of $32 \leq N \leq 64$, whereas this work includes clusters of 8 and 16 spins as well. From the last row of Fig. 6.11 (16 spin and 32 spin) one notes that the branch splitting with some enthusiasm is visible for both lattices. This is in contrast to the $(\pi, 0)$ anomaly in the energy dispersion and the intensity, which the 16 spin lattice does not exhibit, as is noted both in [19] and in the discussion above.

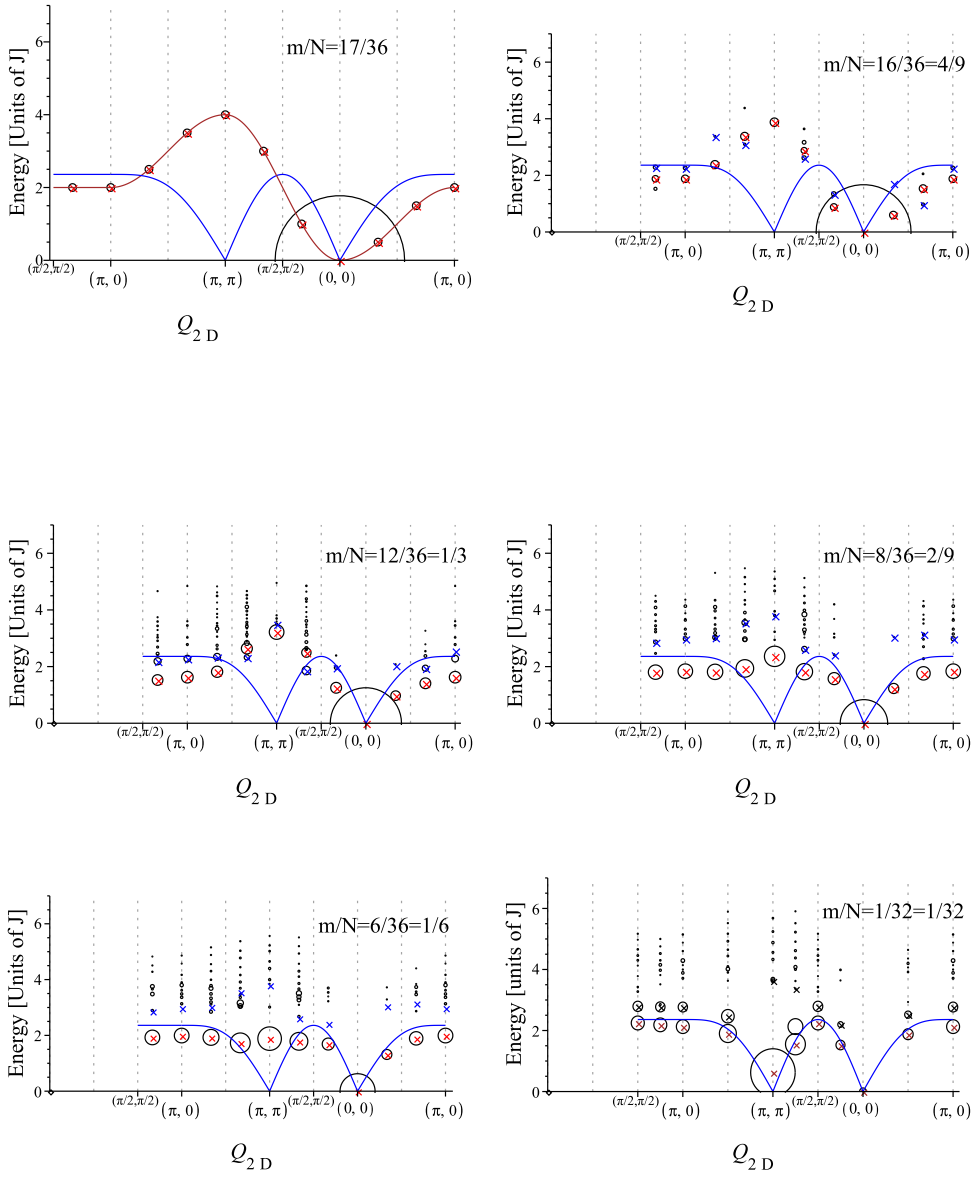

Figure 6.13: Results for $S^{zz}(\mathbf{q},\omega)$ from step2 of RLexact for the 36 spin 6x6 lattice (the last panel with different colors is based on the 32-spin lattice). The scan direction which is along the first axis is as indicated by the dashed blue line in Fig. 2.3 and the second axis is the energy in units of J. The red (blue) diagonal crosses mark the position of the largest (second largest) dynamical structure factor. For the panel displaying the 32 spin lattice the brown (black) diagonal crosses mark the position of the largest (second largest) dynamical structure factor. Starting from the upper left corner and continuing in the reading direction the values of m/N are $17/36, 16/36, 12/36, 8/36, 6/36, 1/32$. The brown line in the upper left panel is the nearest neighbor ferromagnetic LSW dispersion in zero field, see Eqn. (2.62) and Fig. 2.5. The blue line is the nearest neighbor LSW dispersion *in zero field*, Eqn. (2.40), which is included for visual reference. Only $S^{zz}(\mathbf{q},\omega)$ with $S^{zz}(\mathbf{q},\omega)/N > 10^{-4}$ are displayed. The radius of each circle is $1.5 \cdot \sqrt{\frac{S^{zz}(\mathbf{q},\omega)}{N}}$, where N is the number of sites in the lattice.

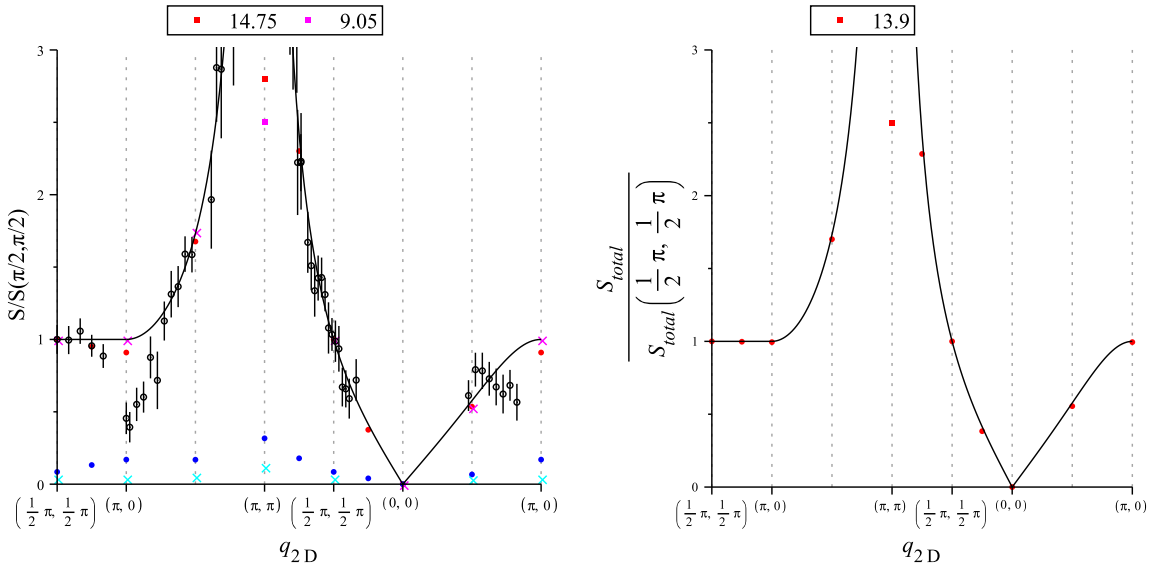

Figure 6.14: Left figure: The dynamical structure factor $S^{zz}(\mathbf{q},\omega)$ normalized wrt. the strongest pole in $(\frac{\pi}{2},\frac{\pi}{2})$. The scan direction which is along the ordinate is as indicated by the dashed blue line in Fig. 2.3. The solid red circles (pink diagonal crosses) represent the largest pole (sum of the remaining poles) of the 32 spin lattice. The solid blue circles (cyan diagonal crosses) represent the largest pole (sum of the remaining poles) of the 16 spin lattice. The black solid curve is the LSW prediction Eqn. (2.67). The red (pink) solid squares at (π,π) are lowered from their original value in order to make the figure readable and represent the 32 (16) spin lattice. Their true values are seen at the top. The open black circles are experimental neutron scattering data on CFTD, obtained by Christensen *et al.* [23]. The vertical solid lines are error bars. Note that the ED point for $\mathbf{q} = (\frac{3\pi}{4},\frac{\pi}{4})$ in the left side of the panel is covered by a CFTD-point. Right figure: The total spectral weight of $S^{zz}(\mathbf{q},\omega)$ normalized wrt. the strongest pole in $(\frac{\pi}{2},\frac{\pi}{2})$. Only results for the 32 spin lattice are displayed and the color-coding is as in the left panel.

Chapter 7

Outlook and conclusion

7.1 Outlook

Along with the elaboration of this thesis work, a number of ideas to how the work could be continued have emerged. These ideas can be divided into two groups as being related either to numerical or experimental work. We shall start in the numerical regime and the ideas will be listed pointwise below.

- An obvious idea is to enable RLexact to carry out exact diagonalization for larger systems. This is especially interesting at $m = 0$, which is the only m-value from which we can obtain information about the ground state properties. The goal should be either 36 or 40 sites for $m = 0$. However, the idea is easier to state than to carry out, since a success would require an optimization of RLexact. This optimization has been started with the beginning optimization of FindUnique. But, since it at the moment is impossible to complete ED of the 36-spin lattice at $m = 0$ even with RITZ_CONV= 10^{-1}, more optimization ideas are needed, in order to run this job within the two days time limit at DCSC. A candidate for this optimization is to invoke the spin-flip symmetry[1] present (only) in the $m = 0$ subspace. This would immediately lower the number of steps in the diagonalization-process by a factor of two. In an earlier version, RLexact was capable of this in one dimension, so this task should not be huge. The optimization of RLexact enabling it to run larger systems is properly a job for a computer scientist, or at least someone with more insight in the C-language than the author. The task is very important, since an optimization of the code is essential for keeping RLexact in game of producing relevant numerical work. Alternatively, access to a bigger cluster than DCSC or higher time limit at DCSC, would probably, with the present version of RLexact, facilitate the exact diagonalization of the 36 spin lattice with $m = 0$. With the present version of RLexact this job would at the DCSC cluster take about a week.

- Experimental neutron scattering results and numerical and theoretical work, agree that the ground state of the spin-$\frac{1}{2}$ AFM on a square lattice is of non-classical nature. The so-called RVB state described in Chapter 2, is a candidate for the ground state of this system. Therefore it would be highly relevant to develop RLexact, so that it can calculate the nature of the ground state, in particular the overlap between the RVB state and the exact ground state found by RLexact. However, this is despite its conceptual simplicity very hard to carry out from the programmers point of view. The reason is that RLexact

[1] When $m = 0$ the number of spin-up and spin-down are equal. Hence, half of the states can be obtained in one operation, when the other half is known.

produces a ground state in the basis of uniques, while the RVB state normally is defined from dimer coverings of the lattice. These two bases are incommensurable. Hence, the key to success is probably to define the RVB state on the background of Uniques, such that the two bases coincide.
Another development of RLexact could be to incorporate the concept of Ring Exchange as described in Chapter 2 into the Hamiltonian, in order to investigate the effects on the $(\pi, 0)$ anomaly.

- A number of small task can be carried out on RLexact. Among these are an optional incorporation of the input file for nearest neighbor coupling in RLexact. As mentioned in chapter 5, this input file is at the moment written manually. The reason that the automatic generation of the input file must be optional, is that future work could be based on systems with other couplings than nearest neighbors. Another idea could be the inclusion of a variable in step1.pl and step2.pl, which selects the jobs for q-points submitted to DCSC. At the moment RLexact submits N jobs for a N-spin system, of which only $N/4$ contain distinct physics due to C_4 symmetry of the square lattice, see Fig. 5.1.

- With the present version of RLexact it should be possible to obtain results for the dynamical structure factor for systems with $N > 36$ as long as m is relatively close to $N/2$. The limit for RLexact set by the dimension of the sub-blocks of the Hamiltonian, is at the moment given approximately by the $m = 0$ sub-space with $N = 36$, having the number of configurations $\binom{36}{18} \approx 9 \cdot 10^9$. This dimensionality is the same for a 64 spin system with $m/N \approx 1/8$ $\left(\binom{64}{8}\right)$ and a 48 spin system with $m/N \approx 0.21$ $\left(\binom{48}{10}\right)$. These results would be easily obtainable and directly comparable with e.g. [39].
Finally, experiments show a tiny anisotropy gap of 0.38 meV at the zone center [19], making it interesting to incorporate an anisotropy into selected calculation. This was however not done in this thesis work, but could be relevant in both spin wave calculations and as a new feature of RLexact.

We are now ready to suggest future work related to the physical conclusions of this thesis work. Like above, the different ideas will be stated point wise.

- The magnetic ZB branch splitting between $(\frac{\pi}{2}, \frac{\pi}{2})$ and $(\pi, 0)$ treated in this thesis work needs to be investigated further. This could be done in three ways.
i) A numerical investigation based on higher values of N and m should be carried out. With $N = 40$ one more point would be added along the magnetic ZB, and with $m \approx 13$ then $m/N = 0.325$, which is the regime relevant for observing the branch splitting. Since $\binom{40}{13} \approx 5 \cdot 10^9$, this is within reach of RLexact at the moment. Also numerical work on smaller systems would be relevant, since the results of this work suggest, that the branch splitting is present in both the 32 and 16 spin lattice
ii) An experimental investigation by neutron scattering with a field, on physical realizations of the 2DQHAFSL, could get us closer to an understanding of the physics behind the branch splitting. These experiments should focus on the regime $h \in [2.8; 3.5]$ (in units of J) where the results of this work suggest, that branch splitting first appears and then melts together in a temporary continuum. One question that would be answered from this, is whether the branch splitting is nothing but a finite size effect or a true nature of the 2DQHAFSL.
iii) If neutron scattering experiments reveal the branch splitting as being more than just a finite size effect, an investigation of the temperature dependence of the branch splitting

is relevant. The ED results of this thesis work have been carried out at zero temperature, and it could be interesting to investigate to which degree the possible branch splitting in physical realizations of the 2DQHAFSL exhibit a temperature dependence.
iv) Another very interesting neutron scattering experiment would be to investigate the correlation between the one-magnon branch and multi-magnon continuum along the magnetic ZB. This should be investigated both with and without field, and could possibly reveal if the intensity anomaly observed by Christensen *et al.* [23] could be explained by spectral weight moving from the one-magnon branch to the multi-magnon continuum, as the results of this thesis work suggest.

- The branch splitting and the $(\pi, 0)$ anomaly are in this work both shown to be intrinsic properties of the 2DQHAFSL. Since many parents of the high temperature superconductors are physical realizations of the 2DQHAFSL, it would be interesting to investigate if there is a connection between the field dependence of the two phenomenons.

7.2 Conclusion

This thesis work has by use of the program RLexact performed exact diagonalization (ED) studies of the spin-$\frac{1}{2}$ Heisenberg antiferromagnet on a square lattice, the so-called 2DQHAFSL. The project was originally inspired by results from neutron scattering experiments [23, 19], revealing an anomaly in both intensity and energy wrt. linear spin wave theory (LSWT), at the point $(\pi, 0)$ in the two-dimensional magnetic Brillouin zone. However, before the exact diagonalization studies could begin, it was necessary to complete a work on RLexact in order to run it parallelly on the cluster at Danish Center for Scientific Computing. This work had been started by others, but were left partly unfinished, meaning that critical parts of the program was uncompilable/unrunable. As the project developed, it turned out that the literature presents a number of numerical works on the 2DQHAFSL, especially a paper by Lüscher and Lächli [39], which facilitated a profound test of the reliability of RLexact after the parallelization had been completed. This paper was published in may 2009, which was about the time, where this project was defined. It took some time before the author of this thesis realized, that the extensive work of [39] covered a great part of the already defined thesis project.
Hence, most of the numerical results of this thesis work, changed from being 'first timers' to a reproduction of [39]. This was not so bad as it seems, since the reliability of RLexact could be extensively tested, and the results of [39] could be challenged and supplement this thesis work in essential places, such as the branch splitting.
The first data that was analyzed, lead to curves of the uniform magnetization and the susceptibility, as well as a prediction of the ground state staggered moment. The former two were found to be reliable, while the determination of the ground state staggered moment was associated with severe uncertainties/errors. However, these results were only part of the warming up. The main question that needed answer was the following: Is the $(\pi, 0)$ anomaly in intensity and energy along the magnetic zone boundary, found by neutron scattering experiments on CFTD, a generic property of the 2DQHAFSL with nearest neighbor coupling? The question was already treated in the literature, but RLexact was a perfect tool to challenge these results. The RLexact studies revealed that the $(\pi, 0)$ anomaly in energy was indeed an intrinsic property of the 32 spin 2DQHAFSL with nearest neighbors, though with the energy reduction being 4.7% as compared to the 6(1) and 7(1)% found on CFTD [19, 23], a physical realization of the 2DQHAFSL.
Concerning the intensity anomaly in $(\pi, 0)$ some interesting observations were done; the 32 spin lattice exhibited an $(\pi, 0)$ anomaly, with a reduction of about 9% in the one-magnon branch

wrt. LSWT. This should be compared with the 54(15)% measured on CFTD [23]. However, it was also revealed, that the sum of all poles at each q-point, being well described by LSWT, did not experience the same anomaly along the magnetic zone boundary. Concluding, these results suggest, that along the magnetic zone boundary and specifically at $(\pi, 0)$, the spectral weight lost in the one-magnon branch ends in the multi-magnon continuum. A paper based on QMC simulation [38] has a related conclusion.
An interesting remark is that the 16 spin lattice was found not to display any anomaly, neither in energy nor in intensity. This is for the energy in accordance with the literature, but it was not possible to find any reference on the intensity.
Inspired by Rønnow *et al.* [19] it was also investigated whether the $(\pi, 0)$ energy anomaly could be modeled when using linear spin wave theory including next-nearest neighbors. This was indeed the case, since the ED results were perfectly described by LSWT with nearest plus next-nearest neighbor coupling and with a 1.25 scaling.
The work hence suggested, that the CFTD results could be understood by two theories: The Heisenberg model with nearest neighbor coupling (exact results) and the approximative theory of spin waves in the same model but with an additional next-nearest neighbor coupling. From the perspective of modeling one should prefer the simplest model describing the phenomenon, i.e. the Heisenberg with nearest neighbors. However, it is necessary to carry out exact diagonalization studies on bigger systems in order to test convergence in the thermodynamical limit. Within the 2DQHAFSL, it seems that the 32 spin lattice with $m = 0$ simulated in this thesis work, wrt. system size is in line with the literature. However, in a few years it should be possible to extract ED results for the ground state of the 2DQHAFSL with $N = 36$ or 40, which was not accomplished in this work.
During the study of the literature and the analysis of the data for the dynamical structure factor $S^{zz}(\mathbf{q}, \omega)$ a very interesting feature emerged; in a plot of $S^{zz}(\mathbf{q}, \omega)$ a quite clear branch splitting occurred at the magnetic zone boundary between $(\frac{\pi}{2}, \frac{\pi}{2})$ and $(\pi, 0)$. In relation with the intensity and energy anomaly just discussed, this interval is very interesting. The results of this thesis work and the results by Luscher *et al.* [39], suggest that the well-defined one-magnon energy branch splits in two, when the magnetization passes $m/N \approx 0.32$ from below. The two branches exist for fields up to $m/N \approx 0.37$, at which the lower branch melts together with the upper, at this field-strength being well-described by LSWT. From the entire splitting process it is seen, that the upper branch is formed from the multi-magnon continuum approaching and concentrating at the LSWT predicted branch, while the lower, which has the highest spectral weight at all fields before the 'melting together', is situated below the LSWT prediction. An important remark to the branch splitting is, that it is more pronounced in $(\frac{\pi}{2}, \frac{\pi}{2})$ than in $(\pi, 0)$. This is contrary to the $(\pi, 0)$ anomaly, which deviates the most from LSWT at $(\pi, 0)$. Another remark is that the results of this work, although very poor at this point, seems to indicate that the splitting as opposed to the other magnetic zone boundary effects, exist for the 16 spin lattice.
I have not been able to come up with an explanation for the branch splitting, and will hence merely note that it is related to the energy gap between the one-magnon branch and the multi-magnon continuum. Furthermore it seems possible, that a relation between the branch splitting and the conservation of spectral weight along the magnetic zone boundary exists, even though the former only is observed with a field and the latter only exists in zero field.
At the moment the multi-magnon continuum is a topic of interest for neutron scattering experimentalists, and it will be interesting to relate the results of this thesis work to the experimental results in the years to come. However, due to the low spectral weight of the continuum structure factors, it is very hard to distinct these from the background, making it impossible or at least very time consuming from neutron scattering, to obtain experimental continuum results

as detailed as those based on numerical work. This illustrates the importance of corporation between the two fields.

Concluding, the main result of this thesis work is the ED investigation of the magnetic zone boundary features of the 2DQHAFSL: The $m/N \approx 0.33$ branch splitting, the zero-field conservation of total spectral weight at the magnetic ZB and the anomalies in energy and intensity of the one-magnon branch also along the magnetic ZB.
The latter two anomalies have been shown to be intrinsic properties of the 2DQHAFSL, supporting both results from the literature and what has been experimentally determined in CFTD. This altogether facilitates the description of CFTD by the 2DQHAFSL.
The in-field branch splitting and the zero-field conservation of spectral weight, that in this thesis work have been shown as intrinsic properties of the nearest neighbor Heisenberg model, might be important pieces in the puzzle of revealing the secrets of the magnetic zone boundary in the physical realizations of the 2DQHAFSL. It will be interesting to see if these two phenomenons relate to the idea of a RVB admixtured ground state.

Appendix A

Calculations

A.1 Handmade calculations of $S^{zz}(\mathbf{q},\omega)$

We shall in this section calculate $S^{zz}(\mathbf{q},\omega)$ for the simple 4x1 and 2x1 antiferromagnetic chains. When calculating $S^{zz}(\mathbf{q},\omega)$ by hand, the first thing to notice is that $|gs\rangle$ only lives in the $m=0$ subspace. This means, that only the inner products $\langle e|S^z_q|gs\rangle$ where $m_e \neq 0$ is vanishing.

A.1.1 4x1

Due to the above comment we only carry out calculations for the $m=0$ subspace and the calculations will be done on the basis of uniques.

$\|u\rangle$		a_n	H_{zz}
$\|1\rangle$	$\|0101\rangle$	2	-1
$\|2\rangle$	$\|0011\rangle$	4	0

It is readily seen from this simple case, that the allowed $\mathbf{q}$'s are $\mathbf{q} \in \{0,2\}$ for the unique $|1\rangle$ and that all $\mathbf{q}$'s are allowed for the unique $|2\rangle$. This means that for $\mathbf{q}=0$ in the ordered basis $\{|1\rangle,|2\rangle\}$ of Uniques we get the Hamiltonian

$$\mathbf{H} = \begin{pmatrix} -1 & \sqrt{2} \\ \sqrt{2} & 0 \end{pmatrix}$$

which by diagonalization yields the eigenvectors and eigenenergies

$$\begin{aligned} |gs\rangle &= \frac{1}{\sqrt{3}}(-\sqrt{2}|1\rangle + 2\rangle) \quad E=-2 \\ |e_3\rangle &= \sqrt{\frac{2}{3}}(\frac{1}{\sqrt{2}}|1\rangle + 2\rangle) \quad E=1 \end{aligned}$$

For $\mathbf{q}=2$ we get in the ordered basis the hamiltonian

$$\mathbf{H} = \begin{pmatrix} -1 & 0 \\ 0 & 0 \end{pmatrix}$$

which by diagonalization yields the eigenvectors and eigenenergies

$$\begin{aligned} |e_1\rangle &= |1\rangle \quad E=-1 \\ |e_2\rangle &= |2\rangle \quad E=0 \end{aligned}$$

For $\mathbf{q}=1$ and $\mathbf{q}=3$ the unique $|1\rangle$ is not defined , in both cases resulting in the hamiltonian[1] $\mathbf{H}=(0)$.
We are now ready to perform calculations and apply the sum rule Eqn. (5.21).

$$S_q^z|gs\rangle = \frac{1}{2}\left(-\sqrt{\frac{2}{3}}\frac{1}{2}(-e^{iq}+e^{2iq}-e^{3iq}+e^{4iq})|1\rangle + \sqrt{\frac{1}{3}}\frac{1}{2}(-e^{iq}-e^{2iq}+e^{3iq}+e^{4iq})|1\rangle \right) \quad \text{(A.1)}$$

We now take the inner product of Eqn. (A.1) with the exited states $|e_1\rangle, |e_2\rangle$ and $|e_3\rangle$. We get

$$\langle e_1|S_q^z|gs\rangle = \langle 1|S_q^z|gs\rangle = \frac{1}{2\sqrt{6}}(-e^{iq}+e^{2iq}-e^{3iq}+e^{4iq}) \quad \text{(A.2)}$$

$$\langle e_2|S_q^z|gs\rangle = \langle 2|S_q^z|gs\rangle = \frac{1}{4\sqrt{3}}(-e^{iq}-e^{2iq}+e^{3iq}+e^{4iq}) \quad \text{(A.3)}$$

$$\begin{aligned}\langle e_3|S_q^z|gs\rangle &= \langle 3|S_q^z|gs\rangle = \frac{\sqrt{2}}{12}(-e^{iq}+e^{2iq}-e^{3iq}+e^{4iq}) + \frac{\sqrt{2}}{12}(-e^{iq}-e^{2iq}+e^{3iq}+e^{4iq}) \\ &= \frac{1}{2\sqrt{3}}(-e^{iq}+e^{4iq}) \quad \text{(A.4)}\end{aligned}$$

In order to proceed with the calculations one should use that $\mathbf{q}=\{0,1,2,3\}=\{0,\frac{\pi}{2},\pi,\frac{3\pi}{2}\}$ and that $|e_3\rangle$ has $\mathbf{q}=0$, $|e_1\rangle$ has $\mathbf{q}=0,2$ and $|e_2\rangle$ has $\mathbf{q}=0,1,2,3$. Hence summing Eqns. (A.2), (A.3) and (A.4) over $\mathbf{q}=0,2$, $\mathbf{q}=0,1,2,3$ and $\mathbf{q}=0$ respectively, one obtains

$$\sum_{e,\mathbf{q}} M_e^{zz}(\mathbf{q},\omega) = 2\pi\big(\frac{3}{4}+\frac{1}{2}(2\cos(2\pi))\big) = 2\pi = \frac{4\pi}{2} \quad \text{(A.5)}$$

which obeys the sum rule Eqn. (5.21) since $N=4$. We are now reassured that the result is right, and we can compare the individual matrix elements with the results of RLexact. This is done in the following table[2]. It is seen that the deviation are almost non existing, and hence the results of RLexact are judging from this test very reliable.

	Hand	RLexact	Deviation
$2\pi\|\langle gs\|S_q^z\|gs\rangle\|^2, q=0$	0	0	0
$2\pi\|\langle e_1\|S_q^z\|gs\rangle\|^2, q=0$	0	0	0
$2\pi\|\langle e_1\|S_q^z\|gs\rangle\|^2, q=2$	$4\pi/3 = 4.188790204$	4.18879	≈ 0
$2\pi\|\langle e_2\|S_q^z\|gs\rangle\|^2, q=0$	0	0	0
$2\pi\|\langle e_2\|S_q^z\|gs\rangle\|^2, q=1$	$2\pi/6 = 1.047197551$	1.0472	≈ 0
$2\pi\|\langle e_2\|S_q^z\|gs\rangle\|^2, q=2$	0	0	0
$2\pi\|\langle e_2\|S_q^z\|gs\rangle\|^2, q=3$	$2\pi/6 = 1.047197551$	1.0472	≈ 0
$2\pi\|\langle e_3\|S_q^z\|gs\rangle\|^2, q=0$	0	0	0

A.1.2 2x1

The situation for the 2x1 lattice is so simple that we will merely sketch the situation.
The ground state is $|gs\rangle = \frac{1}{\sqrt{2}}(|10\rangle - |01\rangle)$ and the only excited state with $m=0$ is $|e_1\rangle = \frac{1}{\sqrt{2}}(|10\rangle + |01\rangle)$. Since we only have two spins in this system, the possible values for $\mathbf{q}$ are $\mathbf{q}=\{0,\pi\}$.
Letting S_q^z operate on $|gs\rangle$ gives

$$S_q^z|gs\rangle = \big(\frac{1}{\sqrt{2}}\big)^2\frac{1}{2}\left((e^{iq}-e^{2iq})|10\rangle - (-e^{iq}+e^{2iq})|01\rangle\right) \quad \text{(A.6)}$$

[1] In the basis $\{|2\rangle\}$.
[2] Remark: That $\langle gs|S_q^z|gs\rangle = 0$ follows directly from Eqn. (A.1).

$q=0$	$q=\frac{\pi}{5}$	$q=\frac{2\pi}{5}$	$q=\frac{3\pi}{5}$	$q=\frac{4\pi}{5}$	$q=\frac{5\pi}{5}$
E=0	E=0.972167	E=1.62421	E=1.73496	$E=1.26928$	$E=0.423239$
$S^{zz}=0$	$S^{zz}=0.364259$	$S^{zz}=0.796646$	$S^{zz}=1.28966$	$S^{zz}=2.08531$	$S^{zz}=5.06766$
			$E=2.48653$	$E=2.55459$	$E=2.07663$
			$S^{zz}=0.0929543$	$S^{zz}=0.302418$	$S^{zz}=0.692448$
					$E=3.06329$
					$S^{zz}=0.0650366$

Table A.1: Data from RLexact for the 10x1 antiferromagnetical chain in zero field ($m=h=0$).

Taking the inner product with $\langle e_1|$ we get

$$\langle e_1|S^z_q|gs\rangle = \frac{1}{2\sqrt{2}}(e^{iq}-e^{2iq}) \tag{A.7}$$

Yielding

$$M^{zz}_{e_1}(\mathbf{q},\omega) = 2\pi|\langle e_1|S^z_q|gs\rangle|^2 = 2\pi\frac{1}{8}(e^{iq}-e^{2iq})(e^{-iq}-e^{-2iq}) = \frac{\pi}{4}(2-2\cos(q)) \tag{A.8}$$

When summing this over the two possible $\mathbf{q}$-values $\mathbf{q}=\{0,\pi\}$ we get

$$\sum_{e,\mathbf{q}} M^{zz}_e(\mathbf{q},\omega) = \frac{\pi}{4}((2-2)+(2+2)) = \pi = \frac{N\pi}{2} \quad , \tag{A.9}$$

since $N=2$. Hence the rule is fulfilled and we can state the individual contributions.

	Hand	RLexact	Deviation
$2\pi\|\langle e_1\|S^z_q\|gs\rangle\|^2, q=0$	0	0	0
$2\pi\|\langle e_1\|S^z_q\|gs\rangle\|^2, q=0$	0	0	0
$2\pi\|\langle e_1\|S^z_q\|gs\rangle\|^2, q=\pi$	$\pi=3.141592654$	3.14159	0

Remark: That $|\langle gs|S^z_q|gs\rangle|^2=0$ follows directly from Eqn. (A.6).

A.2 Comparison of $S^{zz}(\mathbf{q},\omega)$ from RLexact and the literature

In order to test the reliability of RLexact after the parallelization has been implemented, systems which have already been treated in the literature were run on RLexact to check for consistency.

A.2.1 10x1 RLexact

The antiferromagnetic 10x1 chain was investigated earlier by Müller *et al.*[35] in zero field. Table A.1 shows the results from RLexact of the 10x1 antiferromagnetic chain (for zero field), and in Fig. A.1 the results of Müller *et al.* are displayed. By comparing Fig. A.1 and Table A.1 it is clear that the results of RLexact and Müller *et al.* are completely consistent except at the lowest lying point for $q=\frac{3\pi}{5}$, where the two values are 1.29 and 1.30 respectively. Why there is a small deviation at this point I cannot explain, but a possible explanation is a misprint in [35], since there are at least one other misprint concerning $S^{zz}(\mathbf{q},\omega)$ as noted by [34].

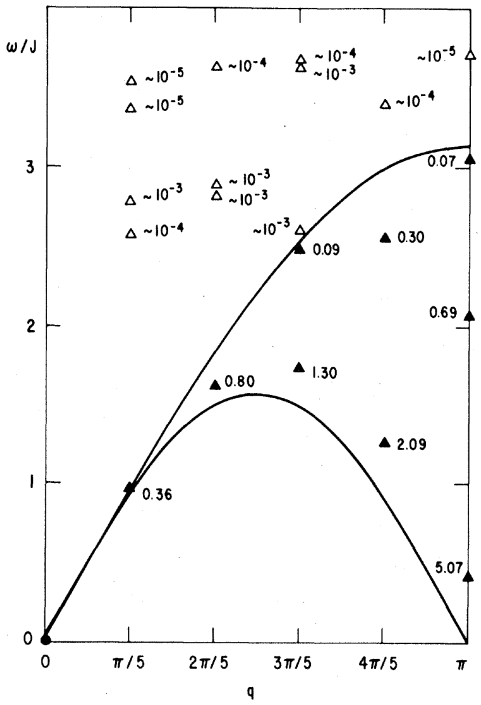

Figure A.1: Data for the dynamical structure factor $S^{zz}(\mathbf{q},\omega)$ for the 10x1 antiferromagnetic chain for $h = 0$. Data is from Müller *et al.* [35].

Appendix B

Selected details of RLexact

B.0.2 $\hat{H}^{\pm}$ working on the uniques

In this section we will for instructive reasons go through a full calculation of an element of $\hat{H}$, for the 2x4 square lattice. We arbitrarily choose $m = 0$ and the unique $|5\rangle$ for our example, but for completeness the set of uniques for all m-values of the 4x2 square lattice are found in Fig. B.1. The diagonal elements are calculated through $\hat{H}_{zz} = \sum_{\langle i,j \rangle} \mathbf{S_i} \cdot \mathbf{S_j}$. For $|5\rangle$ this gives $(\frac{1}{4}+\frac{1}{4})+(\frac{1}{4}-\frac{1}{4})+(-\frac{1}{4}-\frac{1}{4})+(\frac{1}{4}-\frac{1}{4})+(\frac{1}{4}-\frac{1}{4})+(\frac{1}{4}-\frac{1}{4})+(\frac{1}{4}-\frac{1}{4})+(\frac{1}{4}-\frac{1}{4})=0$
To find the off-diagonal elements, we let $\hat{H}_{\pm}$ operate on $|5\rangle$. When $\hat{H}_{\pm}$ operates on a unique, the result is number of non-unique state, which however can be reached by certain translation of a uniques. That is

$$\hat{H}_{\pm}|u_n\rangle = \sum_m \hat{T}_{x,y}|u_m\rangle$$

To be specific one uses that

$$\hat{T}_{x,y}|u\rangle = \sum_{t_x,t_y} e^{2\pi i(\frac{t_x}{N_x}q_x + \frac{t_y}{N_y}q_y)}|u + (t_x,t_y)\rangle \tag{B.1}$$

$N_{x(y)}$ is the number of possible translations along the $x(y)$ direction dictated by periodic boundary conditions, $t_{x(y)}$ is the actual given translation along the $x(y)$ direction, $q_{x(y)}$ is the associated reciprocal lattice vector and the notation $|u + (t_x, t_y)\rangle$ means the unique $|u\rangle$ translated t_x and t_y along the x- and y direction respectively.
This implies that a phase factor is attached to every state obtained from another state by translation. All phase factors as a function of q_x, q_y, t_x and t_y for the eight possible translations of the 2x4 square lattice ($N_x = 4$ and $N_y = 2$) is seen from Table B.2. Hence the phase factors must be multiplied onto the uniques $|u_m\rangle$. Since the phase factors depends on the the point in q-space for which we are trying to determine the matrix, one should in general expect different result for different q-vectors. For our example we chose to illustrate the calculations for two different q-vectors $\mathbf{q} = \binom{0}{0}$ and $\mathbf{q} = \binom{3}{1}$.
The first step, letting $\hat{H}_{\pm}$ operate, is the same for all **q**-vectors. We get

$$\begin{aligned}\hat{H}_{\pm}|5\rangle = \hat{H}_{\pm}\left|\begin{smallmatrix}0&0&0&1\\0&1&1&1\end{smallmatrix}\right\rangle &= \tfrac{1}{2}\Bigg(\left|\begin{smallmatrix}0&1&0&1\\0&0&1&1\end{smallmatrix}\right\rangle + \left|\begin{smallmatrix}0&0&1&0\\0&1&1&1\end{smallmatrix}\right\rangle + \left|\begin{smallmatrix}0&0&1&1\\0&1&0&1\end{smallmatrix}\right\rangle \\ &+\left|\begin{smallmatrix}1&0&0&0\\0&1&1&1\end{smallmatrix}\right\rangle + \left|\begin{smallmatrix}0&0&0&1\\1&0&1&1\end{smallmatrix}\right\rangle + \left|\begin{smallmatrix}0&1&0&1\\0&0&1&1\end{smallmatrix}\right\rangle + \left|\begin{smallmatrix}0&0&1&1\\0&1&0&1\end{smallmatrix}\right\rangle\Bigg)\end{aligned}$$

$$= \hat{T}_{0,1}|9\rangle + \hat{T}_{1,0}|4\rangle + \hat{T}_{0,0}|9\rangle + \hat{T}_{3,0}|2\rangle + \hat{T}_{0,0}|4\rangle + \hat{T}_{0,1}|9\rangle + \hat{T}_{0,0}|9\rangle + \hat{T}_{0,0}|2\rangle \tag{B.2}$$

m	$\lvert u\rangle$	a_n	Non-existing **q**	m	$\lvert u\rangle$	a_n	Non-existing **q**
0	$\lvert 1\rangle = \left\lvert \begin{smallmatrix} 0 & 0 & 0 & 0 \\ 1 & 1 & 1 & 1 \end{smallmatrix} \right\rangle$	2	$(1,0),(1,1),(2,0)$	1	$\lvert 1_1\rangle = \left\lvert \begin{smallmatrix} 0 & 0 & 0 & 1 \\ 1 & 1 & 1 & 1 \end{smallmatrix} \right\rangle$	8	
			$(2,1),(3,0),(3,1)$	1	$\lvert 2_1\rangle \left\lvert \begin{smallmatrix} 0 & 0 & 1 & 1 \\ 0 & 1 & 1 & 1 \end{smallmatrix} \right\rangle$	8	
0	$\lvert 2\rangle = \left\lvert \begin{smallmatrix} 0 & 0 & 0 & 1 \\ 1 & 1 & 1 & 0 \end{smallmatrix} \right\rangle$	8		1	$\lvert 3_1\rangle \left\lvert \begin{smallmatrix} 0 & 0 & 1 & 1 \\ 1 & 0 & 1 & 1 \end{smallmatrix} \right\rangle$	8	
0	$\lvert 3\rangle = \left\lvert \begin{smallmatrix} 0 & 0 & 0 & 1 \\ 1 & 1 & 0 & 1 \end{smallmatrix} \right\rangle$	8		1	$\lvert 4_1\rangle \left\lvert \begin{smallmatrix} 0 & 0 & 1 & 1 \\ 1 & 1 & 0 & 1 \end{smallmatrix} \right\rangle$	8	
0	$\lvert 4\rangle = \left\lvert \begin{smallmatrix} 0 & 0 & 0 & 1 \\ 1 & 0 & 1 & 1 \end{smallmatrix} \right\rangle$	8		1	$\lvert 5_1\rangle = \left\lvert \begin{smallmatrix} 0 & 0 & 1 & 1 \\ 1 & 1 & 1 & 0 \end{smallmatrix} \right\rangle$	8	
0	$\lvert 5\rangle = \left\lvert \begin{smallmatrix} 0 & 0 & 0 & 1 \\ 0 & 1 & 1 & 1 \end{smallmatrix} \right\rangle$	8		1	$\lvert 6_1\rangle = \left\lvert \begin{smallmatrix} 0 & 1 & 0 & 1 \\ 0 & 1 & 1 & 1 \end{smallmatrix} \right\rangle$	8	
0	$\lvert 6\rangle = \left\lvert \begin{smallmatrix} 0 & 0 & 1 & 1 \\ 0 & 0 & 1 & 1 \end{smallmatrix} \right\rangle$	4	$(0,1),(1,1),(2,1)$	1	$\lvert 7_1\rangle = \left\lvert \begin{smallmatrix} 0 & 1 & 0 & 1 \\ 1 & 0 & 1 & 1 \end{smallmatrix} \right\rangle$	8	
			$(3,1)$	2	$\lvert 1_2\rangle \left\lvert \begin{smallmatrix} 0 & 0 & 1 & 1 \\ 1 & 1 & 1 & 1 \end{smallmatrix} \right\rangle$	8	
0	$\lvert 7\rangle = \left\lvert \begin{smallmatrix} 0 & 0 & 1 & 1 \\ 1 & 1 & 0 & 0 \end{smallmatrix} \right\rangle$	4	$(0,1),(1,0),(2,1)$	2	$\lvert 2_2\rangle = \left\lvert \begin{smallmatrix} 0 & 1 & 0 & 1 \\ 1 & 1 & 1 & 1 \end{smallmatrix} \right\rangle$	4	$(1,0),(1,1),(3,0),(3,1)$
			$(3,0)$	2	$\lvert 3_2\rangle = \left\lvert \begin{smallmatrix} 0 & 1 & 1 & 1 \\ 0 & 1 & 1 & 1 \end{smallmatrix} \right\rangle$	4	$(0,1),(1,1),(2,1),(3,1)$
0	$\lvert 8\rangle = \left\lvert \begin{smallmatrix} 0 & 0 & 1 & 1 \\ 0 & 1 & 1 & 0 \end{smallmatrix} \right\rangle$	8		2	$\lvert 4_2\rangle = \left\lvert \begin{smallmatrix} 0 & 1 & 1 & 1 \\ 1 & 0 & 1 & 1 \end{smallmatrix} \right\rangle$	8	
0	$\lvert 9\rangle = \left\lvert \begin{smallmatrix} 0 & 0 & 1 & 1 \\ 0 & 1 & 0 & 1 \end{smallmatrix} \right\rangle$	8		2	$\lvert 5_2\rangle = \left\lvert \begin{smallmatrix} 0 & 1 & 1 & 1 \\ 1 & 1 & 0 & 1 \end{smallmatrix} \right\rangle$	4	$(0,1),(1,0),(2,1),(3,0)$
0	$\lvert 10\rangle = \left\lvert \begin{smallmatrix} 0 & 0 & 1 & 1 \\ 1 & 0 & 1 & 0 \end{smallmatrix} \right\rangle$	8		3	$\lvert 1_3\rangle = \left\lvert \begin{smallmatrix} 0 & 1 & 1 & 1 \\ 1 & 1 & 1 & 1 \end{smallmatrix} \right\rangle$	8	
0	$\lvert 11\rangle = \left\lvert \begin{smallmatrix} 0 & 1 & 0 & 1 \\ 0 & 1 & 0 & 1 \end{smallmatrix} \right\rangle$	2	$(0,1),(1,0),(1,1)$	4	$\lvert 1_4\rangle = \left\lvert \begin{smallmatrix} 1 & 1 & 1 & 1 \\ 1 & 1 & 1 & 1 \end{smallmatrix} \right\rangle$	1	$(0,1),(1,0),(1,1),(2,0)$
			$(2,1),(3,0),(3,1)$				$(2,1),(3,0),(3,1)$
0	$\lvert 12\rangle = \left\lvert \begin{smallmatrix} 0 & 1 & 0 & 1 \\ 1 & 0 & 1 & 0 \end{smallmatrix} \right\rangle$	2	$(0,1),(1,0),(1,1)$				
			$(2,0),(3,0),(3,1)$				

Figure B.1: Information about the Uniques of the 4x2 lattice.

Consulting table B.2 one finds the phase factors, arriving at two different results for $\mathbf{q} = \binom{0}{0}$ and $\mathbf{q} = \binom{3}{1}$.

For $\mathbf{q} = \binom{0}{0}$ one gets

$$\hat{H}_{\pm}|5\rangle = |2\rangle + |4\rangle + 2|9\rangle \tag{B.3}$$

For $\mathbf{q} = \binom{3}{1}$ one gets[1]

$$\hat{H}_{\pm}|5\rangle = \frac{1-i}{2}|2\rangle + \frac{1+i}{2}|4\rangle \tag{B.4}$$

B.0.3 The number of representatives

Each unique can by translation be transformed into a number of non-unique states. For the 4x2 lattice eight translations exist hence each unique can maximally represent eight states. If a number of states are not represented, this number corresponds to the exact same number of certain q-values not allowed. How this comes about is seen in the example below.
For the example is chosen the unique $|2_2\rangle$[2]. If we let the Total Translation operator operate on the unique we obtain

$$\begin{aligned}
\hat{T}_T|2_2\rangle &= \left|\begin{smallmatrix}0&1&0&1\\1&1&1&1\end{smallmatrix}\right\rangle + e^{2\pi i(\frac{q_x}{4}\cdot 0+\frac{q_y}{2}\cdot 1)}\left|\begin{smallmatrix}1&1&1&1\\0&1&0&1\end{smallmatrix}\right\rangle \\
&+ e^{2\pi i(\frac{q_x}{4}\cdot 1+\frac{q_y}{2}\cdot 0)}\left|\begin{smallmatrix}1&0&1&0\\1&1&1&1\end{smallmatrix}\right\rangle + e^{2\pi i(\frac{q_x}{4}\cdot 1+\frac{q_y}{2}\cdot 1)}\left|\begin{smallmatrix}1&1&1&1\\1&0&1&0\end{smallmatrix}\right\rangle \\
&+ e^{2\pi i(\frac{q_x}{4}\cdot 2+\frac{q_y}{2}\cdot 0)}\left|\begin{smallmatrix}0&1&0&1\\1&1&1&1\end{smallmatrix}\right\rangle + e^{2\pi i(\frac{q_x}{4}\cdot 2+\frac{q_y}{2}\cdot 1)}\left|\begin{smallmatrix}1&1&0&0\\0&1&0&1\end{smallmatrix}\right\rangle \\
&+ e^{2\pi i(\frac{q_x}{4}\cdot 3+\frac{q_y}{2}\cdot 0)}\left|\begin{smallmatrix}1&0&1&0\\1&1&1&1\end{smallmatrix}\right\rangle + e^{2\pi i(\frac{q_x}{4}\cdot 3+\frac{q_y}{2}\cdot 1)}\left|\begin{smallmatrix}1&1&1&1\\1&0&1&0\end{smallmatrix}\right\rangle \\
&= \left|\begin{smallmatrix}0&1&0&1\\1&1&1&1\end{smallmatrix}\right\rangle\left(1+e^{\pi i q_x}\right) + \left|\begin{smallmatrix}1&1&1&1\\0&1&0&1\end{smallmatrix}\right\rangle\left(e^{\pi i q_y}+e^{\pi i(q_x+q_y)}\right) \\
&+ \left|\begin{smallmatrix}1&0&1&0\\1&1&1&1\end{smallmatrix}\right\rangle\left(e^{\pi i\frac{q_x}{2}}+e^{\pi i\frac{3}{2}q_x}\right) + \left|\begin{smallmatrix}1&1&1&1\\1&0&1&0\end{smallmatrix}\right\rangle\left(e^{\pi i(\frac{q_x}{2}+q_y)}+e^{\pi i(\frac{3}{2}q_x+q_y)}\right)
\end{aligned}$$

Each parenthesis can be written on the form $(1+e^{\pi i q_x})$ possibly with a prefactor. Demanding that $(1+e^{\pi i q_x}) \neq 0$ for the phases not to cancel results in the constraint $q_x \neq 2n+1$, disqualifying the q-values $\mathbf{q} \in \{\binom{1}{0}, \binom{1}{1}, \binom{3}{0}, \binom{3}{1}\}$.
In order to illustrate the origin of these phases an example will be done for $(q_x, q_y) = (3,1)$. The phases are as follows:

$$\sum_{t_x,t_y} e^{2\pi i(\frac{t_x}{4}\cdot 3+\frac{t_y}{2}\cdot 1)} = e^{2\pi i(\{0,\frac{1}{2},\frac{3}{4},\frac{5}{4},\frac{6}{4},\frac{8}{4},\frac{9}{4},\frac{11}{4}\})} = \{1,-1,-i,i,-1,1,i,-i\}$$

where the sum should be understood as going through all possibilities (as opposed to a actual summing up of terms) and the awkward notation in the exponent simply is a listing of the results from the $2\cdot 4 = 8$ different translations. The convention is to translate zero along x and zero along y, then one along x and zero along y, then one along x and one along y, then two along x and zero along y etc., obtaining the sequence $(0,0),(0,1),(1,0),(1,1),(2,0),(2,1),(3,0),(3,1)$.
The above knowledge of the phases would in Eqn. (B.2) be implied as follows: One can at all

[1] Note that the phasefactors in this case cancels out such that unique $|9\rangle$ no longer is present.
[2] See Table B.1

(t_x, t_y)	$(0,0)$	$(0,1)$	$(1,0)$	$(1,1)$	$(2,0)$	$(2,1)$	$(3,0)$	$(3,1)$
(q_x, q_y)								
$(0,0)$	1	1	1	1	1	1	1	1
$(0,1)$	1	-1	1	-1	1	-1	1	-1
$(1,0)$	1	1	i	i	-1	-1	$-i$	$-i$
$(1,1)$	1	-1	i	$-i$	-1	1	$-i$	i
$(2,0)$	1	1	-1	-1	1	1	-1	-1
$(2,1)$	1	-1	-1	1	1	-1	-1	1
$(3,0)$	1	1	$-i$	$-i$	-1	-1	i	i
$(3,1)$	1	-1	$-i$	i	-1	1	i	$-i$

Figure B.2: Phase factors generated by the Total Translation Operator.

times consult table B.2 to find the corresponding phases for a given (q_x, q_y) and (t_x, t_y). It should be noted that RLexact does not calculate a scheme such as in table B.2, instead it simply calculates the attached phase for every unique that needs to be translated into a state after a action like that in Eqn. (B.2). I have however chosen to include Table B.2 for instructive reasons.

The final step in finding the entries of the each block, is to weigh the number of states that each initial unique $|u_i\rangle$ represents before $\hat{H}_{\pm}$ operates on it, with the number of states represented by the various uniques to which $|u_i\rangle$ is sent. This is done by multiplying each term by the ratio of the square root of the number of states represented by $|u_i\rangle$ to the square root of the number of states represented by each final unique $|u_f\rangle$. Continuing with the example of Eqn. (B.2) yields the final result

$$|2\rangle + |4\rangle + 2|9\rangle \rightarrow \sqrt{\frac{a_5}{a_2}}|2\rangle + \sqrt{\frac{a_5}{a_4}}|4\rangle + 2\sqrt{\frac{a_5}{a_9}}|9\rangle = |2\rangle + |4\rangle + 2|9\rangle \tag{B.5}$$

where the a_n's are defined in Table 5.3. It is from Eqn. (B.5) seen, that no prefactor changes, since in the particular case of the unique $|5\rangle$, by coincidence $a_2 = a_4 = a_5 = a_9$ and hence the relative magnitude of the involved a_n's are 1. This is far from always the case.

State $\lvert s\rangle$	corresponding $\lvert u\rangle with \hat{T}_{t_x,t_y}\lvert u\rangle = \lvert s\rangle$	(t_x, t_y)
$\left\lvert \begin{matrix} 0 & 1 & 0 & 1 \\ 0 & 0 & 1 & 1 \end{matrix} \right\rangle$	$\left\lvert \begin{matrix} 0 & 0 & 1 & 1 \\ 0 & 1 & 0 & 1 \end{matrix} \right\rangle = \lvert 9\rangle$	$(0,1)$
$\left\lvert \begin{matrix} 0 & 0 & 1 & 0 \\ 0 & 1 & 1 & 1 \end{matrix} \right\rangle$	$\left\lvert \begin{matrix} 0 & 0 & 0 & 1 \\ 1 & 0 & 1 & 1 \end{matrix} \right\rangle = \lvert 4\rangle$	$(3,0)$
$\left\lvert \begin{matrix} 0 & 0 & 1 & 1 \\ 0 & 1 & 0 & 1 \end{matrix} \right\rangle$	$\left\lvert \begin{matrix} 0 & 0 & 1 & 0 \\ 0 & 1 & 1 & 1 \end{matrix} \right\rangle = \lvert 9\rangle$	$(0,0)$
$\left\lvert \begin{matrix} 1 & 0 & 0 & 0 \\ 0 & 1 & 1 & 1 \end{matrix} \right\rangle$	$\left\lvert \begin{matrix} 0 & 0 & 0 & 1 \\ 1 & 1 & 1 & 0 \end{matrix} \right\rangle = \lvert 2\rangle$	$(1,0)$
$\left\lvert \begin{matrix} 0 & 0 & 0 & 1 \\ 1 & 0 & 1 & 1 \end{matrix} \right\rangle$	$\left\lvert \begin{matrix} 0 & 0 & 0 & 1 \\ 1 & 0 & 1 & 1 \end{matrix} \right\rangle = \lvert 4\rangle$	$(0,0)$
$\left\lvert \begin{matrix} 0 & 1 & 0 & 1 \\ 0 & 0 & 1 & 1 \end{matrix} \right\rangle$	$\left\lvert \begin{matrix} 0 & 0 & 1 & 1 \\ 0 & 1 & 0 & 1 \end{matrix} \right\rangle = \lvert 9\rangle$	$(0,1)$
$\left\lvert \begin{matrix} 0 & 0 & 1 & 1 \\ 0 & 1 & 0 & 1 \end{matrix} \right\rangle$	$\left\lvert \begin{matrix} 0 & 0 & 1 & 1 \\ 0 & 1 & 0 & 1 \end{matrix} \right\rangle = \lvert 9\rangle$	$(0,0)$
$\left\lvert \begin{matrix} 0 & 0 & 0 & 1 \\ 1 & 1 & 1 & 0 \end{matrix} \right\rangle$	$\left\lvert \begin{matrix} 0 & 0 & 0 & 1 \\ 1 & 1 & 1 & 0 \end{matrix} \right\rangle = \lvert 2\rangle$	$(0,0)$

Figure B.3: Table showing which Uniques $\lvert u\rangle$ should be translated to obtain the bit patterns in the first column.

Appendix C

Results for exact diagonalization

This appendix presents documentation for the hand-calculated diagonalization results.

C.0.4 $m = 0$,$\mathbf{q} = \binom{0}{0}$

$$H_{00,m=0} = \begin{pmatrix}
0 & 2 & 0 & 0 & 0 & 0 & 0 & 0 & 0 & 0 & 0 & 0 \\
2 & -2 & 1 & 0 & 1 & 0 & 2\sqrt{2} & 0 & 0 & 0 & 0 & 2 \\
0 & 1 & 0 & 1 & 0 & 0 & 0 & 0 & 0 & 2 & 0 & 0 \\
0 & 0 & 1 & 0 & 1 & 0 & 0 & 2 & 0 & 0 & 0 & 0 \\
0 & 1 & 0 & 1 & 0 & 0 & 0 & 0 & 2 & 0 & 0 & 0 \\
0 & 0 & 0 & 0 & 0 & 2 & 0 & 0 & \frac{1}{\sqrt{2}} & \frac{1}{\sqrt{2}} & 0 & 0 \\
0 & 2\sqrt{2} & 0 & 0 & 0 & 0 & -2 & 0 & \frac{1}{\sqrt{2}} & \frac{1}{\sqrt{2}} & 0 & 0 \\
0 & 0 & 0 & 2 & 0 & 0 & 0 & 0 & 1 & 1 & 0 & 0 \\
0 & 0 & 0 & 0 & 2 & \frac{1}{\sqrt{2}} & \frac{1}{\sqrt{2}} & 1 & -1 & 0 & 1 & 1 \\
0 & 0 & 2 & 0 & 0 & \frac{1}{\sqrt{2}} & \frac{1}{\sqrt{2}} & 1 & 0 & -1 & 1 & 1 \\
0 & 0 & 0 & 0 & 0 & 0 & 0 & 0 & 1 & 1 & 0 & 0 \\
0 & 2 & 0 & 0 & 0 & 0 & 0 & 0 & 1 & 1 & 0 & -4
\end{pmatrix}$$

$$\mathbf{\Phi}_{|gs\rangle,00,m=0,Maple} = \begin{pmatrix}
0.3064418204 \\
-1.062484739 \\
0.3251963680 \\
-0.1147573950 \\
0.3223612395 \\
0.06415853865 \\
0.7299253308 \\
0.1536811089 \\
-0.4053233322 \\
-0.4053233104 \\
0.1169033388 \\
1
\end{pmatrix}$$

$$\begin{aligned}
E_{|gs\rangle,00,m=0,Maple} &= -6.934332510 \\
E_{|gs\rangle,00,m=0,RLexact} &= -6.93433
\end{aligned}$$

C.0.5 $m = 0$,$\mathbf{q} = \binom{3}{1}$

$$\hat{H}_{31,m=0} = \begin{pmatrix} -2 & \frac{1+i}{2} & 0 & \frac{1-i}{2} & \sqrt{2}(1+i) & 0 & 0 & 0 \\ \frac{1-i}{2} & 0 & \frac{1+i}{2} & 0 & 0 & 0 & 0 & 0 \\ 0 & \frac{1-i}{2} & 0 & \frac{1+i}{2} & 0 & 0 & 0 & 0 \\ \frac{1+i}{2} & 0 & \frac{1-i}{2} & 0 & 0 & 0 & 0 & 0 \\ \sqrt{2}(1-i) & 0 & 0 & 0 & -2 & 0 & \frac{1}{\sqrt{2}} & \frac{1}{\sqrt{2}} \\ 0 & 0 & 0 & 0 & 0 & 0 & \frac{1+i}{2} & \frac{1+i}{2} \\ 0 & 0 & 0 & 0 & \frac{1}{\sqrt{2}} & \frac{1-i}{2} & -1 & 0 \\ 0 & 0 & 0 & 0 & \frac{1}{\sqrt{2}} & \frac{1-i}{2} & 0 & -1 \end{pmatrix}, \mathbf{\Phi}_{|gs\rangle,31,m=0,Maple} = \begin{pmatrix} 0 \\ 0 \\ 0 \\ 0 \\ -1 \\ 1 \\ 1 \\ 0 \end{pmatrix}$$

$$\begin{aligned} E_{|gs\rangle,31,m=0,Maple} &= -4.281394240 \\ E_{|gs\rangle,31,m=0,RLexact} &= -4.28139 \end{aligned}$$

C.0.6 $m = 0$,$\mathbf{q} = \binom{2}{1}$

$$\hat{H}_{21,m=0} = \begin{pmatrix} -2 & 0 & 0 & 0 & 0 & 0 & 0 & 2 \\ 0 & 0 & 0 & 0 & 0 & 0 & 0 & 0 \\ 0 & 0 & 0 & 0 & 0 & 0 & 0 & 0 \\ 0 & 0 & 0 & 0 & 0 & 0 & 0 & 0 \\ 0 & 0 & 0 & 0 & 0 & 1 & 1 & 0 \\ 0 & 0 & 0 & 0 & 1 & -1 & 0 & -1 \\ 0 & 0 & 0 & 0 & 1 & 0 & -1 & 1 \\ 2 & 0 & 0 & 0 & 0 & 1 & -1 & -4 \end{pmatrix}, \mathbf{\Phi}_{|gs\rangle,21,m=0,Maple} = \begin{pmatrix} -0.5615528128 \\ 0 \\ 0 \\ 0 \\ 0 \\ 0.2192235935 \\ -0.2192235936 \\ 1 \end{pmatrix}$$

$$\begin{aligned} E_{|gs\rangle,21,m=0,maple} &= -5.561552813 \\ E_{|gs\rangle,21,m=0,RLexact} &= -5.56155 \end{aligned}$$

C.0.7 $m = 1$,$\mathbf{q} = \binom{0}{0}$

$$\hat{H}_{00,m=1} = \begin{pmatrix} 1 & 0 & 0 & 1 & 1 & 0 & 1 \\ 0 & 2 & \frac{1}{2} & 0 & \frac{1}{2} & \frac{1}{2} & \frac{1}{2} \\ 0 & \frac{1}{2} & 2 & \frac{1}{2} & 0 & \frac{1}{2} & \frac{1}{2} \\ 1 & 0 & \frac{1}{2} & -1 & \frac{3}{2} & \frac{1}{2} & \frac{3}{2} \\ 1 & \frac{1}{2} & 0 & \frac{3}{2} & -1 & \frac{1}{2} & \frac{3}{2} \\ 0 & \frac{1}{2} & \frac{1}{2} & \frac{1}{2} & \frac{1}{2} & 1 & 1 \\ 1 & \frac{1}{2} & \frac{1}{2} & \frac{3}{2} & \frac{3}{2} & 1 & -2 \end{pmatrix}, \mathbf{\Phi}_{|gs\rangle,00,m=1,Maple} = \begin{pmatrix} 1 \\ 0.5 \\ 0.5 \\ 1.5 \\ 1.5 \\ 1 \\ -2 \end{pmatrix}$$

$$\begin{aligned} E_{|gs\rangle,00,m=1,maple} &= -3.307926037 \\ E_{|gs\rangle,00,m=1,RLexact} &= -3.30793 \end{aligned}$$

C.0.8 $m = 1$,$\mathbf{q} = \binom{2}{1}$

$$\hat{H}_{21,m=1} = \begin{pmatrix} -1 & 0 & 0 & 1 & -1 & 0 & 1 \\ 0 & 0 & \frac{1}{2} & 0 & \frac{1}{2} & \frac{1}{2} & -\frac{1}{2} \\ 0 & \frac{1}{2} & 0 & \frac{1}{2} & 0 & -\frac{1}{2} & \frac{1}{2} \\ 1 & 0 & \frac{1}{2} & -1 & \frac{3}{2} & \frac{1}{2} & -\frac{3}{2} \\ -1 & \frac{1}{2} & 0 & \frac{3}{2} & -1 & -\frac{1}{2} & \frac{3}{2} \\ 0 & \frac{1}{2} & -\frac{1}{2} & \frac{1}{2} & -\frac{1}{2} & -1 & 1 \\ 1 & -\frac{1}{2} & \frac{1}{2} & -\frac{3}{2} & \frac{3}{2} & 1 & 2 \end{pmatrix}, \mathbf{\Phi}_{|gs\rangle,21,m=1,Maple} = \begin{pmatrix} -0.5615528121 \\ 0.2192235937 \\ -0.2192235937 \\ 0.7807764063 \\ -0.7807764070 \\ -0.4384471872 \end{pmatrix}$$

$$\begin{aligned} E_{|gs\rangle,21,m=1,maple} &= -5.561552813 \\ E_{|gs\rangle,21,m=1,RLexact} &= -5.56155 \end{aligned}$$

C.0.9 $m = 2$,$\mathbf{q} = \binom{0}{0}$

$$\hat{H}_{00,m=2} = \begin{pmatrix} 1 & \sqrt{2} & 0 & 2 & 0 \\ \sqrt{2} & 0 & 0 & 0 & 2 \\ 0 & 0 & 2 & \sqrt{2} & 0 \\ 2 & 0 & \sqrt{2} & 0 & \sqrt{2} \\ 0 & 2 & 0 & \sqrt{2} & 0 \end{pmatrix}, \mathbf{\Phi}_{|gs\rangle,00,m=2,Maple} = \begin{pmatrix} 0.7782272848 \\ -0.9373183542 \\ 0.2700281475 \\ -1.013488679 \\ 1 \end{pmatrix}$$

$$\begin{aligned} E_{|gs\rangle,00,m=2,maple} &= -3.307926037 \\ E_{|gs\rangle,00,m=2,RLexact} &= -3.30793 \end{aligned}$$

C.0.10 $m = 2$,$\mathbf{q} = \binom{2}{1}$

$$\hat{H}_{21,m=2} = \begin{pmatrix} 1 & 0 & 0 \\ 0 & 0 & 0 \\ 0 & 0 & 0 \end{pmatrix}, \mathbf{\Phi}_{|gs\rangle,21,m=2,Maple} = \begin{pmatrix} 0 \\ 0 \\ 1 \end{pmatrix} \text{ or } \mathbf{\Phi}_{|gs\rangle,21,m=2,Maple} = \begin{pmatrix} 0 \\ 1 \\ 0 \end{pmatrix}$$

$$\begin{aligned} E_{|gs\rangle,21,m=2,maple} &= 0 \\ E_{|gs\rangle,21,m=2,RLexact} &= 0 \end{aligned}$$

Appendix D

Extra notes

D.1 The staggered magnetization

Fig. D.1 presents the staggered magnetization $m^\dagger$ as a function of magnetic field. In [39] the staggered moment is calculated by use of

$$(m^\dagger)^2(N) = (m^\dagger)^2\left[1 + 0.062075\left(\frac{n-1}{2}\right)\frac{c}{\rho_s\sqrt{N}} + \mathcal{O}\left(\frac{1}{N}\right)\right] \tag{D.1}$$

Here ρ_s is the spin stiffness, c is the spin wave velocity, n is the dimensionality (1, 2 and 3) and N is the number of spins in the system.
The formula is merely stated for reference and has not been used in this thesis work.

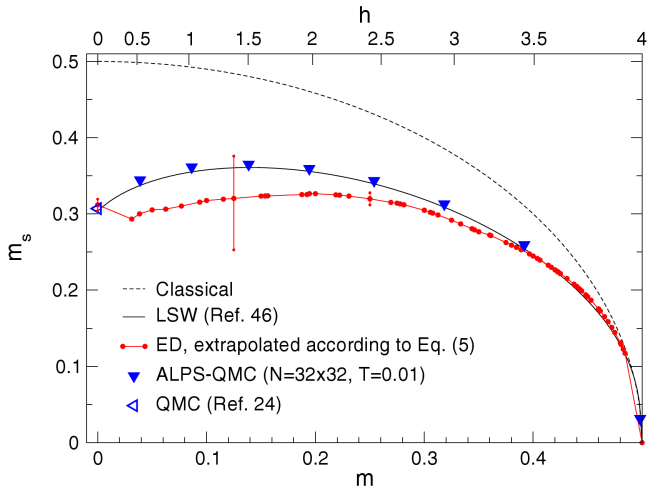

Figure D.1: Staggered magnetization $m^\dagger$ obtained from finite-size extrapolations according to Eqn. (D.1), quantum Monte Carlo simulations, and spin-wave calculations. The picture is taken directly from [39].

D.1.1 Uncertainties

Following [10] the uncertainties of a least squares fit yielding $y = A + Bx$ are given by

$$\sigma_A = \sigma_y\sqrt{\frac{\sum_i x_i^2}{\Delta}} \quad , \tag{D.2}$$

where

$$\sigma_y = \sqrt{\frac{1}{N-2}\sum_{i=1}^{N}(y_i - A - Bx_i)^2} \tag{D.3}$$

and

$$\Delta = N\sum_i x_i^2 - (\sum_i x_i)^2 \tag{D.4}$$

Here $\{x_i\}_{i=1}^N$ are the independent variable, $\{y_i\}_{i=1}^N$ are the independent variable and N is the number of observations.
For the $1/N$ interpolation we have $x_i = \{0.267393, 0.301607, 0.321367\}$ and $y_i = \{1/32, 1/16, 1/8\}$ and for the $1/\sqrt{N}$ fit we have the same values for x_i but this time $y_i = \{1/\sqrt{32}, 1/\sqrt{16}, 1/\sqrt{8}\}$.
For the fitting results of $m^\dagger = 0.258 + 0.539 \cdot \frac{1}{N}$ and $m^\dagger = 0.219 + .298 \cdot \frac{1}{N}$ for the $1/N$ and $1/\sqrt{N}$ fits the uncertainties are respectively $\sigma_{m^\dagger} \approx 0.7$ and $\sigma_{m^\dagger} \approx 0.12$.
It should be noted that these are big uncertainties relative to the value of $m^\dagger$.

D.2 Points in q-space

When naming points in the two dimensional q-space of the square lattice the following notation is used:

$\Gamma = (0, 0)$
$M = (\pi, 0)$
$X = (\pi, \pi)$
$S = (\frac{\pi}{2}, \frac{\pi}{2})$

D.3 Symmetry consideration

$\mathbf{S}^z$	Dim $\mathbf{S}^z$
$\frac{N}{2}$	1
$\frac{N}{2}-1$	$\binom{N}{1}$
$\frac{N}{2}-2$	$\binom{N}{2}$
$\vdots$	$\vdots$
$\frac{N}{2}-\left(\frac{N}{2}-1\right)=1$	$\binom{N}{\frac{N}{2}-1}$
$\frac{N}{2}-\frac{N}{2}=0$	$\binom{N}{N/2}$
$-\frac{N}{2}+\left(\frac{N}{2}-1\right)=-1$	$\binom{N/2}{\frac{N}{2}-1}$
$\vdots$	$\vdots$
$-\frac{N}{2}+2$	$\binom{N}{2}$
$-\frac{N}{2}+1$	$\binom{N}{1}$
$-\frac{N}{2}$	1
Sum of dimensions	$\binom{N}{N/2}+2\sum_{n=0}^{\frac{N}{2}-1}\binom{N}{n}$

Figure D.2: First column shows the possible values of $m \equiv \mathbf{S}^z$ and the second column shows the dimension of each value, that is the number of different states having the given m.

A visualization of $\hat{H}$ is seen in Fig. D.3.

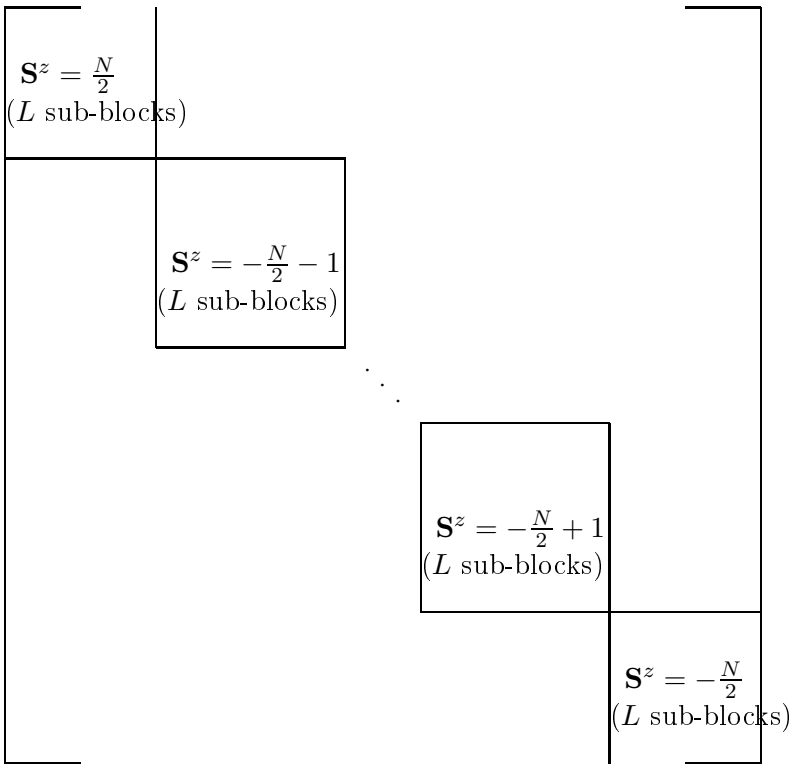

Figure D.3: Illustration of $\hat{H}$. In blocks with $m = \mathbf{S^z} = \pm\frac{N}{2} \mp 1$ the dimension is $\binom{N}{1} \times \binom{N}{1}$, since *one spin* points oppositely to the rest, having N different sites to occupy. The dimension of the next two block going towards the 'center' of $\hat{H}$ is $\binom{N}{2} \times \binom{N}{2}$. Continuing this line of thought, the m invariant blocks of $\hat{H}$ can be constructed. It is each of these blocks that can be further block diagonalized into L sub-blocks due to translation symmetry, represented by the quantum numbers k_x and k_y.

Bibliography

[1] U. Schollwöck, J. Richter et al., *Quantum Magnetism*, Springer 2004.

[2] Michael Tinkham, *Introduction to superconductivity*, Second edition, Dover Publications, 1996.

[3] Michael P. Marder, *Condensed Matter Physics. Corrected Printing*, John Wiley & Sons Inc.,2000.

[4] G.L. Squires, *Introduction to the theory of thermal neutron scattering*, Dover Publications, 1978.

[5] G. Shirane, S.M. Shapiro and J.M. Tranquada, *Neutron Scattering with a Triple-Axis Spectrometer*, Cambridge University Press, 2002.

[6] K. Yosida, *Theory of Magnetism*, Springer, Solid-State Sciences 122, 1991.

[7] Jane K. Cullum, Ralph A. Willoughby, *Lanczos Algorithms for Large Symmetric Eigenvalue Computations Vol. II Programs*, Birkhäuser Boston Inc.,1985.

[8] Jane K. Cullum, Ralph A. Willoughby, *Lanczos Algorithms for Large Symmetric Eigenvalue Computations Vol. I Theory*, Birkhäuser Boston Inc.,1985

[9] J.J. Sakurai, *Modern Quantum Mechanics*, Addison Wesley Longman, Revised edition, 1994

[10] J. R. Taylor, *An Introduction to Error Analysis*, Second Edition, University Science Books, 1997

[11] T. Thio *et al.*, *Antisymmetric exchange and its influence on the magnetic structure and conductivity of* La_2CuO_4, Phys. Rev. B, 38, p. 905 (1988)

[12] P.W. Anderson, Mater Res. Bull, 8, p. 153 (1973).

[13] P.W. Anderson, Science, 235, p. 1196-1198 (1987).

[14] P.W. Anderson, *An Approximate Quantum Theory of the Antiferromagnetic Ground State*, Phys. Rev., 86, p. 694-701 (1952).

[15] D. A. Huse, *Ground-state staggered magnetization of two-dimensional quantum Heisenberg antiferromagnets*, Phys. Rev. B Rapid Com., 37, p.2380-2382 (1988).

[16] J. Oitmaa and D. D. Betts, *The Ground state of two quantum models of magnetism*, Can. J. Phys., 56, p.897-901(1978).

[17] H.A.Bethe, Z Phys, 74, p. 205-226 (1931).

[18] N. Burger *et al.*, *Neutron diffraction Study of the Antiferromagnetic Phase of Copper Formate Tetradeuterate*, Solid State Com., 34, p. 883-886 (1980).

[19] H.M.Rønnow et al., *Spin dynamics of the Spin $\frac{1}{2}$ quantum Antiferromagnet Copper Deuteroformate Tetradeuterate (CFTD)*, Phys. Rev. Letters, 87, (2001).

[20] O. F. Syljuåsen, *Numerical evidence for unstable magnons at high fields in the Heisenberg antiferromagnet on the square lattice*, Phys. Rev. B, 78, (2008).

[21] J.-Y.P. Delannoy et al. (2009), *Low-energy theory of the t-t'-t"-U Hubbard model at half filling: Interaction strengths in cuprate superconductors and an effective spin-only describtion of La_2CuO_4*, Phys. Rev. B, 79, p. 235130 (2009)

[22] K. Lefmann *Neutron Scattering: Theory, Instrumentation and Simulation*, Lecture notes, Sep. 2009.

[23] N.B. Christensen *et al.*, *Quantum dynamics and entanglement of soins on a square lattice*, PNAS, 104, p.15264-15269 (2007).

[24] J.F. Annett *et al.*, Phys. Rev B, 40, p.2620 (1989).

[25] Y.J. Kim *et al.*,*Ordering due to Quantum Fluctuations in $Sr_2Cu_3O_4Cl_2$*, Phys. Rev. Lett., 83, p. 852-855 (1999).

[26] J. Igarashi, *1/N expansion for thermodynamic quantitiesin a two dimensional Heisenberg antiferromagnet at zero temperature*, Phys. Rev. B, 46, p. 392-405 (1966).

[27] M. D. Lumsden et al., *Magnetic exitation spectrum of the square lattice $S = 1/2$ Heisenberg antiferromagnet $K_2V_3O_8$*, Phys. Rev. B, 74, p. 2144424 (2006).

[28] T. Huberman et al., *Two-magnon excitations observed by neutron scattering in the two-dimensional spin- $\frac{5}{2}$ Heisenberg antiferromagnet Rb_2MnF_4*, Phys. Rev. B, 72, p. 014413 (2005).

[29] N. Tsyrulin et al., *Quantum Effects in a Weakly Frustrated $S = 1/2$ Two-Dimensional Heisenberg Antiferromagnet in applied magnetic field*, Phys. Rev. Lett., 102, p. 197201 (2009).

[30] E. Dagotto and A. Moreo, *Zero-temperature properties of the two-dimensional Heisenberg antiferromagnet: A nummerical study*, Phys. Rev. B Rapid Com.,38, p. 5087 (1988).

[31] D. Vaknin et al., *Antiferromagnetism in La_2CuO_{4-y}*, Phys. Rev. Lett., 58, p. 2802 (1987).

[32] J. D. Reger and A. P. Young, *Monte Carlo simulations of the spin-$\frac{1}{2}$ Heisenberg antiferromagnet on a square lattice*, Phys. Rev. B - Rapid Com.,37, p. 5978 (1988).

[33] R. Coldea *et al.*,*Spin Waves and Electronic Interactions in La_2CuO_4*, Phys. Rev. Lett., 86, p. 5377 (2001).

[34] K. Lefmann, C. Rischel, *Dynamical correlation functions of the $S = \frac{1}{2}$ nearest-neighbor and Haldane-Shastry Heisenberg antiferromagnetic chains in zero and applied fields*, Phys. Rev. B, 54, p. 6340 (1996).

[35] G. Müller, H. Thomas *et al.*, *Quantum spin dynamics of the antiferromagnetic linear chain in zero and nonzero magnetic field*, Phys. Rev. B, 24, p. 1429-1457 (1981).

[36] J. C. Bonner and M.E. Fisher, *Linear Magnetic Chains with Anisotropic Coupling*, Phys. Rev, 135, p. A640-A658 (1964).

[37] E. H. Lieb, *The Hubbard Model: Some rigorous results and open problems*, Phys. Rev. B, 40, 1-20 (1993)

[38] A. W. Sandvik and R. R. P. Singh, *High-Energy Dispersion and Multimagnon Continuum in the Two-Dimensional Heisenberg Antiferromagnet*, Phys. Rev. Lett., 86, p. 528-531 (2001)

[39] A. Lüscher and A. M. Läushli. *Exact diagonalization study of the antiferromagnetic spin-$\frac{1}{2}$ Heisenber model on the square lattice in a magnetic field*, Phys. Rev. B, 79, p. 195102 (2009).

[40] F. Treue, *2D Lanczos Algorithm*, Report, University of Copenhagen, October 2008.

[41] S. Rosenlund and J í Hjøllum, *Quantum Monte Carlo Simulation of a 1D spin-$\frac{1}{2}$ isotropic Heisenberg Antiferromagnet*, Report, University of Copenhagen.